

Corrosion propagation in cracked reinforced concrete structures

by

Schalk Ruan Bezuidenhout

Thesis presented in partial fulfilment of the requirements for the degree of Master of Engineering in the Faculty of Engineering at Stellenbosch University



Supervisor: Prof G.P.A.G. van Zijl

December 2017

Declaration

By submitting this thesis electronically, I declare that the entirety of the work contained therein is my own, original work, that I am the sole author thereof (save to the extent explicitly otherwise stated), that reproduction and publication thereof by Stellenbosch University will not infringe any third party rights and that I have not previously in its entirety or in part submitted it for obtaining any qualification.

S.R. Bezuidenhout

December, 2017

Copyright © 2017 Stellenbosch University
All rights reserved

Acknowledgements

I would like to express my sincere gratitude to the following people for their assistance and support during the course of this study:

- Professor G.P.A.G. van Zijl, for being an excellent mentor, for all the advice, support and willingness to always help during the course of this thesis.
- The Civil Engineering laboratory and workshop; Johan van der Merwe, Stephan Zeranka, Charlton Ramat and Peter Cupido during the execution of my experimental work.
- Stellenbosch University and Lithon Project Consultants Namibia for the financial assistance that made all of this possible.
- Carli Loubser, for her love and support during the past two years.
- To my family, especially father, mother and sister for the encouragement and support.
- Friends for keeping me sane throughout the writing of this thesis.
- For Theo Müller and Stacey van Nierop for proof reading of this thesis.

And lastly, but most importantly, I would like to thank God my Saviour, for the blessings, grace and unconditional love during the past two years. All the honour and glory goes to Him who gave me perseverance and ability.

Abstract

The durability of a reinforced concrete (RC) structure is significantly influenced by the presence of cracks. Cracks act as pathways that accelerate the ingress of corrosion agents into the concrete to the embedded reinforcement. This causes the acceleration of both the corrosion initiation and propagation stages of degradation. The increase in the corrosion rate in the corrosion propagation stage leads to a reduction in the residual service life of a structure. The overall effect of cracks in RC structures is that the residual service life of a structure is remarkably shortened.

In recent years, many researchers have investigated the corrosion of structures in the propagation stage. However, the majority of these investigations are focused on specimens with only one crack and reinforcement rod. This study investigates cracked RC exposed to chloride-induced corrosion. The experimental investigation considers three different reinforcement layouts, namely 1Y10, 2Y10 and 3Y10, and four crack spacings (S_c), as follows: single crack, $70 \leq S_c \leq 85$ mm, $85 < S_c < 100$ mm and $100 \leq S_c \leq 120$ mm. Twenty-seven $150 \times 150 \times 700$ mm long beams were sustained in flexural loading to maintain a consistent surface crack width of 0.4 ± 0.1 mm. The specimens were subjected to cyclic ponding for 36 weeks, and were monitored weekly to measure the corrosion rate and corrosion potential.

The results indicate that the corrosion rate of the RC members is influenced by a change in reinforcement density. For a given crack spacing, the corrosion rate decreased with an increase in reinforcement density. In addition, the corrosion rates were influenced by different crack spacing. It was also observed that single cracked specimens were susceptible to a higher corrosion rate than the multiply cracked

specimens. The combined effect of reinforcement density and crack spacing has shown that apart from a complex relationship between the anode and cathode region, the increase in reinforcement density has a greater influence on the corrosion rate than the increase in crack spacing.

In current practice, the onset of the corrosion propagation stage conservatively marks the end of the structure's serviceable life. A model for determining the residual service life of a structure in the corrosion propagation stage is proposed. This model may be used to gain insight regarding a structure's "corrosion state" for planning maintenance and determining its remaining service life. The study recommends that reinforcement density and crack spacing, accompanied by the prediction of residual service life, should be taken into consideration in the durability design of RC structures.

Opsomming

Die duursaamheid van 'n gewapende beton (GB) struktuur word aansienlik beïnvloed deur die teenwoordigheid van kraake. Kraake dien as weë wat die indringing van roesmiddels in die beton na die bewapening versnel. Dit veroorsaak die versnelling van beide die korrosie-inisiasie en voortsettingsfases van verwerking. Die toename in die korrosiesnelheid in die korrosie-voortsettingsfase lei tot 'n afname in die residuele diensleef tyd van 'n struktuur. Die algehele gevolg van kraake in GB-strukture is dat die oorblywende leef tyd van 'n struktuur merkwaardig verkort word.

In die afgelope jare het baie ondersoekers die korrosie van strukture in die voortsettingsfase bestudeer. Die meerderheid van hierdie ondersoekers is egter op monsters met slegs een kraak en bewapening staaf gefokus. Hierdie studie ondersoek gekraakte GB wat blootgestel is aan chloried-geïnduseerde korrosie. Die eksperimentele ondersoek beskou drie verskillende bewapeningskonfigurasies, naamlik 1Y10, 2Y10 en 3Y10, en vier kraakspasiërings (S_c), soos volg: enkele kraak; $70 \leq S_c \leq 85$ mm; $85 < S_c < 100$ mm en $100 \leq S_c \leq 120$ mm. Monsters in die vorm van $150 \times 150 \times 700$ mm lang balke is deurgans in buiging belas om 'n konsekwente oppervlakkraakwydte van die 0.4 ± 0.1 mm te behou. Die monsters is vir 'n periode van 36 weke aan sikliese toediening blootgestel en die korrosietempo en korrosiepotensiaal is weekliks gemeet.

Die resultate dui aan dat die korrosiesnelheid van die GB-lede beïnvloed word deur 'n verandering in bewapeningsdigtheid. Vir 'n gegewe kraakspasiëring het die korrosiesnelheid afgeneem met 'n toename in bewapeningsdigtheid. Daarbenewens word die korrosietempo beïnvloed deur kraakspasiëring. Daar is ook opgemerk dat enkel-kraak monsters vatbaar was vir hoër korrosie as veelvoudige-kraak monsters. Die gekombineerde effek van bewapening en kraakspasiëring het getoon dat,

afgesien van 'n komplekse verhouding tussen die anode- en katode-gebied, die toename in bewapeningsdigtheid 'n groter invloed op die korrosietempo het as die toename in kraakspasiëring.

In die huidige praktyk dui die aanvang van die korrosie-voortplantingsfase konserwatief die einde van die strukturele diensleef tyd aan. 'n Model vir die bepaling van die oorblywende dienslewe van 'n struktuur in die korrosie-voortsettingsfases word voorgestel. Hierdie model kan gebruik word om insig te verkry in 'n struktuur se "korrosietoestand" vir die beplanning van onderhoud en die bepaling van die struktuur se oorblywende diensleef tyd. Die studie beveel aan dat die bewapenings digtheid en kraakspasiërings, tesame met die voorspelling van die oorblywende dienslewe, in ag geneem moet word in die duursaamheidsontwerp van GB-strukture.

Contents

Acknowledgements	ii
Abstract	iii
Opsomming	v
1 Introduction	1
1.1 Background	1
1.2 Research aims and objectives	2
1.3 Thesis organisation	3
2 Chloride-induced corrosion in cracked reinforced concrete structures	4
2.1 General Overview	4
2.2 Electrochemical process of corrosion	5
2.3 Initiation of chloride-induced corrosion	7
2.4 Transport mechanisms in concrete	10
2.4.1 Permeation	10
2.4.2 Gaseous and ionic diffusion	11
2.4.3 Absorption	13
2.4.4 Penetrability and percolation	13
2.4.5 Effect of concrete ageing on transport mechanisms	14
2.4.6 Transport properties of cracked concrete	15
2.5 Factors affecting corrosion propagation	18
2.5.1 Effect of external exposure conditions	18
2.5.2 Effect of concrete quality (binder type and w/b ratio)	21
2.5.2.1 Binder type	22
2.5.2.2 Water-to-binder ratio (w/b)	23
2.5.3 Concrete cover	23
2.5.4 Effect of crack characteristics	25
2.5.4.1 Crack density/frequency	26
2.5.4.2 Crack width	28
2.5.4.3 Cracking at the steel-concrete interface	30
2.5.4.4 Crack geometry and orientation	31

2.5.4.5	Autogenous Crack Healing	32
2.5.5	Pitting factor	33
2.5.6	Effect of multiple reinforcement bars	35
2.5.7	Influence of loading conditions	37
2.6	Corrosion assessment and monitoring	39
2.6.1	Definition of corrosion rate	39
2.6.2	Corrosion measurement techniques	41
2.6.2.1	Polarization resistance technique	42
2.6.2.2	Galvanostatic pulse technique	43
2.6.2.3	Electrochemical impedance spectroscopy	45
2.6.2.4	Electrochemical Noise	46
2.6.2.5	Coulostatic method	46
2.6.2.6	Confinement of current	49
2.6.3	Complimentary techniques	51
2.6.3.1	Concrete resistivity	51
2.6.3.2	Half-cell potential	52
2.7	Concluding remarks	54
3	Experimental Framework	56
3.1	Introduction	56
3.2	Experimental Variables	56
3.2.1	Reinforcing Steel	56
3.2.2	Crack Density	57
3.3	Experimental Constants	59
3.3.1	Binder, Coarse and Fine Aggregate	59
3.3.2	Water/Binder Ratio	60
3.3.3	Crack width	60
3.3.4	Concrete Cover	61
3.4	Concrete Specimen Properties	61
3.4.1	Concrete mix design	61
3.4.2	Specimen dimensions and sample size	62
3.5	Casting and Curing of Specimens	63
3.6	Crack Inducement	64
3.6.1	Pre-cracking	64
3.6.2	Sustained specimen loading	67

3.7	Exposure Conditions	70
3.7.1	Ponding basin	70
3.7.2	Saline solution and ponding cycle	71
3.7.3	Laboratory conditions	71
3.8	Corrosion assessment	72
3.8.1	Modulated confinement of the current	72
3.8.2	Measurement procedure	74
3.9	Destruction of specimens	76
3.9.1	Gravimetric mass loss	76
3.9.2	Residual reinforcement capacity	77
3.10	Reinforcement Tensile Test	78
4	Experimental results and analysis	81
4.1	Introduction	81
4.2	General visual observations	81
4.3	Corrosion rate results	84
4.3.1	General overview of corrosion rate results	84
4.3.2	Effect of crack density on corrosion rate	87
4.3.3	Effect of reinforcement density on corrosion rate	89
4.3.4	Correlation between crack density and reinforcement density	90
4.4	Corrosion potential results	92
4.4.1	General overview of corrosion potential results	92
4.4.2	Relationship between corrosion potential and corrosion rate	95
4.5	Mass loss results	97
4.5.1	Electrochemical mass loss	97
4.5.2	Gravimetric mass loss	100
4.5.3	Relationship between electrochemical and gravimetric mass loss	100
4.6	Reinforcement tensile capacity results	102
4.6.1	Relationship between tensile capacity and corrosion rate	102
5	Towards residual service life prediction	106
5.1	Introduction	106
5.2	Steel-stress level	107
5.2.1	Analytical calculation of steel-stress level	107
5.2.2	Relationship between steel-stress level and corrosion rate	112
5.3	Empirical corrosion rate prediction models	114

5.3.1	Review of existing empirical models	114
5.3.1.1	Morinaga (1988)	114
5.3.1.2	Vu et al. (2005)	115
5.3.1.3	Scott (2004)	116
5.3.1.4	Otieno (2014)	117
5.3.2	Analysis of existing empirical models	118
5.3.3	Model input parameter limitations	119
5.4	Residual service life prediction	120
5.4.1	Definition of residual service life	120
5.4.2	Relationship between residual service life and corrosion rate . .	120
5.4.3	Relationship between service life and reinforcement diameter . .	121
5.4.4	Analysis of a proposed residual service life prediction model . .	122
6	Conclusions and recommendations	126
6.1	Conclusions	126
6.1.1	Effect of multiple reinforcement rods on corrosion rate	126
6.1.2	Effect of crack spacings on the corrosion rate	127
6.1.3	Combined effect of crack spacing and reinforcement density . . .	128
6.1.4	Effect of steel stress on corrosion rate	128
6.1.5	Effect of corrosion rate on the residual service life	129
6.1.6	General conclusions	130
6.2	Recommendations	130
	Appendices	141
	A Appendix A	142
A.1	Specimen pre-cracking	142
A.2	Crack spacings	146
	B Appendix B	147
B.1	Residual service life prediction model	147
	C Appendices	151
C.1	Product details	151
C.1.1	GECOR-10 [®]	151
C.1.2	Alcolin [®]	151

List of Figures

2.1	Three stage corrosion damage model (Heckroodt 2002)	5
2.2	Corrosion process in concrete	6
2.3	Schematic representation of pitting in RC (Bertolini et al. 2013)	9
2.4	Typical corrosion products of iron (reproduced from Jaffer et al. (2009))	9
2.5	Typical chloride profile for concrete situated in the marine splash zone (Böhni 2005)	12
2.6	Schematic of ITZ relation to penetrability and percolation (Alexander et al. 2010)	14
2.7	Influence of w/b ratio and RH on oxygen diffusion coefficient (Bentur et al. 1997)	19
2.8	Submerged concrete specimens (Adiyastuti 2005)	20
2.9	Laboratory based ponding setup	21
2.10	Corrosion rate in various cement compositions (reproduced from Scott et al. (2007))	22
2.11	Concrete cover vs. O_2 diffusion (reproduced from Bentur et al. (1997))	24
2.12	Causes of cracking in RC structures (adapted from CEB (1992))	25
2.13	Effect of crack frequency on the cumulative mass loss due to corrosion (reproduced from Arya et al. (1996))	27
2.14	Effect of crack width and concrete composition on corrosion rates (reproduced from (Otieno et al. 2010))	29
2.15	Schematic of primary and secondary (internal) cracks (Goto 1971)	30
2.16	Computed strain overlay on specimens with different loading conditions (Pease 2010)	31
2.17	Stereoscopic images of concrete in fresh water (Palin et al. 2015)	32
2.18	Stereoscopic images of concrete in sea water (Palin et al. 2015)	33
2.19	Schematic of general vs. pitting corrosion (Andrade et al. 2017)	34
2.20	Schematic geometry of corroding steel bar (adapted from Andrade et al. (2001, pg. 145))	34
2.21	Macro-cell vs. micro-cell corrosion (Hansson et al. 2006)	36
2.22	Sustained loading versus pre-loading (reproduced from Yoon et al. (2000))	38
2.23	Schematic of equivalent homogenous loss in g/cm^2 (reproduced from Andrade et al. (1996))	40

2.24 Schematic of localized attack and length error (reproduced from Andrade et al. (1996))	41
2.25 Schematic of linear region about the corrosion potential (adapted from Poursaei (2010))	43
2.26 Typical galvanostatic pulse result (Poursaei 2010)	44
2.27 Schematic plot of equation 2.23 (Newton et al. 1988)	45
2.28 Schematic of coulometric technique circuitry (Chu et al. 2006)	47
2.29 Example of Coulometric corrosion rate measurement (Paul 2015)	48
2.30 Unconfined vs. confined corrosion current measurement	49
2.31 Schematic confinement of current circuitry (adapted from Andrade et al. (1996))	50
2.32 4-Point Wenner probe technique	51
2.33 Scatter of I_{corr} vs. resistivity (Alonso et al. 1988)	52
2.34 Schematic half-cell potential circuit (Broomfield 2002)	53
2.35 HCP reference electrode components (Paul 2015)	54
3.1 Specimen cross-section configurations (dimensions in mm)	57
3.2 Top view of specimen notch configurations (dimensions in mm)	58
3.3 Aggregate grading curves	60
3.4 Typical 150 x 150 x 700 mm concrete specimen	63
3.5 Summary of experimental variables and sample size	63
3.6 (a) Specimen mould prior to, and (b) after casting	64
3.7 Specimen pre-cracking in MTM	65
3.8 Typical specimen response	66
3.9 Schematic of 4-point loading rig (dimensions in mm)	68
3.10 Surface crack distribution	69
3.11 Typical crack formation	70
3.12 Specimen ponding basin on tensile face	71
3.13 Photograph of some of the laboratory specimens	72
3.14 Measurement of corrosion rate with GECOR-10	74
3.15 Locations of corrosion rate readings (dimensions in mm)	75
3.16 14-Day measurement and ponding schedule	76
3.17 Corroded Y10 anode region length (L_{anode})	78
3.18 Tensile test in Zwick Z250 MTM	79
3.19 Reinforcement tensile capacity results	80

4.1	Experimental study specimen notation	81
4.2	Typical crack and coinciding anodic regions	82
4.3	Typical single crack specimens prior to cleaning with <i>HCl</i>	83
4.4	Typical multiple cracked specimens prior to cleaning with <i>HCl</i>	84
4.5	Typical corrosion rate time-development graphs	85
4.6	Typical corrosion rate time-development graphs	86
4.7	Average corrosion intensity between different crack spacings	88
4.8	Schematic of anode to cathode ratio	88
4.9	Average corrosion intensity for different reinforcement layouts	89
4.10	Schematic of anode to cathode ratio in multiple reinforcement beams	90
4.11	Average corrosion rates after 36 weeks	91
4.12	Correlation between crack spacing and reinforcement layout	91
4.13	Typical corrosion potential time-development graphs	93
4.14	Typical corrosion potential time-development graphs	94
4.15	Corrosion rate vs. corrosion potential	96
4.16	Average i_{corr} vs. E_{corr}	97
4.17	Average reinforcement layout electrochemical mass loss over time	98
4.18	Average crack spacing electrochemical mass loss over time	99
4.19	Initial weight vs. final weight	100
4.20	Crack spacing vs. mass loss	101
4.21	Reinforcement density vs. mass loss	102
4.22	Yield force between uncorroded and corroded reinforcement bars	103
4.23	Relationship between loss of yield force and the mass loss of the steel bar	104
5.1	Concrete strain at surface and transmission length, adapted from Blagojević (2015, pg. 133)	109
5.2	Relation between steel-stress level and surface crack width	111
5.3	Relation between steel-stress level and surface crack width	112
5.4	Relationship between steel stress and corrosion rate	113
5.5	Otieno et al. (2016) prediction vs. measured i_{corr}	118
5.6	Predicted i_{corr} vs. measured i_{corr} for varying cover depths	119
5.7	Residual time before the attainment of a 15% limit state	121
5.8	Relationship between reinforcement diameter and residual service life	122
5.9	Limit states of Y10 reinforcement rod, $\alpha_{pit} = 5$	123
5.10	Residual service life's of reinforcement rods, $LS = 15\%$ and $\alpha_{pit} = 5$	123
5.11	Residual service life between different α_{pit} factors, Y10 and $LS = 15\%$	124

LIST OF FIGURES

A.1	Pre-cracking specimen response for single reinforcement (R1)	143
A.2	Pre-cracking specimen response for double reinforcement (R2)	144
A.3	Pre-cracking specimen response for tripple reinforcement (R3)	145
B.1	Reisdual service life for $\alpha_{pit} = 1$	148
B.2	Reisdual service life for $\alpha_{pit} = 5$	149
B.3	Reisdual service life for $\alpha_{pit} = 10$	150
C.1	GECOR-10 instrument components (<i>isdcorr 2015</i>)	151
C.2	Typical Alcolin silicone	152

List of Tables

2.1	Total chloride threshold values of recent studies	8
2.2	Chloride-induced corrosion environmental marine classes (EN-206 (2000))	18
2.3	Corrosion rates of different w/b ratios (Mangat et al. 1994)	23
2.4	Allowed crack width for RC structures exposed to chloride-induced corrosion	29
2.5	Typicall suggested pitting factors for corroding RC	35
2.6	Corrosion intensity classification (Andrade et al. 1996)	41
2.7	Corrosion probability for half-cell potential (ASTM 2015)	53
3.1	Concrete mix proportions	62
3.2	Concrete compressive strength properties	62
3.3	Flexural pre-cracking loads	67
3.4	Summary of specimen crack spacings	70
3.5	Y10 reinforcement mechanical properties	80
5.1	Conversion between corrosion units	106
5.2	Conversion between units of corrosion for F_e	107
5.3	General experimental properties	107
5.4	Model input parameters for i_{corr} prediction	118
A.1	Flexural pre-cracking responses	142
A.2	Flexural pre-cracking responses	146

Nomenclature

Abbreviations

AC	Alternating current
ASR	Alkali-Silica reaction
BFS	Blast furnace slagment
C & CI	Cement and Concrete Institute
CE	Counter electrode
CoV	Coefficient of Variation
CSE	Copper-copper sulphate electrode
CSF	Condensed silica fumes
EIS	Electrochemical impedance spectroscopy
EN	Electrochemical noise
FA	Fly Ash
FM	Fineness modulus
GRCE	Guard ring counter electrode
GGBS	Ground Granulated Blast-furnace Slagment
GGCS	Ground granulated Corex slagment
HCP	Hardened cement paste
ITZ	Interfacial transitional zone
LPR	Linear polarization resistance
LS	Limit state
MCC	Modulated confinement of current

MTM	Materials Testing Machine
OPC	Ordinary Portland Cement
PAT	Potential attenuation technique
R/SHCC	Reinforced strain hardening cement-based composite
RC	Reinforced concrete
RH	Relative Humidity
SCE	Silver-silver chloride electrode
SCM	Supplementary cementitious materials
SLS	Serviceability limit state
TR	Transient response
ULS	Ultimate limit state
w/b	Water-to-binder ratio
Y10	High yield stress 10 mm diameter ribbed steel bar

Terminology

α_{pit}	Pitting concentration factor
σ_y	Yield stress
A_{st}	Cross-sectional area of steel
E_s	Elastic modulus
f_{cu}	Ultimate compressive strength
F_c	Characteristic yield force
F_y	Yield force
i_{corr}	Corrosion intensity
L_{anode}	Anodic region length

S_c	Crack spacing
T_{init}	Corrosion initiation period
T_{prop}	Corrosion propagation period
T_{RSL}	Residual service life period
w_c	Crack width
CCI_{90}	90-day chloride conductivity index
D_{90}	90-day diffusion coefficient

1. Introduction

1.1 Background

Reinforced concrete structures can be damaged by various deterioration mechanisms that greatly effects the structure's durability. One of the major threats to the durability of reinforced concrete (RC) structures is the corrosion of the reinforcing steel embedded in the concrete. Corrosion of reinforcement in concrete members potentially causes reduced service life and additional maintenance as well as rehabilitation costs. Among the various degradation mechanisms associated with the corrosion of reinforcement, two of these mechanisms are highlighted locally and globally as many investigations have been undertaken to understand their kinetics.

Carbonation is the neutralising reaction in which the pH of concrete is lowered. This occurs when atmospheric carbon dioxide reacts with water in the concrete and forms carbonic acid. This reaction is typical to urban industrial environments and may induce corrosion of reinforcing steel in RC. The second mechanism of degradation is chloride attack. It is a more important cause of degradation to worldwide coastal structures (Blagojević 2015). Therefore, this investigation covers the fundamentals of corrosion of reinforcement with an emphasis on chloride-induced corrosion.

Steel is susceptible to oxidation in the air to a more stable form. Therefore, to benefit from the economical and versatile properties of RC, a steel rod is encased in concrete to protect it from the external environment. In the past, the degradation of RC structures has mainly been based on the Tuutti (1982) model of two stage degradation. The initial, unaffected stage of corrosion initiation is defined as the period before active corrosion. The second stage, corrosion propagation, is defined as the period where expansive corrosion products are produced and result in cover cracking and spalling.

However, this two-stage model has in recent years been expanded to incorporate an acceleration stage. This additional stage provides better clarification between the corrosion propagation and corrosion acceleration. Within the corrosion acceleration stage, the RC member degradation increases rapidly, while the corrosion rate

potentially reaches its maximum.

The corrosion propagation stage serves as an important link between the initiation period and the acceleration period. This is due to the fact that the degradation of the structure is directly linked to the corrosion rate in the propagation stage. In other words, the higher the corrosion rate in the propagation stage, the shorter the residual service life of the structure. The aim of this study is to focus on the corrosion rate in cracked concrete in the propagation stage in order to investigate the mechanics and influences within this important stage. Knowledge of the propagation stage could be of aid to the engineers on whether or not rehabilitation is needed, or if the structure will be able to serve as intended for the residual service life of the structure.

1.2 Research aims and objectives

The aim of this study is to explore the effects of multiple reinforcement rods and crack spacings on the corrosion rate of cracked reinforced concrete beams when exposed to chloride-induced corrosion. This is investigated to improve the understanding of the governing factors on the physical electrochemical processes and their potential interwoven effect. This will consequently lead to more accurate predictions of the residual service life of concrete members in the corrosion propagation stage.

A test methodology is designed to achieve the following objectives:

1. To explore the effects of multiple reinforcement rods on the corrosion rate in the corrosion propagation stage. This is investigated to gain an insight into the electrochemical process between multiple reinforcement rods in reinforced concrete structures.
2. To compare and explore the effect(s) of different crack spacings on the corrosion rate for cracked concrete in the marine environment. This aids the aim of this investigation by improving the understanding of the difference between a singular crack and multiple cracks in corroding RC members.
3. Investigate the combined effects of different crack spacings and reinforcement densities on the corrosion rates of cracked RC members. Knowledge in this regard will assist future on-site corrosion assessments.

4. Explore the effects in steel-stress level of the reinforcement rods on the corrosion rates. This is investigated to aid the understanding of the influence of multiple reinforcement rods on the corrosion rate.
5. To investigate the effects of corrosion rates and other accompanying factors to the residual service life of a structure.
6. Synthesize the obtained information regarding the reinforcement density, crack spacing and steel-stress level to aid the understanding of corrosion rates, and consequently the prediction residual service life, for cracked concrete members in the marine environment.

1.3 Thesis organisation

The remainder of the thesis is structured as follows:

Chapter 1 gives a general introduction to reinforcement corrosion in concrete structures with an emphasis on marine environments. A brief overview of the durability performance of cracked concrete is then given, followed by some insight on the current service life prediction for RC structures situated in coastal environments.

Chapter 2 is concentrated on the literature associated with the fundamentals of reinforcement corrosion, the accompanying factors that influence it and the assessment thereof. The focus of this investigation is on chloride-induced corrosion.

Chapter 3 focuses on the experimental methodology and technical approaches of this study.

Chapter 4 presents the experimental results obtained in this investigation, followed by the discussions of the experimental outcome.

Chapter 5 is focused on the approach towards residual service life predictions, based on the loss of cross-sectional area of the reinforcement.

Chapter 6 concludes the evaluation, discussion and findings of the experimental results obtained in this study, and recommends future work.

2. Chloride-induced corrosion in cracked reinforced concrete structures

2.1 General Overview

Up until now, the corrosion degradation of reinforced concrete (RC) structures has largely been based on the Tuutti (1982) model of two stage degradation. The first stage of degradation, corrosion initiation, is defined as the period before the onset of active corrosion. This period of time can generally last years, depending on the external exposure conditions, concrete quality and loads the member is subjected to. If no cracks are formed on the surface of the member, the corrosion process is generally dependant on the transport properties of the concrete member. This is due to the fact that corrosion constituents have to travel through the concrete matrix to reach the reinforcement before active corrosion can commence.

However, in the presence of cracks, the corrosion initiation stage can be significantly shortened as paths exist for harmful corrosion constituents to reach the reinforcement. The structure now enters the corrosion propagation stage whereby expansive corrosion products are produced resulting in cover cracking and spalling. In order to distinguish between acceleration of corrosion rate and before the corrosion rate potentially reaches the maximum rate, a third stage has in recent years been introduced. This stage is referred to as the corrosion acceleration stage. This three stage degradation model is illustrated in figure 2.1.

2.2 Electrochemical process of corrosion

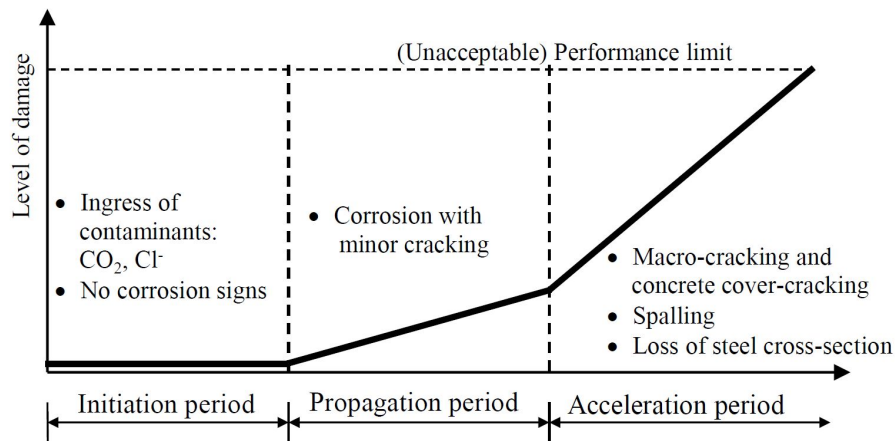


Figure 2.1: Three stage corrosion damage model (Heckroodt 2002)

The three-stage model better incorporates the differences between passive corrosion (no visual damage), the corrosion propagation stage (small visual hints of active corrosion) and the accelerated stage whereby chlorides, moisture and oxygen are freely allowed through the cracks and the reinforcement is generally considered to be exposed to the external environment. At the time the structure reaches the accelerated corrosion stage, high costs of rehabilitation can be expected whilst at the same time higher risks of structural failure are supposed accompanied by the end of service life are anticipated.

Prior to covering the mechanisms that influence the corrosion rate in the corrosion propagation stage, sections 2.2 and 2.4 briefly cover the fundamentals of the corrosion process that lead to the corrosion initiation process.

2.2 Electrochemical process of corrosion

The electrochemical process of steel corrosion is caused by the inherent instability of metals in metallic form and the tendency of these metals to want to revert to a more stable form, for example, to oxides, hydroxides and sulphides (Heckroodt 2002). This process is accelerated when the steel is exposed to a reactive environment. In this environment the reinforcing forms two regions, the anode and the cathode. The anode region is where corrosion occurs and from which electrons flow, and in contrast, the cathode is the passive region to which the electrons flow. Between the anode and cathode the concrete pore solution acts as an electrolyte which conducts the flow of

2.2 Electrochemical process of corrosion

hydroxyl ions. The circuit is completed by the steel bar when the current flows back from the anode to the cathode as shown in figure 2.2. The positively charged iron ions, Fe^{2+} , dissolve in water and the electrons are set free, shown in equation 2.1. Equation 2.2 shows how these free electrons, e^- , flow toward the cathodic region where they are combined with the electrolyte constituents, oxygen (O_2) and water (H_2O), to form hydroxyl ions (OH^-) (Neville 1995).

Anodic Region:



Cathodic Region:

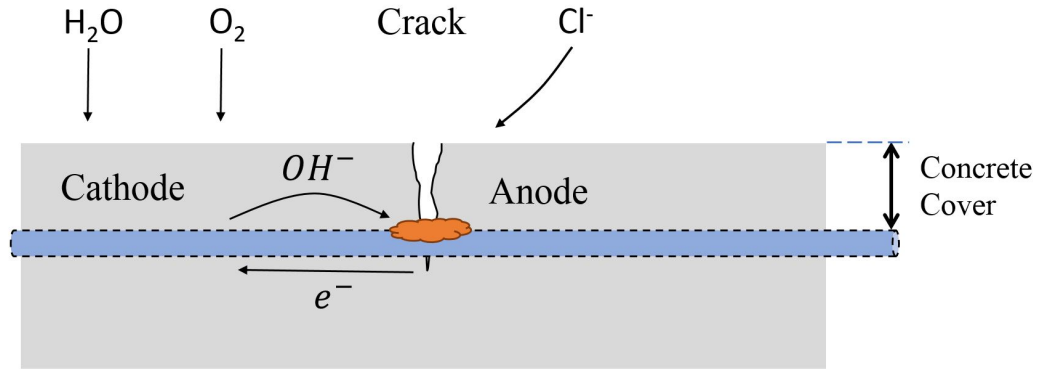
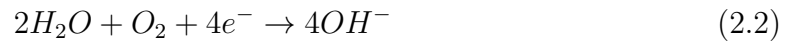
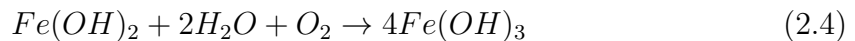
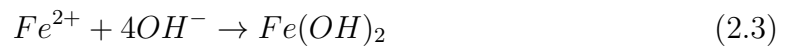


Figure 2.2: Corrosion process in concrete

The hydroxyl ions then combine with the moving Fe^{2+} ions to form ferrous hydroxide, $Fe(OH)_2$ shown in equation 2.3. Thereafter, the $Fe(OH)_2$ is converted to rust by oxidation as shown in equation 2.4. There are other forms of iron complexes that can be formed; these alternative corrosion products are shown in figure 2.4 and is discussed in section 2.3.



From the above equations it can be seen that water and oxygen are needed for the continuous process of corrosion. Therefore, factors such as relative humidity (RH)

2.3 Initiation of chloride-induced corrosion

and concrete saturation level are important. In dry concrete no significant corrosion will take place under a high level of electrical resistivity. Similarly, in fully saturated concrete no significant corrosion will take place due to the prohibition of diffusion of oxygen to reach the cathodic region. Conversely, a high corrosion rate will occur when the concrete is partly saturated due to the conductivity of the concrete.

2.3 Initiation of chloride-induced corrosion

Chloride penetration is an important factor when inducing corrosion in RC structures due to the pH reducing effect of the penetrating chloride. The hydration process of cement in the concrete results in a high alkaline environment, typically between $12.4 \leq \text{pH} \leq 14$, as a result of the sodium and potassium hydroxide. This alkaline environment aids the protection of the reinforcement bar by forming a thin passive layer on the surface of the steel bar that is secure from any mechanical damage. The passive layer is typically a few nanometres thick and is composed of different degrees of hydrated iron oxide (Fe^{2+} and Fe^{3+}). When the chloride comes into contact with the passive film, it reduces the resistance of the passive film by lowering the pH. This process of corrosion is referred to as the depassivation of the reinforcement bar (Paul 2015). As soon as the passive layer of ferric oxide is broken down, active corrosion starts and can be measured even at negligible to low corrosion rates. For the acceleration of the corrosion process, a certain concentration of chlorides is needed at the reinforcement level. This concentration is described as the chloride threshold level (or critical chloride concentration) and is an important input parameter in corrosion rate prediction models. This chloride level is affected not only by the environmental RH and temperature but also the concrete cover, binder chemistry and the reinforcement electrical potential (Nilsson et al. 1996). Therefore, a single level cannot be chosen for all types of concrete. Different approaches have been investigated to express the chloride threshold level. Two of these approaches are that of total chlorides to free chlorides and chloride to hydroxyl ion ratio. Table 2.1 shows some recommended total chloride threshold values based on the percentage of binder mass.

2.3 Initiation of chloride-induced corrosion

Table 2.1: Total chloride threshold values of recent studies

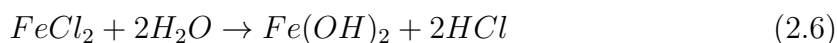
Reference	Binder type	Chloride threshold (% by mass of binder)
Trejo et al. (2003)	OPC ^a	0.02 - 0.24
Scott (2004)	Various binders	0.08 - 0.53
Lambert et al. (1991)	OPC ^a and SRPC ^b	1.0 - 3.0
Alonso et al. (2000)	OPC ^a	1.24 - 3.08

^a Ordinary Portland cement

^b Sulfate resisting Portland cement

These studies show that chloride threshold values are difficult to define as table 2.1 has a range of 0.02 to 3.08 %. The range might have been smaller if a standardised testing procedure is adopted. A standardised procedure will be more appropriate if a binder-specific chloride threshold concentration would be defined. Despite this large range, most authors use a conservative value of 0.4 % total chlorides by mass of cement when performing corrosion studies (Daigle et al. 2004).

If the chloride concentration is high enough at the reinforcement level, the chloride ions will act as a catalytic agent in the corrosion process. Once the corrosion process is initiated, localized pitting corrosion, being one of the most common types of chloride-induced steel corrosion mechanisms, takes place. This process is shown in figure 2.3. This creates an aggressive environment within the pitting region and allows steel corrosion to take place in a highly localized small anode within the pit. If the chloride concentration is high in the surrounding reinforcement, corrosion will not be limited to the pitting region. Therefore, the corrosion attack can involve the surrounding areas. The mechanism remains the same by lowering the pH of the concrete as described by equations 2.5 to 2.7.



2.3 Initiation of chloride-induced corrosion

As the ferric chloride, $FeCl_2$, lowers the pH of concrete the pit area increases. This reduction in pH is also assisted by the formation of oxychloride, $FeOCl$, within the same reaction and therefore aids further corroding the reinforcement. This process becomes self-propagating as the chloride ions are set free by hydrolysis (equations 2.6 and 2.7) and combine with Fe^{2+} to form more ferric chloride as shown in figure 2.3.

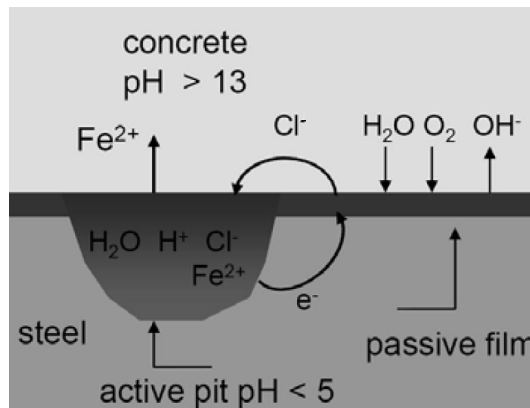


Figure 2.3: Schematic representation of pitting in RC (Bertolini et al. 2013)

The corrosion products formed by the corrosion process are the fundamental cause of eventual concrete cover peeling or spalling. It is important to note that the corrosion products have volumes several times greater than the unit volume of the initial steel bar. The most common corrosion products are shown in figure 2.4.

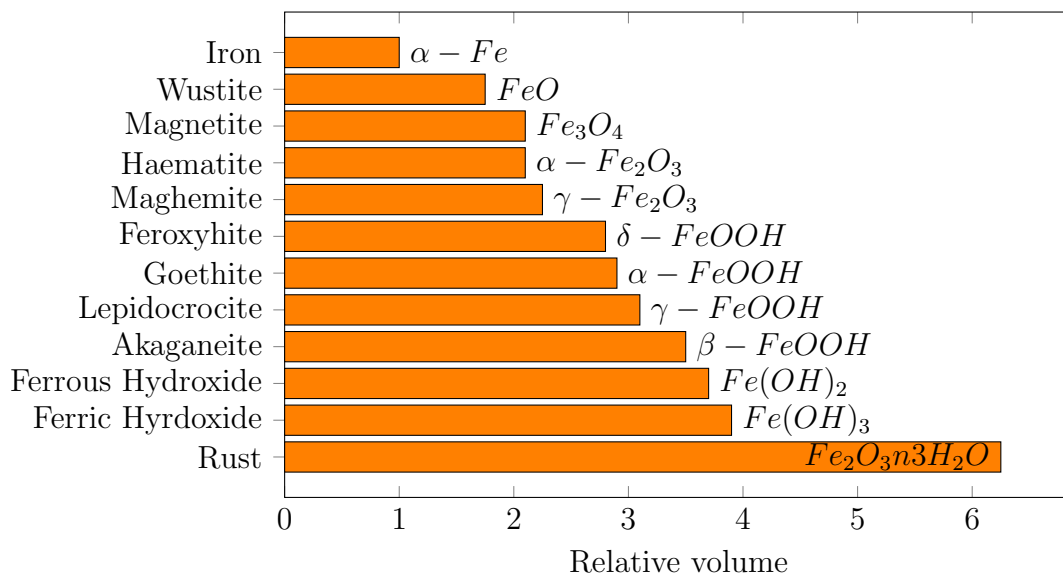


Figure 2.4: Typical corrosion products of iron (reproduced from Jaffer et al. (2009))

2.4 Transport mechanisms in concrete

From figure 2.4, rust ($Fe_2O_3 \cdot nH_2O$) has a unit volume of roughly six times greater than that of the corroding steel bar (Fe). This rust causes high expansion forces at the reinforcement level and surrounding pores where the rust product accumulates. Thus, after time and enough build-up, rust creates more micro-cracks and passages for Cl^- , H_2O and O_2 to flow. This opening of micro-cracks leads to wider cracks while also spawning more micro-cracks, and consequently lead to the spalling of the concrete cover (Blagojević 2015; Zhou et al. 2014).

2.4 Transport mechanisms in concrete

The durability performance of concrete is fundamentally associated with how well the concrete matrix retards the ingress of harmful substances that can corrode the reinforcement. Therefore, the transport properties of the cementitious material are major factors for ensuring durability. The penetrability of the concrete is defined as the degree to which the concrete allows harmful substances to transport through the concrete matrix through mechanisms of ingress. These mechanisms include diffusion, permeation and capillary absorption. Transport mechanisms can be modelled (Alexander et al. 2010) for the prediction of time to cracking and for the consideration of durability regarding other deterioration processes (Liu 1996). The permeability of the concrete matrix is influenced by the aggregate to cement paste bond and the interfacial transition zone (ITZ) through which harmful substances can more easily migrate. Each of the transport mechanisms are briefly described in the following subsections.

2.4.1 Permeation

The capability of concrete to transfer fluids and gasses through its pore structure under an external pressure while the pores of the concrete remain saturated with that fluid is referred to as the permeability of concrete (Wang et al. 1997). This permeability is directly related to the pressure gradient which drives the liquids and gasses through the pore structure from a region of high pressure to a region of low pressure. The average velocity of substance flow is determined through Darcy's law in equation 2.8.

$$\bar{v} = \left(\frac{k}{n}\right) \cdot \left(-\frac{dh}{dx}\right) \quad (2.8)$$

2.4 Transport mechanisms in concrete

Where \bar{v} is the velocity, k is the coefficient of permeability, n is the porosity, h is the hydraulic head and x is the distance.

2.4.2 Gaseous and ionic diffusion

Diffusion of chloride ions in concrete is defined as the movement of ions from a region of high concentration to a region of lower concentration, driven by the concentration gradient. Ionic diffusion takes place if the concrete matrix is partially saturated or fully saturated, whereas gaseous diffusion takes place in unsaturated concrete (Sharif et al. 1999). According to a study done by Vu et al. (2000), chloride ion penetration is best represented by the diffusion process where the concrete is assumed to be saturated. Modelling of ionic and gaseous diffusion is often done through applying Fick's first law (for steady state diffusion) for the rate of diffusion of a fluid or ion into a uniformly permeable material as shown in equation 2.9 (Richardson 2003).

$$J = -D_{eff} \cdot \frac{dC}{dx} \quad (2.9)$$

where J is the mass transport rate, D_{eff} is the effective diffusion coefficient, C is the concentration of fluid and x is the distance.

The rate of gaseous diffusion is greatly affected by the moisture content of the concrete. A dry concrete medium promotes the flow of gaseous molecules through the pores of the concrete. In contrast, saturated concrete pores will limit gaseous diffusion. The rate of diffusion can be 10^4 to 10^5 times greater in gas phase than in liquid phase for gases such as carbon dioxide and oxygen (Richardson 2003).

Ionic diffusion, on the other hand, requires a saturated medium and a concentration difference. The saturated concrete matrix allows the chloride ions to use the free water as a passage for ionic diffusion. Using Fick's second law, shown in equation 2.10, and in certain conditions, the error function solution by Crank, the ionic diffusion can be modelled as shown in equation 2.11 (Richardson 2003).

$$\frac{\partial C}{\partial t} = D \cdot \frac{\partial^2 C}{\partial x^2} \quad (2.10)$$

for: $C_X = 0$ at $t = 0$ and $0 < x < \infty$

for: $C_X = C_S$ at $x = 0$ and $0 < t < \infty$

2.4 Transport mechanisms in concrete

$$\frac{C_X}{C_S} = 1 - \operatorname{erf}\left(\frac{X}{2 \cdot (D \cdot t)^{0.5}}\right) \quad (2.11)$$

where C_X is the chloride concentration at depth x at time t , C_S is the surface chloride concentration, t is the time of exposure and D is the diffusion coefficient.

Diffusion properties are important for modelling the residual service life in RC structures in coastal regions. Diffusion is one of the dominant transport mechanisms to transport oxygen and chloride ions to the reinforcement level. Crank's error function is often used in conjunction with Fick's second law for chloride profile analysis. A typical measured chloride profile for concrete situated in the tidal splash zone is shown in figure 2.5. For this example, Fick's second law has been plotted for various data points, ignoring those in the convection zone. In this figure, the initial chloride background level is denoted as C_i , and the surface chloride concentration at depth x is denoted as $C_{S,\Delta X}$. Furthermore, the convection zone refers to the region where the concrete is susceptible to the influence of the external environment drying out the concrete.

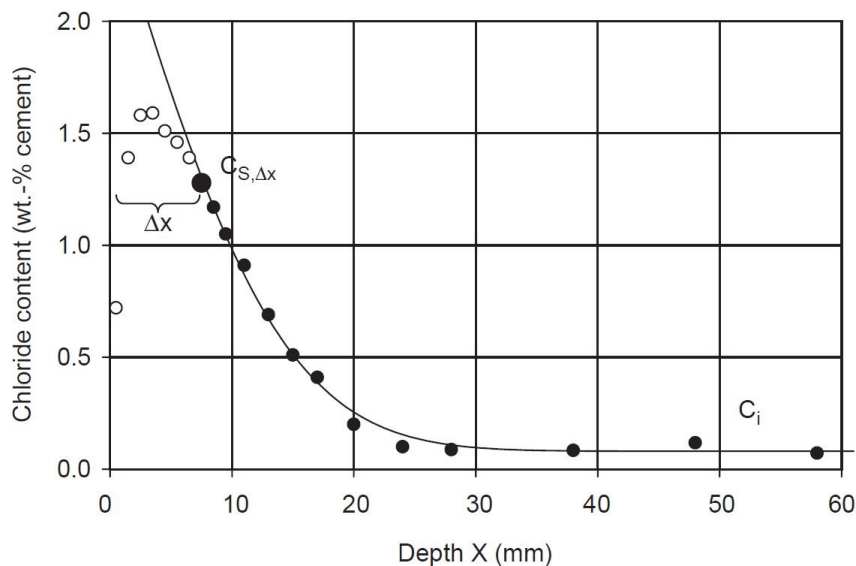


Figure 2.5: Typical chloride profile for concrete situated in the marine splash zone (Böhni 2005)

The diffusion coefficient for a concrete member can be estimated using Fick's second law of diffusion. In conditions where the diffusion coefficient and surface

2.4 Transport mechanisms in concrete

concentration of chloride ions are known, durability predictions can be made based on the depth and rate of chloride penetration.

2.4.3 Absorption

Absorption (capillary action) causes the ingress of fluid into the concrete member. It is important to note that capillary action is not related to permeability, but rather to the pore structure of the concrete. The transportation of liquid is caused by the pressure difference across the meniscus of the pore (Richardson 2003). Therefore, the rate of movement (sorptivity), is influenced by the degree of interconnection and size of the pores. Sorptivity may be defined by equation 2.12 (Alexander et al. 2010).

$$S = \frac{\Delta M_t}{\sqrt{t}} \cdot \left(\frac{d}{M_{sat} - M_{dry}} \right) \quad (2.12)$$

where $\Delta M_t/t^{1/2}$ is the slope of the straight line produced when the mass of water absorbed is plotted against the square root of time, d is the thickness of the sample and M_{sat} & M_{dry} is the saturated and dry mass of the concrete respectively.

Sorptivity is greatly influenced by the pores on the exposed surface. Therefore, the hydration of the outer surface of the concrete member (curing), compaction, mix composition and aggregate orientation are important for durability performance (Kropp et al. 2007).

2.4.4 Penetrability and percolation

Penetrability refers to the collection of mechanisms: permeation, diffusion, absorption and conduction. Percolation refers to whether or not a material is penetrable. The matrix of all concrete members is inherently penetrable and porous as shown in figure 2.6. The interfacial transitional zone (ITZ) refers to the phase that forms between the aggregate and the cement matrix (or paste). This zone generally has a higher penetrability than that of the hardened cement paste, allowing preferential paths for fluid movement. ITZ is typically between 20 and 50 μm thick and the more dispersed the aggregate, the less percolated as illustrated in figure 2.6 (Owens 2009).

2.4 Transport mechanisms in concrete

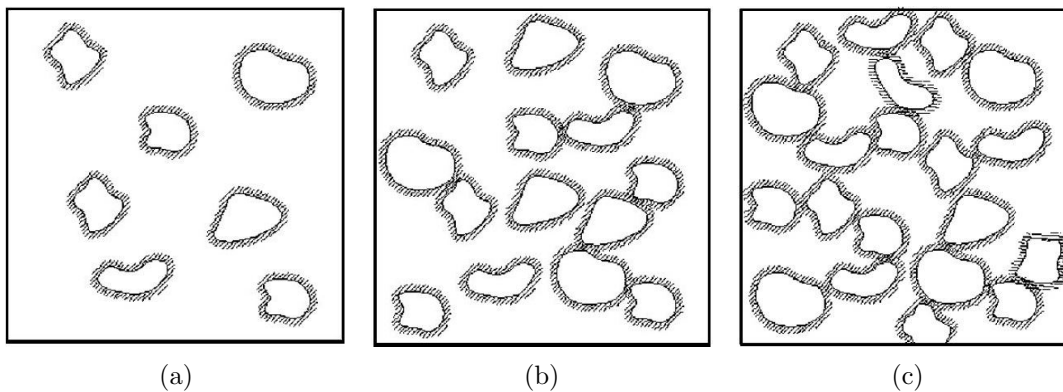


Figure 2.6: Schematic of ITZ relation to penetrability and percolation (Alexander et al. 2010)

In figure 2.6, the ITZ defines the level of penetrability and the percolation of the concrete. The schematic uses the three situations: (2.6a) a wide dispersion of the aggregate particles which makes penetrable fluid paths through the ITZ unavailable and is unpercolated; (2.6b) aggregate dispersion decreases, resulting in some ITZs overlapping and creating some fluid movement paths; (2.6c) much higher aggregate concentration leading to many overlapping ITZs resulting in longer and more fully connected fluid transport paths and is therefore referred to as percolated.

There are, however, many factors regarding the aggregates that affect the ITZ. Very fine aggregates ($<100\ \mu\text{m}$), have the reverse effect as they act as “fine fillers” which increase durability and ITZ properties (Owens 2009). By refining the ITZ, durability is increased. This is typically done in practice with the addition of ultra-fine mineral additives such as condensed silica fumes (CSF). Without the use of CSF, overlapping ITZs would be present and result in percolated pathways as well as the ease of fluid movement through the concrete member (Winslow et al. 1994).

2.4.5 Effect of concrete ageing on transport mechanisms

The hydration process in concrete occurs throughout the entire service life, therefore, the porosity and continuity of the capillary pores may change over time. The continuous hydration of the cementitious material may be one of the main reasons for the change in micro-structure. However, there are other factors that also need to be accounted for, such as the deterioration of the concrete over time. Effects on

2.4 Transport mechanisms in concrete

the concrete (for example leaching and cracking) can have an influence on concrete deterioration as new pathways and subsequently, new capillary pores form leading to new fluid movement mechanisms. Another important process is chloride binding as this significantly affects the long-term durability of concrete members relative to the short-term assessment of experimental concrete members in the laboratory. The continuous effects of cementitious hydration and chloride binding is described by the relation presented in equation 2.13 (Mackechnie 1995).

$$D(t) = D_0 \cdot \left(\frac{t_0}{t}\right)^n \quad (2.13)$$

where $D(t)$ is the time dependant diffusion coefficient, D_0 is the diffusion coefficient at reference time (typically 28 days) and n is the ageing coefficient (reduction factor).

The ageing coefficient, which influences the hydration of the concrete over time, depends on the type of binder used. The long term durability performance of concrete has not been extensively studied and therefore, concrete ageing relationships for members older than 25 years do not yet exist.

2.4.6 Transport properties of cracked concrete

The durability of concrete is mainly influenced by the concrete's ability to prevent aggressive substances from flowing through the concrete. In the prediction of concrete durability, it is vital to understand how substances flow through cracks, as most deterioration mechanisms are enhanced in the cracked concrete state. Transport properties within concrete members are considerably altered in the presence of cracks. Different types of cracks will also alter the associated transport mechanisms. For example, connected macro-cracks have different predominant transport mechanisms when compared to those of discrete and well distributed micro-cracks. This coupled phenomenon between the crack and the matrix is important for understanding the transport mechanisms in cracked concrete (Boulfiza et al. 2003).

The different transport processes inherently have different kinetics, for example different accelerators and/or retarders. Therefore, the changes resulting from cracking depend greatly on the predominant transport mechanism (Rodriguez et al. 2003; Weiss et al. 2007). This implies that the flow of substances through the concrete member is assessed based on to the state of the concrete. In uncracked concrete, the

2.4 Transport mechanisms in concrete

rate of substances intruding the concrete is mainly linked to the penetrability of the concrete as discussed in section 2.4. However, in cracked concrete, the properties of the cracks become more important than the properties of the concrete (e.g. porosity) because of their significant contribution in allowing aggressive substances to enter the concrete member.

Diffusion, advection and capillary suction are the three main transport mechanisms associated with cracked concrete, especially under aggressive exposure conditions (wetting and drying cycles) which allow the chlorides to penetrate deep into the concrete member (Win et al. 2004). There are limited studies that investigate the relationship of cracking with the overall penetrability of the concrete (Samaha et al. 1992) and even less numerical simulations dedicated to quantifying the penetrability of chloride ions in cracked concrete (Marsavina et al. 2009).

The investigation of transport properties in cracked concrete is an important consideration in the durability assessment of a RC member. This consideration should include the following parameters (Breyse et al. 1997):

- crack width
- crack density or frequency
- crack shape, geometry and orientation
- degree of connectivity and origin

In the subsequent sections, some of these crack properties are discussed. However, first cracks need to be classified by their causes and origins. Fine internal microcracks always exist in the concrete matrix at a microscopic level, but are conventionally treated and investigated as part of the porous structure of concrete (Boulfiza et al. 2003). On the contrary, large macrocracks are associated with un-favourable environmental conditions and/or undesirable loading applications. Loading induced cracks mainly appear at the ITZ between the aggregate and the matrix and as the load increases, they extend inward toward the cement matrix (Nawy 2001). This study focuses on the macrocracks induced by loading.

2.4 Transport mechanisms in concrete

Furthermore, the induction of macrocracking is grouped into two separate groups, unloaded and loaded concrete specimens. Unloaded specimens typically behave differently from loaded specimens. This is due to the nature of incipient cracks in unloaded cracks that are often smaller in width and prone to influences such as self-healing. In contrast, the cracks of loaded RC members are typically opened up more (discussed in section 2.6). The advantage of unloaded concrete specimens is that they are easier to model, but the disadvantage is that they do not fully simulate real world conditions. Therefore, using these models for service life predictions of real world structures may become tricky (Wang et al. 2008). There are three different techniques for inducing macrocracks:

1. Artificial
 - (a) by saw cutting an artificial crack (Rodriguez et al. 2003)
 - (b) placing metal or plastic cast-in shims that are removed after curing to leave a crack (Arya et al. 1996)
2. Load-induced
 - (a) uniaxial compressive test (Samaha et al. 1992)
 - (b) ring-shaped test setups with an expansive core (Ismail et al. 2008)
 - (c) splitting test (Wang et al. 1997)
 - (d) flexural bending in 3- and 4-point loading (Paul 2015)
3. Combination
 - (a) Combination of artificially formed cracks (saw cuts or cast-in shims) and then further load-induced after curing (Otieno 2014)

This study will focus on technique three, described in chapter 3, where a combination of saw cuts with 3- and 4-point flexural macrocracks are induced to form known surface crack widths.

2.5 Factors affecting corrosion propagation

Once the required critical chloride concentration has been reached and the passive protection layer is broken down, active corrosion is initiated. Selected factors affecting the chloride-induced corrosion of steel are discussed in the following subsections. However, it is important to remember that the propagation of corrosion is dependent on, among others, concrete properties and the adequate supply of corrosion-sustaining substances (H_2O and O_2).

2.5.1 Effect of external exposure conditions

As mentioned previously, one of the main causes of deterioration in RC structures is chloride-induced corrosion, found in chloride laden environments. In South Africa, these environments are typically located in the coastal or marine region. In [EN-206 \(2000\)](#) provisions are made for the degree of exposure. The severity of chloride-induced environment is classified into groups for a more detailed design and requirements. These classes are shown in table [2.2](#).

Table 2.2: Chloride-induced corrosion environmental marine classes ([EN-206 \(2000\)](#))

EN-206 (2000) Class	Environment description
XS1	Exposed to airborne salt, but not in contact with seawater
XS2a	Permanently submerged
XS2b*	XS2a + exposed to abrasion
XS3a	Tidal, splash and spray zones
XS3b*	XS3a + exposed to abrasion

Note: * Sub-classes added to the South African coastal conditions

This study focuses on the tidal, splash and spray zones (Class XS3a) because most of the infrastructure situated within these regions have high social and economic consequences of failure. Furthermore, in terms of corrosion of reinforcing steel, it is considered to be one of the most aggressive marine environments (Melchers et al. [2012](#), Fig. 1). Along with the physical proximity to the splash zone, the external environment temperature and RH also play a vital role in the exposure conditions.

High temperatures increase the rate of corrosion of steel in the concrete because transport mechanisms occur more rapidly. However, at temperatures exceeding 40 °C

2.5 Factors affecting corrosion propagation

degrees, the rate of concrete drying and the decreasing oxygen solubility in the pore solution become the inhibiting factors for the corrosion rate (Živica 2003). The influence of temperature on the corrosion rate is estimated through an Arrhenius equation presented in equation 2.14 (Liu 1996).

$$i_{corr}(T_2) = i_0 \cdot \exp\left(\frac{E}{R} \cdot \left(\frac{1}{T_2} - \frac{1}{T_1}\right)\right) \quad (2.14)$$

where $i_{corr}(T_2)$ represents the expected corrosion rate at temperature T_2 , i_0 is the initial corrosion rate at a temperature T_1 , R is the universal gas constant and E is the activation energy. Caution should be used when applying this approach as the opposing effects and limitations of higher temperatures are not incorporated.

RH of the external environment is an important factor for both corrosion initiation and propagation because of the water needed at the cathode. As discussed in section 2.4, the concrete needs to be saturated enough for the pore solution to act as an electrolyte in the corrosion process, whilst at the same time dry enough to allow for the access of oxygen. The rate of oxygen movement towards the cathodic region is dependent on the depth of the reinforcement, the oxygen diffusion coefficient and the integrity of the concrete cover. The oxygen diffusion coefficient is affected by the moisture content and the w/b ratio of concrete as shown in figure 2.7.

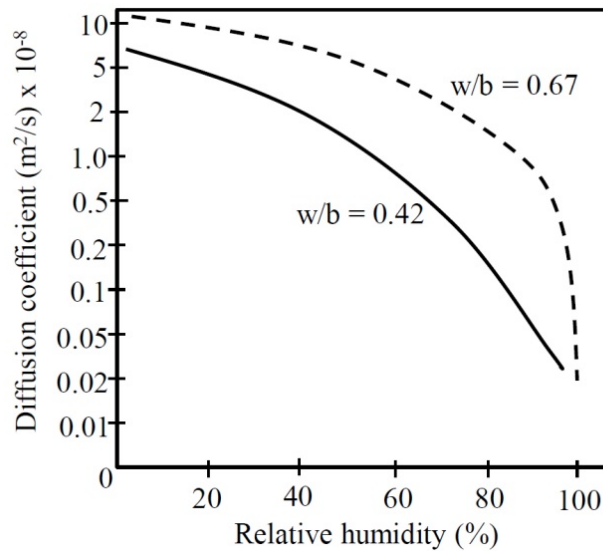


Figure 2.7: Influence of w/b ratio and RH on oxygen diffusion coefficient (Bentur et al. 1997)

2.5 Factors affecting corrosion propagation

A higher w/b ratio in the concrete results in a higher oxygen diffusion coefficient. This is an important aspect in the the mix design of coastal structures. In terms of RH, the most vigorous corrosion activity occurs above 80 % RH (Richardson 2003).

RC structures within the marine zone are constantly exposed to the aggressive environment of salt water from the ocean. To simulate these adverse exposure conditions, previous studies used three chloride-exposure acceleration techniques. The first (the immersion test) is a steady state exposure test used to examine the chloride ion ingress into the concrete specimens (Ismail et al. 2008; Win et al. 2004; Yoon et al. 2010). The concrete specimens are submerged into ponds of artificially created salt water for a certain period of time to simulate the exposure conditions of concrete structures in the marine zone. Afterwards they are taken out to dry and are then tested. Immersed specimens are shown in figure 2.8.

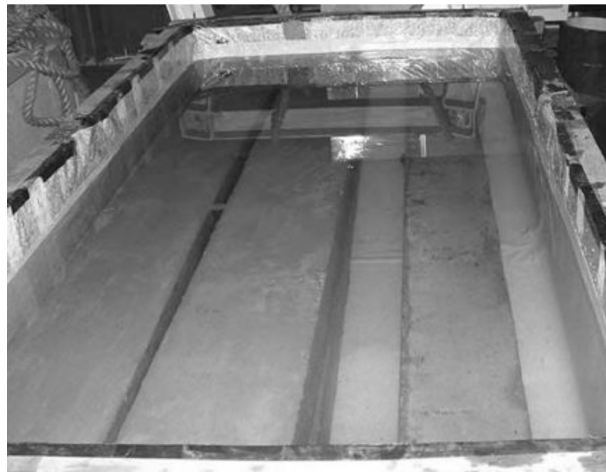


Figure 2.8: Submerged concrete specimens (Adiyastuti 2005)

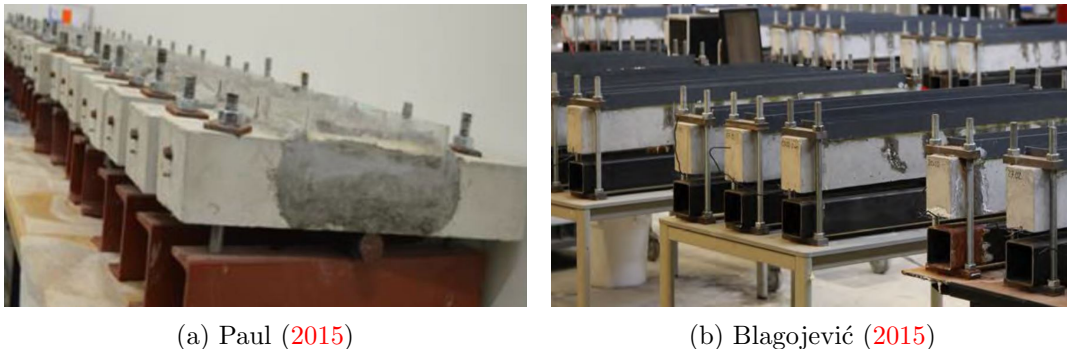
Submerged specimens only have one face exposed to the salt water to obtain the chloride profile after one dimensional ingress. This is done by sealing the other sides with epoxy to allow ingress of chloride ions from one side only (Adiyastuti 2005).

The rapid chloride migration test is the quickest method used to determine chloride penetration in concrete specimens due to the short time required for chloride profiling (Edvardsen et al. 2002). However, it is questioned as to whether or not the migration test is applicable to the chloride penetration mechanics of real world structures. The reliability of the data is also questioned because of the considerable amount of

2.5 Factors affecting corrosion propagation

limitations on the migration test (Blagojević 2015). This investigation does not use the rapid chloride migration test as a means of chloride profiling.

The cracked face ponding test setup is considered to be the best representation of simulating the alternating wetting and drying cycles of the marine environment. An example of this setup is shown in figure 2.9, where it can be observed that the cracked face is ponded with artificial salt solution.



(a) Paul (2015)

(b) Blagojević (2015)

Figure 2.9: Laboratory based ponding setup

The duration of the wetting and drying cycles is typically dependant on the type of concrete and the crack width. These two factors influence the rate of chloride penetration upon wetting and the supply of oxygen during the drying cycle. Three days wetting of a 3% NaCl solution, followed by four days of air drying was used in a recent study (Otieno 2014). Taking into consideration the important effect of temperature and RH of the surrounding environment, this study utilizes the alternating ponding cycles test for accelerated corrosion exposure conditions in laboratory specimens.

2.5.2 Effect of concrete quality (binder type and w/b ratio)

Concrete quality of RC structures within the marine environment is vital in ensuring durable performance of the structure. Firstly, the binder type influences concrete quality with the addition of extenders to ordinary Portland cement. The norm both locally and globally is to replace parts of OPC with extenders to create a more environmentally friendly cement. Supplementation of extenders reduces the amount of CO_2 emissions produced upon manufacturing, as well as lowering

2.5 Factors affecting corrosion propagation

manufacturing costs. The use of extenders offers the added benefit of improved durability performance (Beushausen et al. 2012; Alexander et al. 1999). W/b is the second factor that influences concrete quality in ensuring durability performance. These two factors of concrete quality is briefly discussed in the following subsections.

2.5.2.1 Binder type

Locally, the most used mineral additives are industrial by-products such as slagment (ground granulated Corex slagment (GGCS) and blastfurnace slagment (GGBS)) and fly ash (FA) (Beushausen et al. 2012). The addition of supplementary cementitious materials (SCM) improves the durability of the concrete by providing a denser cement matrix which is less penetrable by chloride ions. Figure 2.10 shows the comparison between the corrosion rate of steel in concrete containing only OPC versus cement containing extenders. C and w_c denote the cover and the crack width respectively.

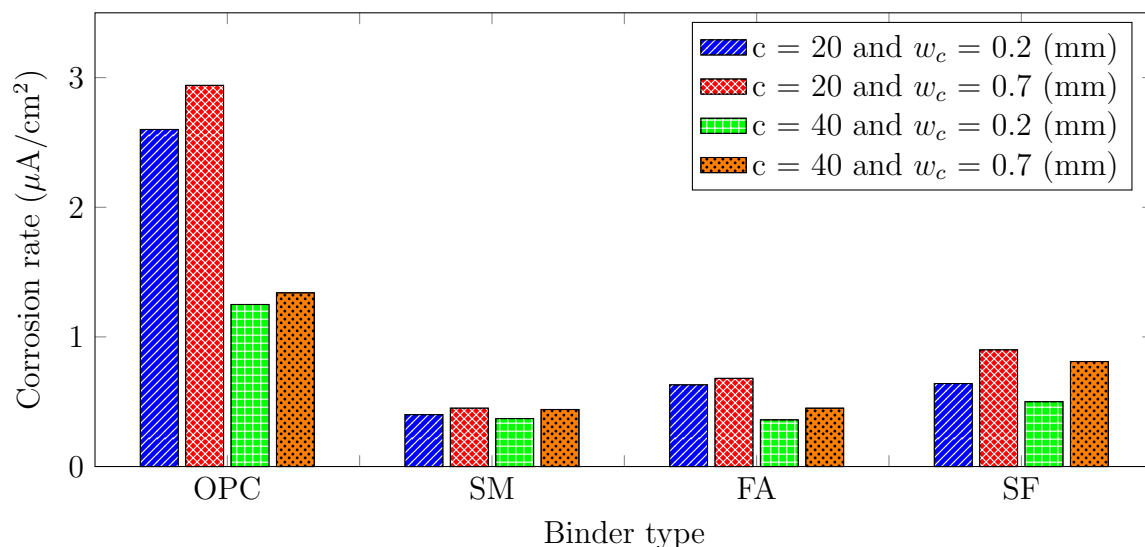


Figure 2.10: Corrosion rate in various cement compositions (reproduced from Scott et al. (2007))

The lower porosity is due to the capillary pores being filled with less OPC and rather being filled by the low-density calcium silicate hydrate (CSH) gel which ensures a denser microstructure (Arya et al. 1995). In addition, a study by Dhir et al. (1997) shows that the addition of fly ash has a chloride-binding effect which leads to better physical absorption of the chlorides by the cement paste, thus reducing

2.5 Factors affecting corrosion propagation

chloride-induced corrosion.

2.5.2.2 Water-to-binder ratio (w/b)

The w/b ratio is typically limited to a maximum value of 0.45 w/b to ensure durability (Owens 2009, Chap.9). The w/b ratio affects the pore structure of the concrete. A high w/b ratio leads to reduced concrete resistivity and increased penetrability (Petterson 1992). In a study by Mangat et al. (1994) presented in table 2.3, the significant effect of the w/b ratio on the corrosion rate, denoted as i_{corr} , of reinforcement is clear. This example was performed with 100 x 100 x 370 mm concrete specimens containing 12 mm diameter deformed reinforcement rods and subjected to 600 days in a salt water spray chamber (1200 wetting and drying cycles). The reinforcement was placed with a 10 mm cover.

Table 2.3: Corrosion rates of different w/b ratios (Mangat et al. 1994)

w/b Ratio	Binder (kg/m ³)	Acid soluble Cl^- *	i_{corr} ($\mu A/cm^2$)
0.45	430	1.4	0.13
0.58	430	2.0	0.65
0.76	430	2.3	2.16

Note: * at steel level (% by mass of binder)

It is therefore observed that a higher w/b ratio leads to a higher corrosion rate. The w/b ratio must be carefully considered at the mix design stage for structures exposed to aggressive environments as it has a substantial influence on the durability performance of the structure.

2.5.3 Concrete cover

The concrete cover influences not only the corrosion initiation, but also the corrosion rate in the corrosion propagation stage. Firstly, in the corrosion initiation stage, the concrete cover provides the initial barrier against the chloride ions. The thickness and quality of the concrete cover has a significant effect on the build-up towards the corrosion propagation stage. In the presence of cracks, the durability performance of the cover is negatively affected, as discussed in section 2.5.4. In the event that the cover thickness is reduced (for example an accidental impact), the

2.5 Factors affecting corrosion propagation

service life may also be significantly reduced as the concrete penetrability is increased.

Secondly, the concrete cover plays a vital role in the corrosion propagation phase. For example, an increase in cover thickness increases the travel path for the corrosion constituents to reach the reinforcement level (O_2 , H_2O and Cl^-). This is illustrated graphically in figure 2.11 where the effect on the O_2 diffusion rate for a variation in concrete cover thickness is shown.

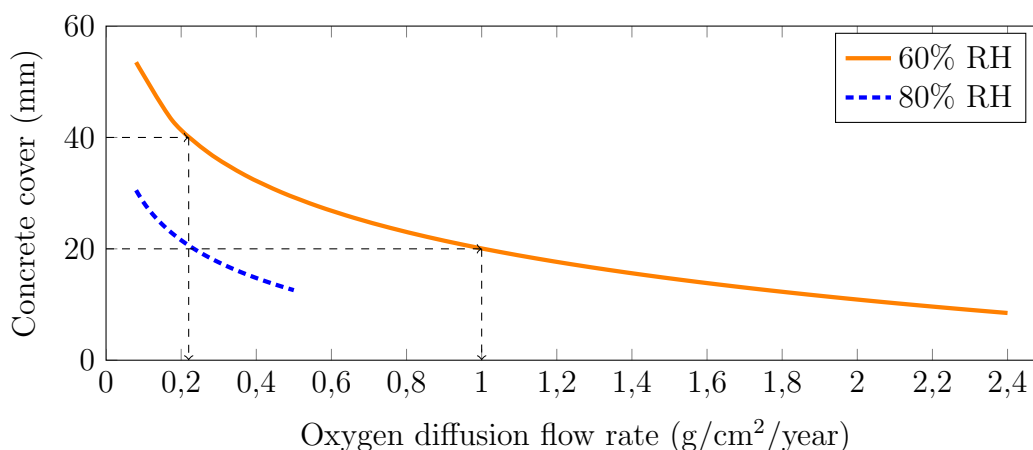


Figure 2.11: Concrete cover vs. O_2 diffusion (reproduced from Bentur et al. (1997))

It is evident in figure 2.11 that doubling the concrete cover (from 20 to 40 mm) results in approximately a quarter of the oxygen diffusion rate (from 1.0 to 0.24 g/cm²/year) for an environment of 60 % RH. An increase in RH also decreases the oxygen diffusion flow rate. The cover depth also influences the drying time as a thicker cover would retain moisture for a longer period. Therefore, concrete cover depth affects the durability performance and corrosion rate by either increasing or decreasing the travel distance of the corrosion agents (Cl^- , O_2 , H_2O).

SANS 10100-2 and **EN-1992-1 (2004)** both specify a minimum concrete cover of 40 mm for normal density concrete exposed to tidal marine conditions. Therefore, this study maintains the required cover depth of 40 mm in order to more accurately depict the influences of other experimental variables.

2.5 Factors affecting corrosion propagation

2.5.4 Effect of crack characteristics

Cracks within a concrete structure cause the concrete to become more permeable by facilitating access for Cl^- , O_2 and H_2O from the outside environment, therefore, compromises the durability performance of the structure. Chloride-induced corrosion in cracked concrete structures depends on multiple factors such as crack orientation and geometry, crack width, crack density/frequency, and the ability of cracks to self-heal. These factors are briefly discussed in the following subsections. The various causes of cracks in RC is illustrated in figure 2.12.

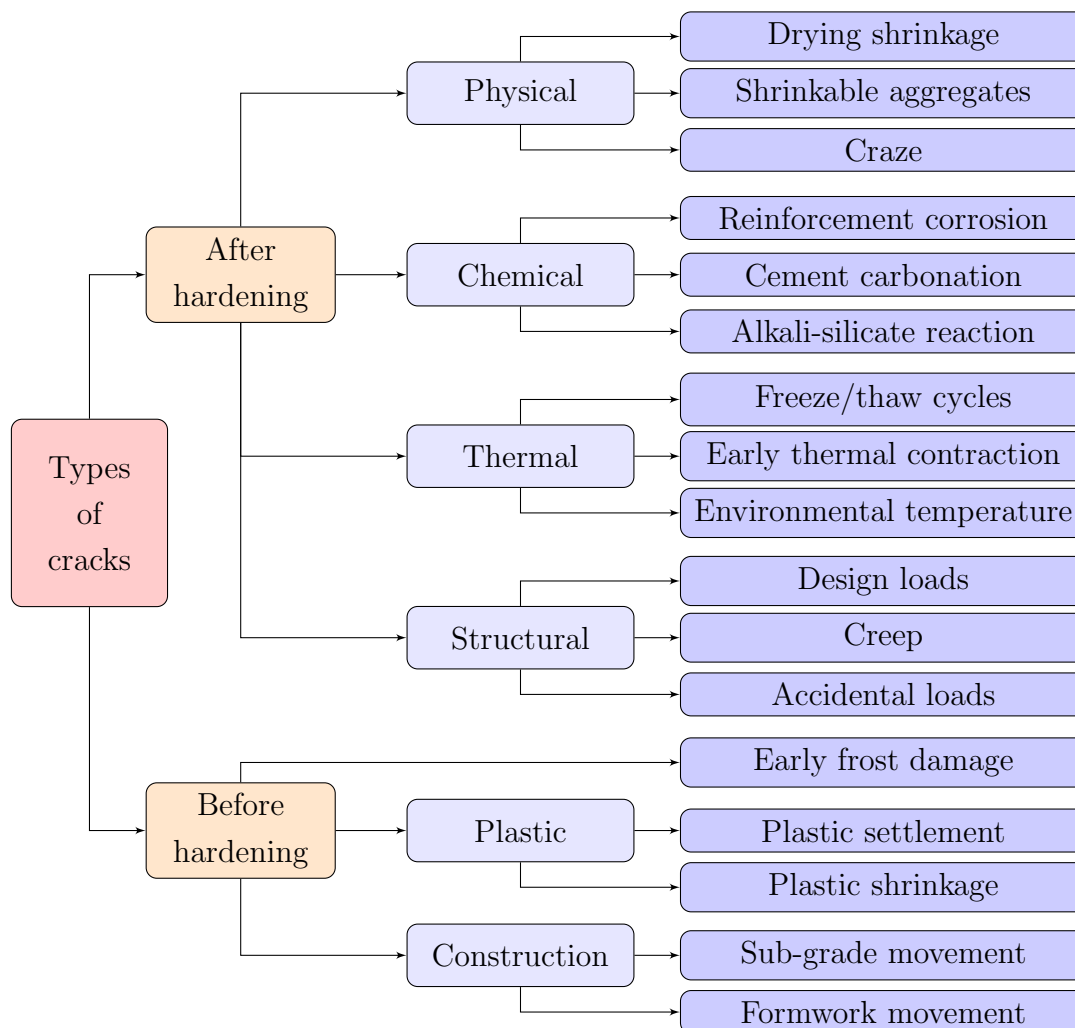


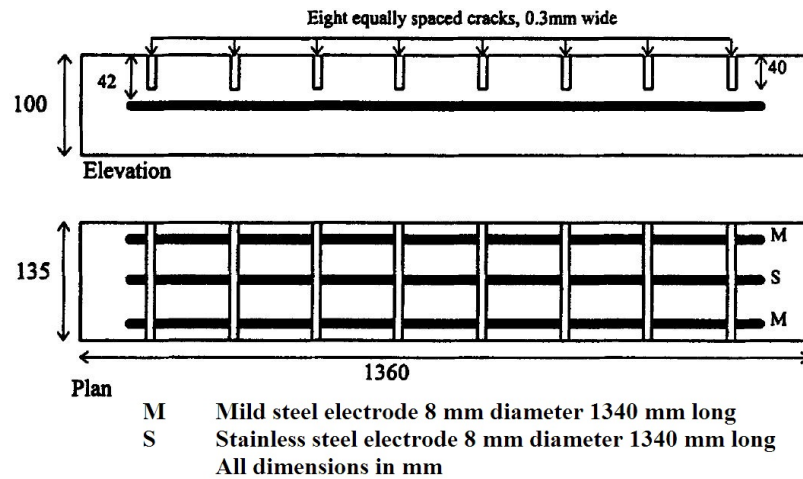
Figure 2.12: Causes of cracking in RC structures (adapted from CEB (1992))

2.5 Factors affecting corrosion propagation

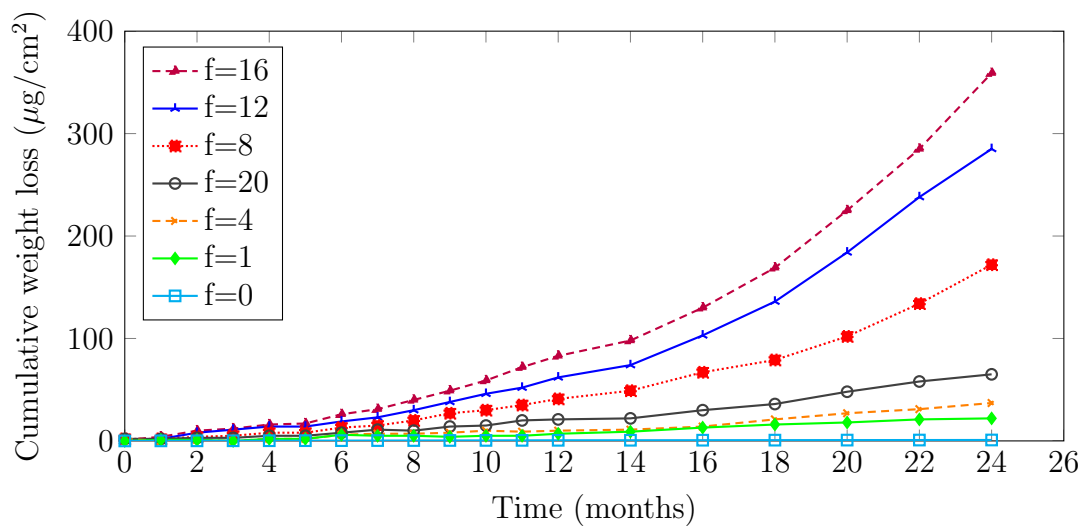
2.5.4.1 Crack density/frequency

The number of cracks transverse to the reinforcement per unit length is referred to as crack frequency (or density). In a previous study by Arya et al. (1996), it was shown that an increase in the number of cracks results in an increase in corrosion rate shown in figure 2.13. This increase in corrosion rate is due to the ease at which corrosion constituents ingress into the concrete as the concrete is more penetrable. The study was performed using seven different crack frequency configurations. The total crack opening of the artificially created cast-in plastic shims was 2.4 mm for each of the seven crack frequencies. The crack depth, cover and w/b were kept constant at 40 mm, 42 mm and 0.65 respectively. Figure 2.13a shows the experimental setup that was implemented. The investigated crack spacings (S_c) were 680, 272, 150, 105, 80 and 65 mm. Furthermore, a stainless steel rod (relatively corrosion resistant) was embedded in the center of the beams to act as a counter electrode in the event of taking corrosion rate readings.

2.5 Factors affecting corrosion propagation



(a) Setup



(b) Results

Figure 2.13: Effect of crack frequency on the cumulative mass loss due to corrosion (reproduced from Arya et al. (1996))

The results of the mass loss for various crack frequencies are shown in figure 2.13b. The mass loss increases in conjunction with a closer crack spacing as expected. However, an irregular result is seen for the case of $f = 20$ ($S_c = 65$ mm). This instance is expected to have suffered the highest mass loss, but it is approximately 7 times lower than the highest $f = 16$ case ($S_c = 80$ mm).

This low corrosion rate result is possibly due to the autogenous healing of cracks over time, especially for this study where cracks were induced through removable shims

2.5 Factors affecting corrosion propagation

and are therefore referred to as “dormant”. The self-healing potential of cracks is described in more detail in section 2.5.4.5. It has to be noted that typical cracks are V-shaped in flexure, rather than rectangular throughout their length. Higher numbers of cracks are also associated with an increase in loading conditions and generally result in an increase in crack widths (Arya et al. 1996).

A recent study by Blagojević (2015, pg. 38) suggests that the results obtained in figure 2.13 would have been significantly different under similar conditions of structures in practice. This is due to the fact that RC structures are typically cracked because of adverse loading conditions, and often subjected to constant variability. An investigation of the interrelated effects of crack spacing and width would be beneficial to understanding how crack density affects corrosion propagation.

2.5.4.2 Crack width

The allowable surface crack width for RC structures exposed to chloride-induced corrosion is given in table 2.4. Several authors have considered crack width to be the most important parameter for the ingress of chloride ions. Many authors have in recent years investigated the influence of crack width on the corrosion rate of reinforcement, with the findings generally concluding that the presence of cracks accelerates corrosion initiation (Arya et al. 1996; Otieno et al. 2010; Arya et al. 1996; Jaffer et al. 2009; Paul 2015; Schießl et al. 1997; François et al. 2006; Şahmaran et al. 2008; Pacheco Farias 2015; Blagojević 2015). Whether the crack width affects both the corrosion initiation and propagation or only corrosion propagation is still up for debate. However, both are generally dependent on the concrete cover, type of binder and w/b ratio as shown in a study by Pettersson et al. (1996). The study concluded that for crack widths smaller than 0.4 mm, the corrosion rate was affected when the cover changed from 15 to 30 mm. However, a change in cover had insignificant influences on the corrosion rates for crack widths larger than 0.4 mm.

2.5 Factors affecting corrosion propagation

Table 2.4: Allowed crack width for RC structures exposed to chloride-induced corrosion

Design code (Regulation)	Allowable crack width (mm)
ACI 224 (1994)	0.15
NEN 6720 (1995)	0.2
Eurocode 2 (2004)	0.3
SANS 10100-1 (2000)	0.3
BS 8110 (1997)	0.3
FIB/Model Code 2010	0.3

In another study by Otieno et al. (2010), it was found that the surface crack width does have a significant impact on the corrosion rate as illustrated in figure 2.14. In this investigation, for the same w/b ratio and cement composition, the average corrosion rate after week 26-31 shows that an increase in crack width leads to an increase in corrosion rate. It is important to note that the uncracked specimens have not yet attained active corrosion rates of higher than $0.1 \mu\text{A}/\text{cm}^2$. To stop the process of self-healing (discussed in section 2.5.4.5) in their study, the concrete specimens were reloaded twice within the 31-week period.

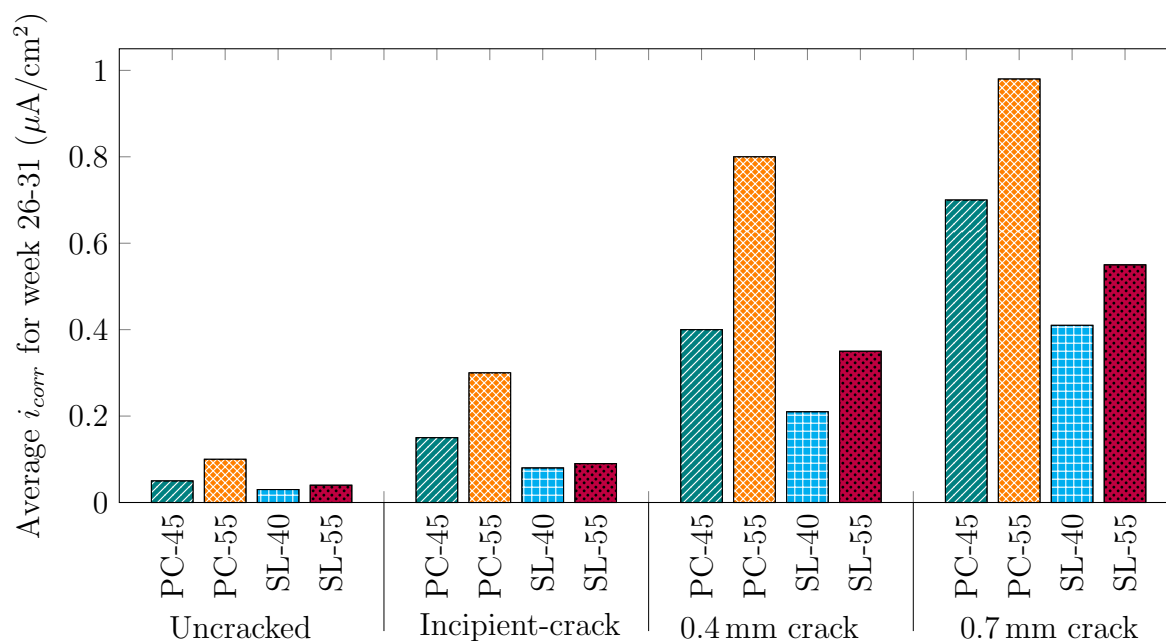


Figure 2.14: Effect of crack width and concrete composition on corrosion rates (reproduced from (Otieno et al. 2010))

2.5 Factors affecting corrosion propagation

In summary, cracks influence the initiation and propagation stages of corrosion. Depending on surface crack width and concrete quality, the initiation stage can be remarkably shortened or in some cases even be eliminated in the presence of cracks. The effect of concrete cracking in the propagation stage is still substantial, but its magnitude is related to the interaction between the surface crack width and concrete quality.

2.5.4.3 Cracking at the steel-concrete interface

The fracture properties of concrete are related to the concrete-reinforcement interface around the deformed reinforcement rod. As reinforcement rods typically carry tension within a concrete member, adverse loading conditions spawn flexural cracks due to the low tension capacity of the concrete. With an increase in loading repetitions or steel stress levels, small internal (“secondary”) cracks form as a result of the force components on the deformed bar’s ribs as shown in figure 2.15. It is also worth noting that at this point of cracking, full crack closure after the load has been removed will not occur (Goto 1971).

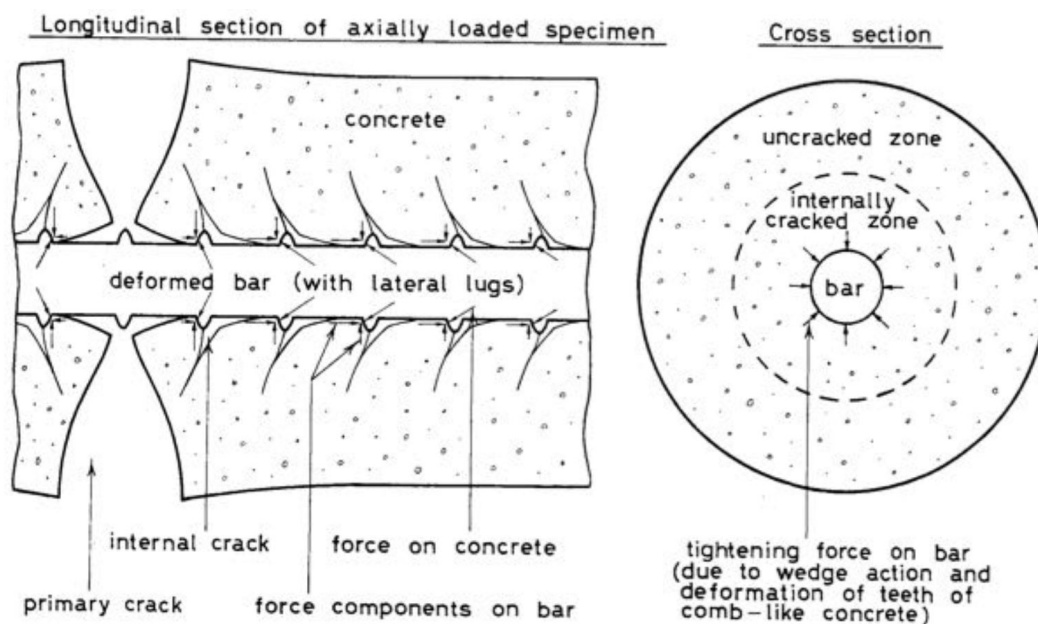


Figure 2.15: Schematic of primary and secondary (internal) cracks (Goto 1971)

With regard to crack development in flexure, Pease (2010) has shown (figure 2.16) that an increased load results in a denser crack pattern at the concrete-steel interface. For

2.5 Factors affecting corrosion propagation

figure 2.16a, a 8 mm aggregate size was employed, 2.16b had a maximum aggregate size of 16 mm, 2.16c was cracked under a single load and 2.16d was loaded under increasing cyclic loading.

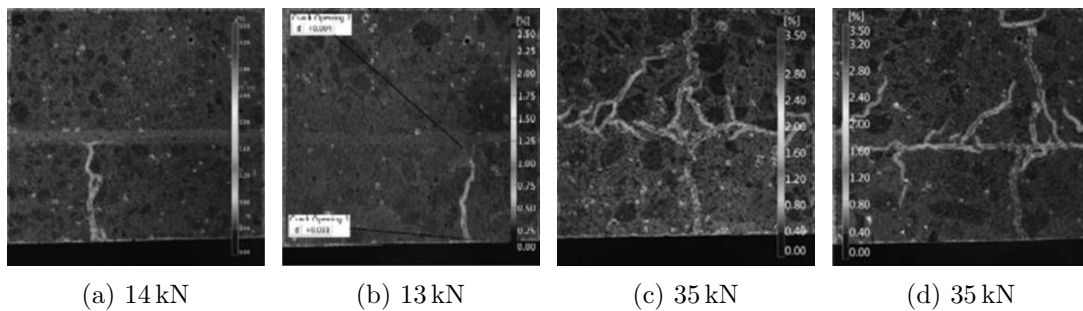


Figure 2.16: Computed strain overlay on specimens with different loading conditions (Pease 2010)

A higher loading on the specimens resulted in an increase in separation and consequently concrete-steel slip. Therefore, the steel-stress level plays an important role in the formation of internal microcracks at reinforcement level and should not be neglected in the relation to chloride-induced corrosion. The effects of the steel-stress level on the corrosion rate should be investigated in future studies as a higher steel stress may potentially lead to a higher corrosion rate due to the possible increase in penetrability of the concrete.

2.5.4.4 Crack geometry and orientation

The occurrence of both transverse and longitudinal cracks is often associated with the restrained deformations in concrete. Recall the causes of cracks shown in figure 2.12. Transverse cracks are more likely to occur in areas of flexure (high tension-stressed areas) with the cathode areas of the corrosion process typically forming in the uncracked regions. Perhaps the most detrimental type of crack orientation is longitudinal as large areas of steel are easily accessed by Cl^- , H_2O and O_2 . Longitudinal cracks form as a result of plastic settlement or shrinkage, but are mostly known in older structures due to the expansive products of corrosion.

Limited research points to the fact that an increase in surface crack width results in a larger area of affected reinforcement. Limiting the surface crack width would

2.5 Factors affecting corrosion propagation

typically not result in the same reinforcement level crack width. For example, between different specimens with a 20 vs. 40 mm cover the crack width at reinforcement level would not be equivalent to each other. This is because flexural cracks generally form in a V-shape. Therefore, the crack width at reinforcement level should be a function of concrete cover and surface crack width rather than only allowing for a limit on the surface crack width.

2.5.4.5 Autogenous Crack Healing

Autogenous crack healing is the ability of concrete to proceed with the continuous hydration process in the presence of water. This healing property of concrete significantly reduces the penetrability of the concrete and improves the durability performance. The precipitation of calcium carbonate crystals inside the cracks is likely the largest influence on the autogenous healing capacity of concrete. To quantify the extent of self-healing potential in fresh water and sea water, Palin et al. (2015) set out to visually quantify the autogenous healing capacity of OPC and blast-furnace slag cement (BFS). It was found that sea water better accommodates for autogenous healing of OPC. After 56 days, 100% healing of cracks up to $592\ \mu\text{m}$ were achieved in sea water, in comparison to fresh water, only managing 100% healing for cracks widths of $168\ \mu\text{m}$. Figures 2.17 and 2.18 show the crack widths in OPC at three different time frames for fresh water and sea water respectively, each separated by 2 weeks from (a) to (c).

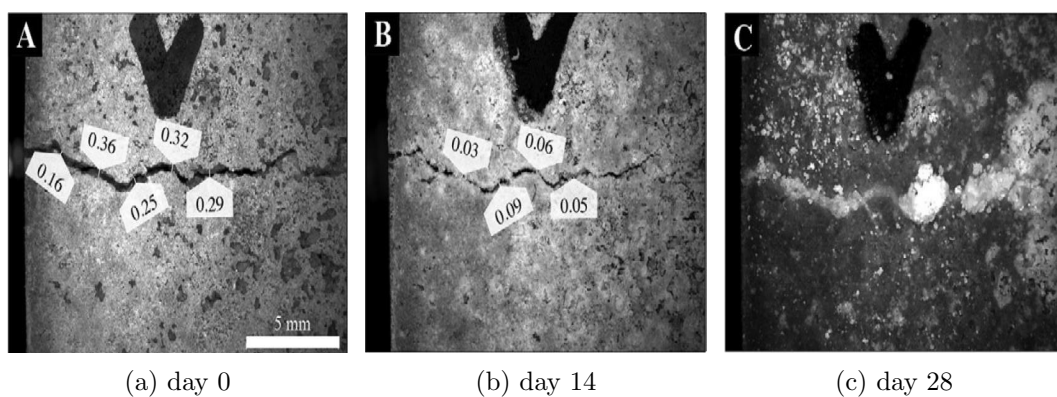


Figure 2.17: Stereoscopic images of concrete in fresh water (Palin et al. 2015)

2.5 Factors affecting corrosion propagation

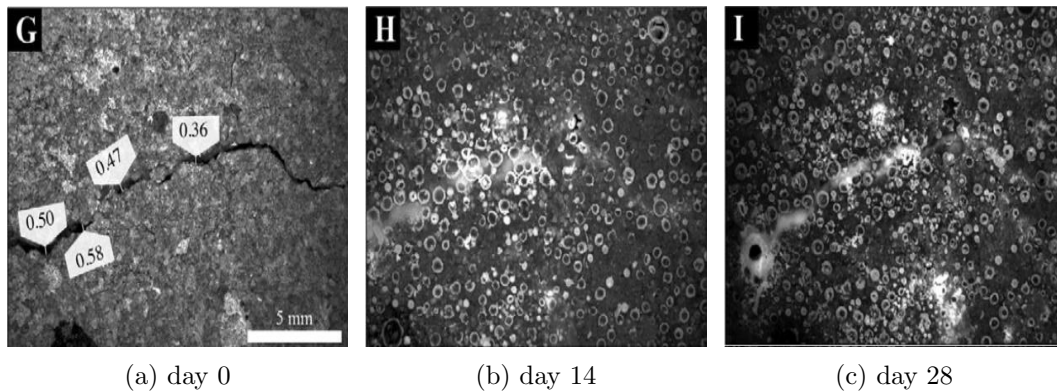


Figure 2.18: Stereoscopic images of concrete in sea water (Palin et al. 2015)

The autogenous healing ability of OPC specimens submerged in sea and fresh water shows that the healing potential may be attributed to the presence of specific ions in the water. This is indeed the case as sea water contains carbonate, calcium and magnesium ions that may precipitate as minerals (Palin et al. 2015). In fresh water, however, there exist limited carbonate ions and negligible calcium and magnesium ions and resulted in a healed crack width approximately 5 times less than that of sea water. There are other important crack characteristics that affect the self-healing ability such as crack depth and length which are not covered in this review.

2.5.5 Pitting factor

In cracked concrete, the assumption that corrosion is uniform can be misleading as corrosion does not necessarily occur over the length of the bar for example in the case of carbonation induced corrosion. Even though surface morphology of corroding reinforcement rods are not the scope of this study, it is important to distinguish between general corrosion and pitting corrosion. Figure 2.19 shows an example of the difference between general (uniformly around the circumference of the rod) and pitting corrosion (localised corrosion).

2.5 Factors affecting corrosion propagation

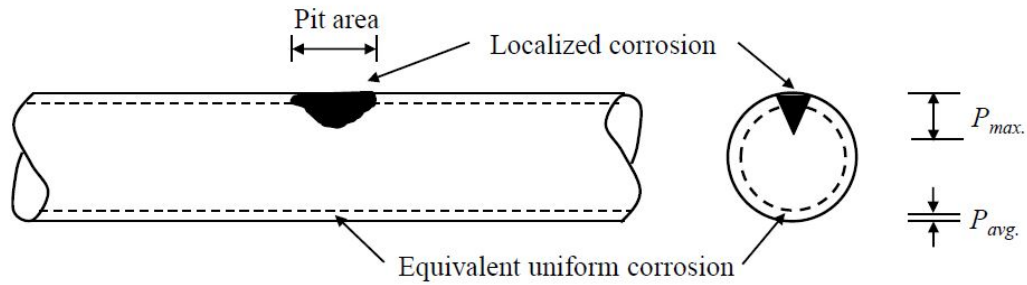
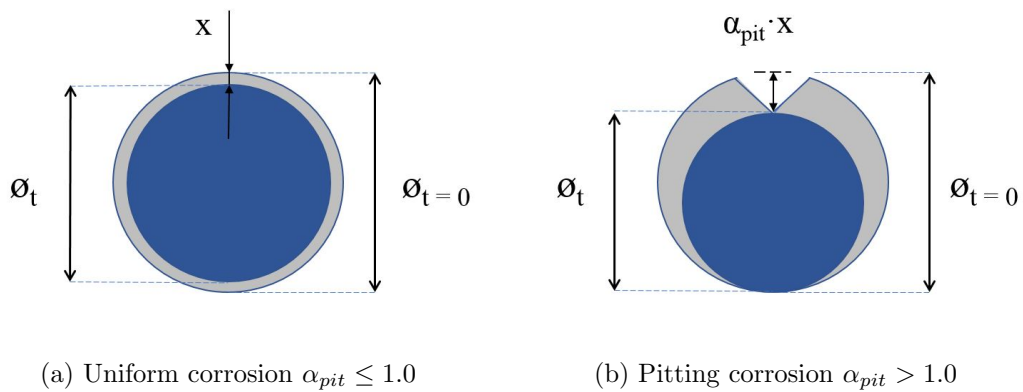


Figure 2.19: Schematic of general vs. pitting corrosion (Andrade et al. 2017)

It can be seen in figure 2.19 that pitting corrosion would result in a greater loss of resistance due to the smaller residual cross-sectional area of the reinforcement rod. This is illustrated in more detail in figure 2.20.



(a) Uniform corrosion $\alpha_{pit} \leq 1.0$

(b) Pitting corrosion $\alpha_{pit} > 1.0$

Figure 2.20: Schematic geometry of corroding steel bar (adapted from Andrade et al. (2001, pg. 145))

The resulting localised corrosion (pitting) is accounted for by incorporating a pit concentration factor, α_{pit} , which is multiplied by the average depth of attack of uniform corrosion, $P_{uniform}$ as shown in equation 2.15. P_{max} represents the maximum penetration depth of the localized corrosion. The equation for uniform depth of attack is described in more detail in section 2.6.1.

$$P_{max} = \alpha_{pit} \cdot P_{uniform} \quad (2.15)$$

The pitting factor is determined by carrying out a morphology assessment on the reinforcement rod at termination of the experiment. The pitting factors from previous experimental studies are shown in table 2.5.

2.5 Factors affecting corrosion propagation

Table 2.5: Typical suggested pitting factors for corroding RC

Reference	Concrete state, exposure type	α_{pit} factor
Carbonation induced	un-cracked, natural	1
Tuutti (1982)	un-cracked, impressed current	4 - 10
Gonzalez et al. (1995)	un-cracked, natural	4 - 8
Gonzalez et al. (1995)	un-cracked, accelerated	5 - 13
Neff et al. (2011)	un-cracked, accelerated	18
Otieno (2014)	cracked, natural & accelerated	10

More studies on uncracked and cracked concrete are still needed on the topic of pitting corrosion in chloride-induced corrosion in RC, as there is still no clear guideline to the use of pitting factors. Andrade et al. (1997) recommends using a conservative pitting factor in the range of 4 - 10. The upper limit being more applicable to cracked, accelerated concrete members. On account of this recommendation, this study makes use of a conservative pitting factor of $\alpha_{pit} = 5$ due to the lack of adequate instruments and apparatus required to perform a surface morphological study on the corroded reinforcement bars.

2.5.6 Effect of multiple reinforcement bars

In the past, the majority of RC corrosion investigations involved the experimentation of a single reinforcement rod exposed to chloride-induced testing. However, concrete structures in practice typically have many layers of interwoven reinforcement rods and/or mats positioned within them. Consequently, in the case of cracked RC, the orientation of the crack sometimes extends to expose more than one reinforcement rod to external corrosive elements (Cl^- , H_2O , O_2). For example, in a beam with a transverse flexural crack across the midspan with multiple reinforcement rods at the bottom, all the bars become exposed to the external environment, given that the crack extends deeper than the reinforcement level. Also, multiple reinforcement rods can be (in most cases) electrically interconnected when there is shear reinforcement and/or for reinforcement mats spot welded together (e.g. beams, slabs etc.).

In a study by Schießl et al. (1997), it was shown that in cracked RC two corrosion mechanisms can arise. Both mechanisms, macrocell and microcell corrosion, occur in the cracked zone or nearby area as shown in figure 2.21.

2.5 Factors affecting corrosion propagation

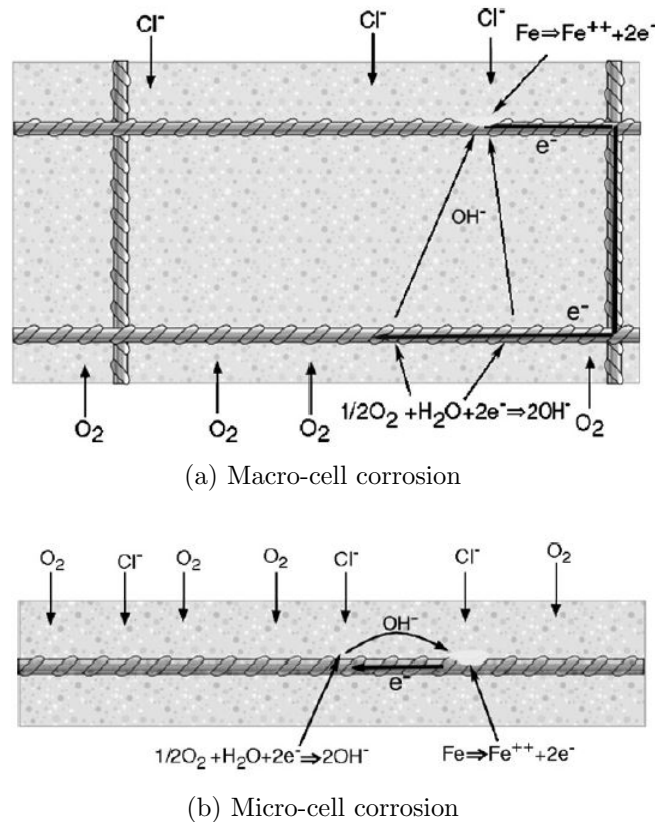


Figure 2.21: Macro-cell vs. micro-cell corrosion (Hansson et al. 2006)

The first mechanism, macrocell corrosion occurs because the reinforcing in the cracked zone acts as an anode while the passive steel between the cracks acts as the cathode. Microcell corrosion, on the other hand, is characterised by both the anodic and cathodic processes occurring adjacent to each other allowing oxygen from outside to penetrate the site. For example, both the anode and cathode are situated inside the crack region (Hansson et al. 2006). However, it is assumed that for multiple reinforcement rods placed next to each other, a similar process would take place, where the electrons flow towards the more actively corroding bar from the less actively corroding bar.

In another study by Cao et al. (2016, pg. 303), the term macrocell corrosion is given to the situation where the current (e^-) flows between the actively corroding steel bar and the steel bar experiencing a lower corrosion rate, or still in the passive state (see figure 2.21a). The integrity and continuity of the steel bar generally makes it difficult to measure the macrocell corrosion effect.

2.5 Factors affecting corrosion propagation

The Stern-Geary corrosion current density equation $i_{corr-SG}$ (equation 2.19) has been widely used to quantitatively assess the corrosion rate of the steel reinforcing. However, Cao et al. (2016) suggests that the $i_{corr-SG}$ is only applicable to the microcell current density. This suggestion implies that the current density is confined to the area of the bar under the counter electrode of the sensor, generally, only including the corrosion rates of that specific bar. Therefore, it was proposed that the corrosion rate should include the influence of other bars that are not directly underneath the sensor at the time of taking a corrosion rate reading. Cao et al. (2016) refers to this combined influence of all the bars as the macrocell current density $i_{corr-macro}$. This investigation also hypothesised that the other bars not directly underneath the sensor can aid the more actively corroding bars with OH^- as shown in figure 2.21a.

A complex arrangement of reinforcement layers may lead to a intricate distribution and interaction of anodic and cathodic sites (Otieno 2014, pg. 211). In a study done by Paul (2015), it is postulated that the reduced anode-to-cathode ratio associated with the increase in the amount of reinforcement density may lead to a reduced corrosion rate. This is due to a smaller area being available for the formation of corrosion products. With this modification to the anode-to-cathode ratios, the tensile steel is potentially at a higher risk of corrosion if the anodic sites are located in the tensile region. The same could also be true if the anodic sites are located on the stirrups. This scenario of multiple reinforcement rods is investigated in this study and is described in more detail in chapter 3.

2.5.7 Influence of loading conditions

Cracks in structures are caused by a variety of aspects as shown in figure 2.12. As mentioned, unfavoured loading conditions may result in the spawning of cracks and consequently aid in the deterioration rate of the structure. In a study by Yoon et al. (2000), the influence of sustained loading versus pre-cracking (pre-loading) was studied on 100 x 150 x 1170 mm specimens. The specimens had a concrete cover of 30 mm and a w/b ratio of 0.5. They were tested for 450 hours with the aid of induced current and a wetting-drying cycle of 4 and 3 days respectively with 3% NaCl solution. The specimens under the sustained loading were loaded to 20, 45, 60

2.5 Factors affecting corrosion propagation

and 75% of their ultimate flexural load, while the pre-loaded specimens were loaded to 45 and 75% of their ultimate flexure load. The results are shown in figure 2.22

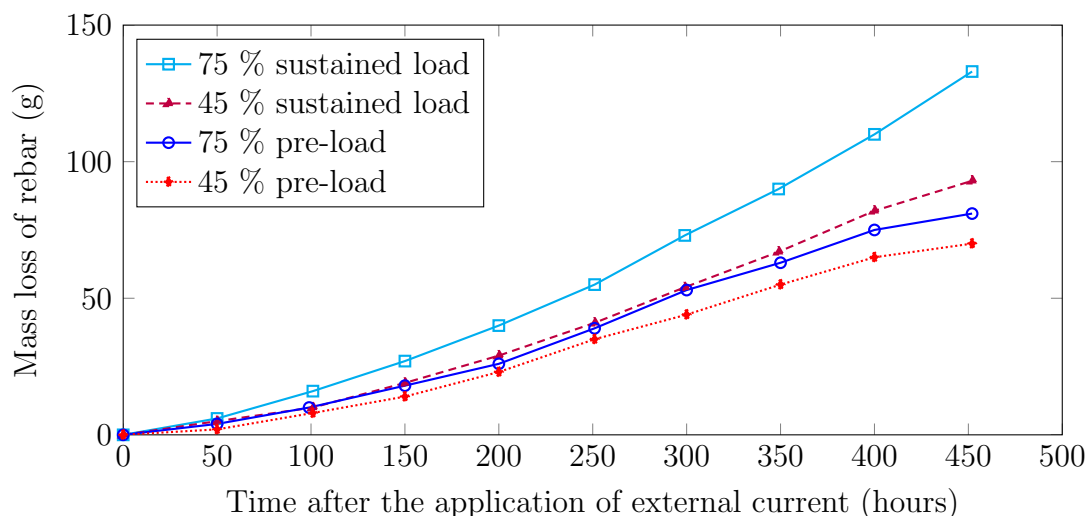


Figure 2.22: Sustained loading versus pre-loading (reproduced from Yoon et al. (2000))

The observed higher corrosion rate of specimens under a sustained load shown in figure 2.22 is as result of the closure of cracks upon un-loading of the pre-loaded specimens. The un-loading slows the penetration of the corrosion agents and reduces the connectivity between the cracks at the concrete-steel interface. Although not a parameter of the Yoon et al. (2000) study, the effects of self-healing may also contribute to the explanation of lower corrosion rates for pre-loaded when compared to that of the sustained loaded specimens.

It is clear that crack activity is an important consideration for the corrosion rate and should be taken into account when conducting on-site corrosion assessments. In a recent study by Blagojević (2015), it is shown that an increase in steel-stress levels may lead to an increase in cracking and a decrease in concrete self-healing. Although this effect on the corrosion propagation is not directly investigated in this study, section 5.2 shows that there is a relationship between the steel-stress level, associated with crack activity, and the corrosion rate.

2.6 Corrosion assessment and monitoring

The assessment of concrete structures affected by corrosion is generally done by means of a preliminary and detailed assessment. These assessments are used to determine the degree of corrosion. The preliminary assessment is used to quantify the extent of corrosion, the possible cause(s) thereof, and the extent of damage that has been caused. Detailed assessments include techniques such as testing for chloride content through the drilling of cores and measuring reinforcement corrosion rates. The definition of corrosion rate is discussed, followed by typical corrosion rate assessment and monitoring techniques.

2.6.1 Definition of corrosion rate

Corrosion rate is defined as the amount of corrosion produced by a unit surface area over a specific time period (Andrade et al. 1996). The physical approach to measuring the corrosion rate is to measure the weight difference between the initial weight of the reinforcement and the weight after exposure to a corrosive environment. This is referred to as the gravimetric method. The mass loss of reinforcement can be determined non-destructively by measuring the chemical dissolution of the reinforcement by means of electrochemical techniques. Electrochemical techniques are the most widely used method for measuring metallic loss of reinforcement. When using electrochemical techniques, Faraday's law is used to convert the electrochemical parameters into gravimetric parameters as shown in equations 2.16 and 2.17 (Andrade et al. 1996).

$$\frac{I \cdot t}{F} = \frac{\Delta W \cdot Z}{M} \quad (2.16)$$

$$\Delta W = \frac{M \cdot I \cdot t}{Z \cdot F} \quad (2.17)$$

where I is the electrical current in Ampere (A), t is the time (s), Z is the valency of metal ($Z_{iron} = +2$), ΔW is the weight loss due to corrosion (g), F is Faraday's constant (96 500 C) and M is the molecular weight of metal ($M_{iron} = 55.845$ g/mol).

The electric current, I , is referred to as the corrosion intensity, I_{corr} , and is given in $\mu\text{A}/\text{cm}^2$ when it is assumed that the attack is homogeneous over the corrosion exposed metallic surface. The metal density is then used to convert to $\mu\text{m}/\text{year}$ for assumed uniform corrosion. A unit conversion table is presented in table 5.1. It is important

2.6 Corrosion assessment and monitoring

to note that corrosion intensity refers to the specific instance the measurement was taken. Therefore, corrosion intensity and corrosion rate are fundamentally different, but are instinctively used similar to each other for practical purposes (Andrade et al. 1996). As shown in figure 2.23, the corrosion rate is the equivalent weight loss of the metal (g) by the unit of surface (cm^2) during a certain period of time.

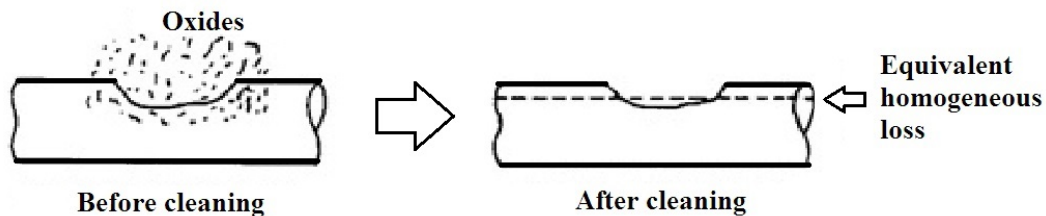


Figure 2.23: Schematic of equivalent homogeneous loss in g/cm^2 (reproduced from Andrade et al. (1996))

Consequently, if various instances of corrosion intensities are measured over the course of a specific period, the amount of weight lost by a reinforcement bar must be equal to the integral of the total current of the $I_{corr} - \text{time}$ curve for that period. It is recommended that the true metallic gravimetric loss of the exposed bar is compared to the electrochemical measured corrosion intensity in order to ensure accurate and reliable I_{corr} readings. This is discussed in more detail in section 3.9.1.

In the case of localised attack, an error in I_{corr} values can arise if the sample size is too large relative to the corroding area, as shown in figure 2.24. The first recommendation from previous research is to minimize this error by studying smaller specimens. Another suggestion is to dismantle and inspect the actual corroding area after the experiment and accounting only for the area visually identified to be suffering from corrosion (Andrade et al. 1996). By utilising recent advances in electrochemical techniques as shown in sections 2.6.2.1 to 2.6.2.3, this error can be minimised or even avoided, especially with the use of a modulated confinement technique as discussed in section 2.6.2.6.

2.6 Corrosion assessment and monitoring

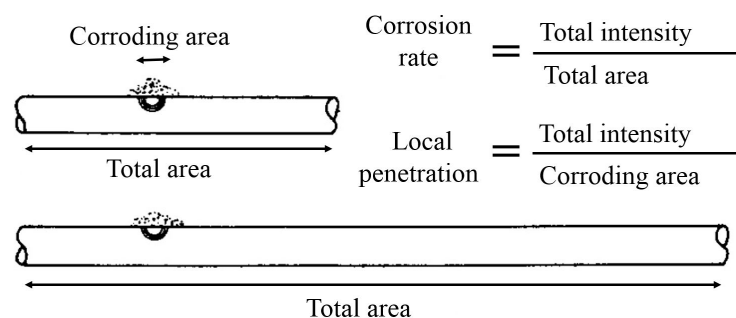


Figure 2.24: Schematic of localized attack and length error (reproduced from Andrade et al. (1996))

Table 2.6 shows a proposed corrosion intensity classification of corrosion rates (Andrade et al. 1996). A more detailed explanation on how the corrosion rate is interconnected with structural service life and why corrosion rates are categorised in negligible to high ranges is provided in section 5.4.2.

Table 2.6: Corrosion intensity classification (Andrade et al. 1996)

Corrosion intensity $\mu A/cm^2$	Corrosion level	Typical concrete status
≤ 0.1	Negligible	Dry concrete, without chlorides
0.1-0.5	Low	Slightly humid and/or containing chlorides
0.5-1.0	Moderate	High humidity and/or containing chlorides
≥ 1.0	High	Highly chloride contaminated concrete

2.6.2 Corrosion measurement techniques

The prediction of the residual service life of a structure is difficult, made complicated by the challenges associated with accurately determining the corrosion rate of the reinforcement. Corrosion rates is required to plan the repair and rehabilitation procedures. There are various corrosion rate measurement techniques available, some of which are discussed in the following subsections.

2.6 Corrosion assessment and monitoring

2.6.2.1 Polarization resistance technique

The linear polarization resistance (LPR) technique is based on the application of a small range of potential (± 20 mV) about the corrosion potential (E_{corr}), which is then related to the corrosion rate (I_{corr}). This is measured in one of the following ways (Poursaei 2010):

- (i) Potentiodynamic - potential sweep is applied to observe the response in current.
- (ii) Potentiostatic - constant potential pulse is applied to observe the response of current.
- (iii) Galvanodynamic - current sweep is applied to observe the response in potential.
- (iv) Galvanostatic - application of a current pulse to observe the response in potential.

As shown schematically in figure 2.25, this relationship between potential and current is approximately linear. By calculating the slope of this linear region, the polarization resistance is then determined using equation 2.18 (Poursaei 2010). Polarization resistance is defined as the resistance of a metal to oxidation while an external potential is applied.

$$R_P = \frac{\Delta E}{\Delta I} \quad (2.18)$$

where R_P is the polarisation resistance in ohm (Ω), ΔE is the change in potential (V) and ΔI is the change in current (A).

The corrosion current (in μA) is determined from the Stern-Geary equation, equation 2.19 (Stern et al. 1957).

$$I_{corr} = \frac{B}{R_P} \quad (2.19)$$

$$B = \frac{\beta_A \cdot \beta_C}{2.3 \cdot (\beta_A + \beta_C)} \quad (2.20)$$

where B is the Stern-Geary constant, β_A is the anodic Tafel slope (mV) and β_C is the cathodic Tafel slope (mV). The Stern-Geary constant is typically assumed to be 26 mV and 56 mV for active and passive corrosion respectively (Andrade et al.

2.6 Corrosion assessment and monitoring

1996). The corrosion intensity is then calculated by dividing the corrosion current from equation 2.19 by the polarized steel surface area as shown in equation 2.21.

$$i_{corr} = \frac{I_{corr}}{A_{pol}} \quad (2.21)$$

where i_{corr} is the corrosion intensity ($\mu\text{A}/\text{cm}^2$) and A_{pol} is the polarized steel surface (cm^2).

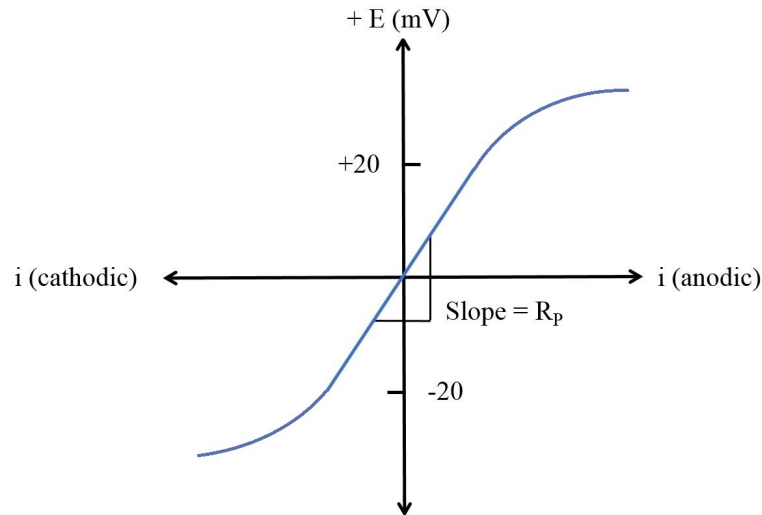


Figure 2.25: Schematic of linear region about the corrosion potential (adapted from Poursaee (2010))

2.6.2.2 Galvanostatic pulse technique

The galvanostatic pulse technique was introduced as a rapid, non-destructive polarization technique by Newton et al. (1988). A small current in the range of 10 - 100 μA is applied galvanostatically between the reinforcement and the counter electrode for a short period, generally between 5 - 30 seconds. The resulting potential from the anodically polarized reinforcement is then recorded by the reference electrode as a function of the polarization time (Elsener et al. 1997). The potential response for a typical galvanostatic pulse corrosion rate measurement is shown in figure 2.26.

2.6 Corrosion assessment and monitoring

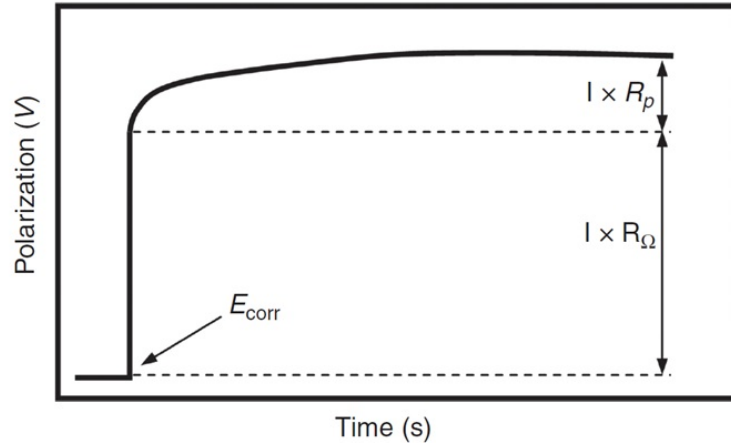


Figure 2.26: Typical galvanostatic pulse result (Poursaei 2010)

The polarization of the reinforcement (η_t) at time (t) and constant applied current (I_{app}) is then shown in equation 2.22 (Jones et al. 1966).

$$\eta_t = I_{app} \cdot \left(R_P \left(1 - e^{-\frac{t}{R_P \times C_{dl}}} \right) + R_\Omega \right) \quad (2.22)$$

where η_t is the polarization of the reinforcement (mV), R_P is the polarization resistance (Ω), C_{dl} is the double-layer capacitance (C) and R_Ω is the ohmic resistance of the concrete (Ω).

Equation 2.22 is then transformed into logarithmic form used to calculate C_{dl} and R_P as shown in equation 2.23 (Jones et al. 1966).

$$\ln(\eta_{max} - \eta_t) - \ln(I_{app} \times R_P) - \left(\frac{t}{R_P \times C_{dl}} \right) \quad (2.23)$$

where η_{max} is the final steady state potential mV. As a schematic illustration, figure 2.27 plots equation 2.23 to show the intercept along the vertical axis.

2.6 Corrosion assessment and monitoring

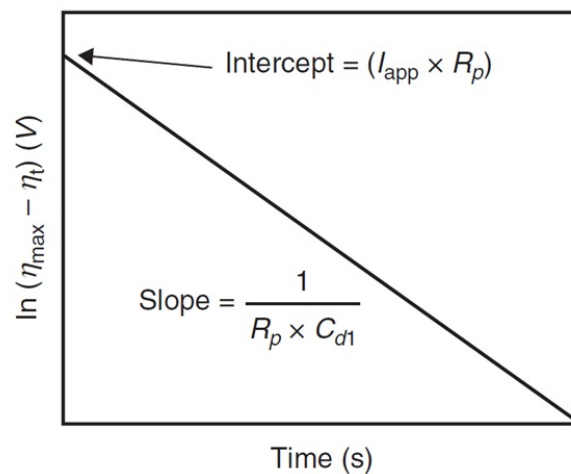


Figure 2.27: Schematic plot of equation 2.23 (Newton et al. 1988)

As shown in figure 2.27, the intercept of $I_{app} \times R_P$ and the slope of the line ($1/R_P \times C_{dl}$) is determined by extrapolating the straight line to $t = 0$ s. The remaining over-potential resembles the ohmic voltage drop experienced over the concrete cover, equivalent to $I_{app} \times R_P$. With the constant applied current known, the polarization resistance is calculated, and consequently, the corrosion intensity from Stern-Geary equation (2.19) (Newton et al. 1988). This study makes use of a commercially available instrument (GECOR-10[®], supplied by ISD[®]) that implements the galvanostatic pulse technique to measure the corrosion rate.

2.6.2.3 Electrochemical impedance spectroscopy

Corrosion measurement through the electrochemical impedance spectroscopy (EIS) technique utilises the frequency domain with the assumption that corrosion on a steel bar can be interpreted as an electrical circuit. The electrical circuit consists of combinations of elements including inductance, capacitance and resistance.

The EIS technique consists of applying a small sinusoidal alternating current (AC) with a low voltage amplitude (10 - 20 mV peak-to-peak) at the working electrode, which is then applied and kept at the E_{corr} (by the potentiostat) for a wide frequency range. This results in a phase change and a different amplitude for each response of every frequency. An impedance, Z , which is the ratio, $\Delta E/\Delta I$, is decomposed into a

2.6 Corrosion assessment and monitoring

capacitive term (phase change of 90°), and a resistive term (in phase with the input signal) as shown in equation 2.24 (Andrade et al. 1996).

$$Z = R_E (R_T/1 + j \cdot \omega \cdot C \cdot R_T) \quad (2.24)$$

where ω is the angular frequency ($\omega = 2 \cdot \pi \cdot f$), j is the imaginary number ($\sqrt{-1}$), C is the electrode resistance (Ω), R_E is the ohmic resistance of the electrode and R_T is the transfer resistance assumed to be equal to polarization resistance (R_P).

Sophisticated equipment is required to perform this method, and is, therefore, considered to be an expensive method of determining the corrosion rate. Although it is only in the development phase, researchers postulate that it might give better insight into the corrosion process, for example the ability to detect localized corrosion and reaction kinetics (Hamdy et al. 2006). However, the application of EIS is still very complex and not a viable solution to on-site corrosion rate measurements (Andrade et al. 2004).

2.6.2.4 Electrochemical Noise

Another transient method for measuring corrosion rate is the electrochemical noise (EN) technique. The EN technique is based on the observation of small voltage variations in the range of μV . A Fourier transform spectrum analyser is used to convert the noise signal from the time domain to the frequency domain, where it can be plotted as amplitude versus frequency. The relation of I_{corr} to electrochemical noise in the case of RC structures is still questionable (Andrade et al. 1996). This technique also requires the use of a sensitive and accurate microvolt, microammeter and spectrum analyser equipment and is, therefore, not a viable solution to measuring on-site corrosion rates.

2.6.2.5 Coulostatic method

The transient response (TR) method is based on the analysis of the response (in a time domain) of an electrode to the application of a current or voltage signal during the first non-stationary period. This method includes various techniques for example the Coulostatic potentiostatic method, which relies on the application of a small current

2.6 Corrosion assessment and monitoring

(10 - 20 mA) to the reinforcement rod for a short period of time (< 10 mS) where after potential decay is observed for a few seconds (Paul 2015). A schematic presentation and an equivalent Randles circuit of the corrosion process (figures 2.28a and 2.28b respectively) can then be used to calculate the polarization resistance (R_P).

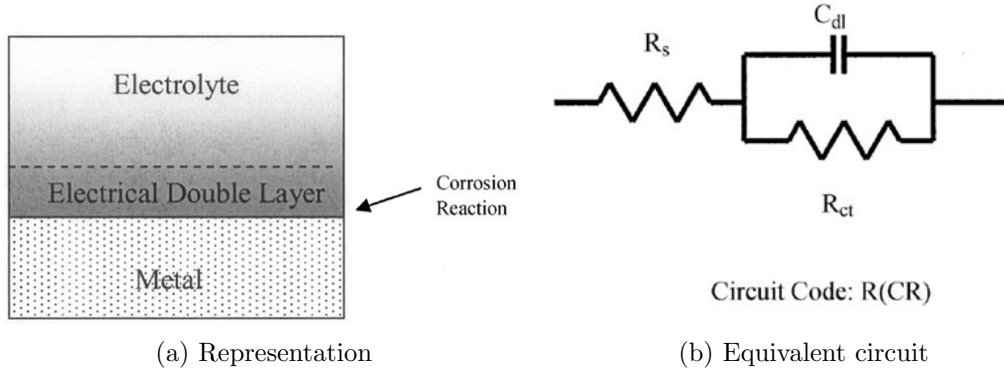


Figure 2.28: Schematic of coulostatic technique circuitry (Chu et al. 2006)

In this model, an active electrolyte resistance (R_S) is connected in series with the parallel combination of the polarization resistance (R_{ct}/R_P) and the double layer capacitance (C_{dl}/C) leading to the calculation of the polarization resistance as shown in equation 2.25 (Paul 2015, pg. 73).

$$\eta_T = \Delta I \cdot R_S + \Delta I \cdot R_P \cdot \exp\left(\frac{-t}{\tau_C}\right) \quad (2.25)$$

where η_T is the total potential change in the working electrode (mV), $\Delta I \cdot R_S$ is the ohmic drop between the working and the reference electrode in the concrete, $\Delta I \cdot R_P$ is the effective polarization at the charging time and τ_C is the coulostatic time constant.

At the instance of disturbance to the applied current, the electric double layer's charge is progressively used in the corrosion reaction, while the electrode potential immediately loses the ohmic drop's ($\Delta I \cdot R_S$) contribution. Therefore, in the process when no current is applied to the reinforcement bar, such as in corrosion testing, the potential decay can be expressed exponentially with time as shown in equation 2.26 (Paul 2015, pg. 74).

$$\eta_T = \eta_0 \cdot \exp\left(\frac{-t}{\tau_C}\right) \quad (2.26)$$

2.6 Corrosion assessment and monitoring

where η_T is the potential shift (ΔE) at time t and η_0 is the initial shift potential. Following equations 2.25 and 2.26, the polarization resistance (R_P) can be calculated from the inter-facial layer (C) and the coulostatic time (τ_C) as shown in equations 2.27 to 2.29.

$$R_P = \frac{\tau_C}{C} \quad (2.27)$$

$$C = \frac{q}{\eta_0} \quad (2.28)$$

$$q = \frac{t_{pulse} \cdot I_{applied}}{A_{pol}} \quad (2.29)$$

where t_{pulse} is the pulse duration (ms), q is the amount of charge (C), $I_{applied}$ is the applied current (mA) and A_{pol} is the area of polarized steel (cm²).

Finally, the resultant I_{corr} is calculated by dividing the Stern-Geary constant (B) by the R_P as in equation 2.19. As mentioned earlier, the Stern-Geary constant varies between 26 to 52 mV depending on the state of the steel, for example a value of 26 mV was found for the case of active corrosion and 52 mV for a passive state (Gonzalez et al. 1985). Therefore, it is assumed that $B = 26$ mV in this method. An example of a Coulostatic corrosion rate reading is shown in figure 2.29. Regarding the sensitivity of the readings, care should be taken in connecting the wires to the electrical analogue for measuring the response to obtain a good result.

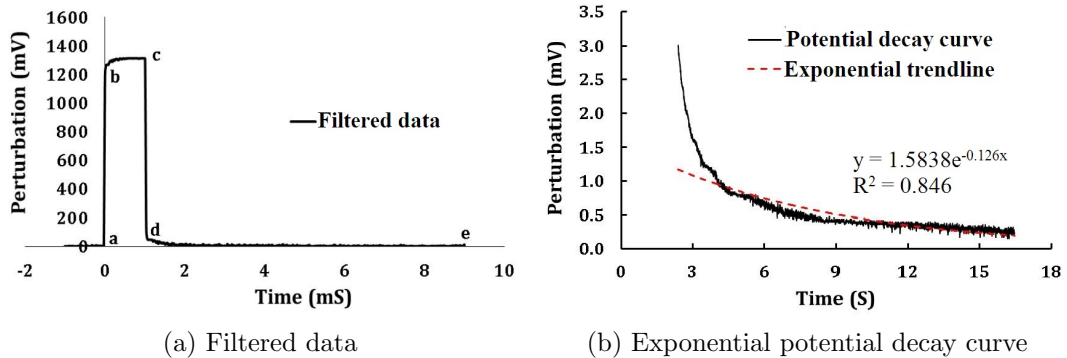


Figure 2.29: Example of Coulostatic corrosion rate measurement (Paul 2015)

The main difficulty in laboratory experiments using the Coulostatic technique is the measurement of localized corrosion. This is because the corrosion pits drain most of the current and thus, the polarization resistance (R_P) may be overestimated

2.6 Corrosion assessment and monitoring

(Andrade et al. 1996). Furthermore, the addition of a stainless steel counter electrode is required to perform corrosion rate readings, limiting the applicability of the corrosion rate measurements to laboratory based specimens. For this reason, the Coulostatic method of corrosion rate measurement is not implemented in this investigation.

2.6.2.6 Confinement of current

Some factors influence the reliability and accuracy of the obtained I_{corr} readings. Examples of these factors are lateral spreading of the current and the sensitive nature of taking corrosion rate readings. In case of the former, the Randles circuit does not accurately model the real behaviour and the calculated I_{corr} values are overestimated, especially in the case of non-corroding reinforcement rods (Elsener et al. 1994). An example of lateral spreading of the current is shown in figure 2.30a.

The limitation of lateral spreading of the current can be resolved if the length of polarized steel surface area is known. The length of the polarised steel surface can be calculated at the end of the experiment by measuring the actual length of the corrosion region. However, in the confinement of current method, the lateral spreading of the current is avoided. This is due to the fact that the current is limited to a known polarisation length, shown in figure 2.30b.

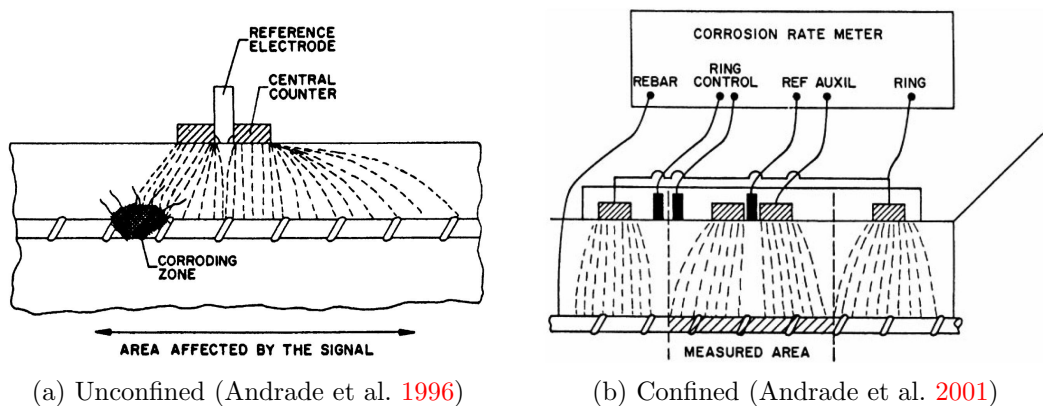


Figure 2.30: Unconfined vs. confined corrosion current measurement

By confining the polarization to a known length, the overestimation of R_p is reduced. This is known as confinement of the applied current. This approach utilizes an

2.6 Corrosion assessment and monitoring

additional counter electrode (CE), called the guard ring counter electrode (GRCE), which is positioned around the outside of the sensor. This annular arrangement of stainless-steel rings is shown in figure 2.31.

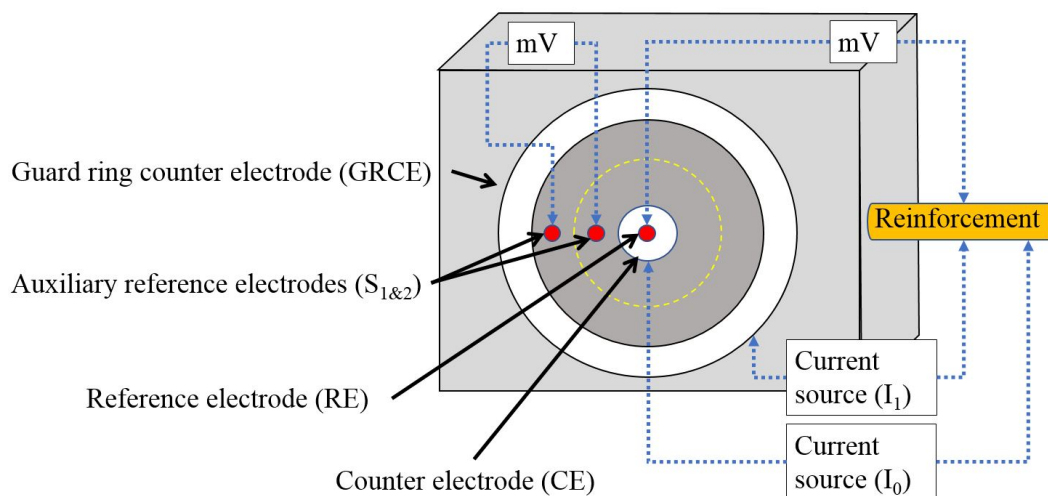


Figure 2.31: Schematic confinement of current circuitry (adapted from Andrade et al. (1996))

The dispersion of non-uniform current as shown in figure 2.30a is eliminated by confining the area of polarized steel surface to directly underneath the sensor. During the polarization procedure, the guard electrode current is adjusted to maintain a constant potential difference between the two auxiliary reference electrodes ($S_{1\&2}$, ring controllers) located between the CE and the GRCE. Figure 2.30b shows the confinement of current underneath the sensor, which minimizes the errors associated with overestimated polarization resistance due to localised attacks.

In this research, the corrosion rate is measured galvanostatically (discussed in section 2.6.2.2) by means of implementing a modulated current confinement technique. It is important to note that the current applied at the secondary electrodes must be controlled or modulated to balance the spreading of potential to just beneath the sensor for the most accurate results. The matter of controlling the application of a second current at the auxiliary electrodes is discussed in section 3.8.1.

2.6 Corrosion assessment and monitoring

2.6.3 Complimentary techniques

Among the corrosion rate measurement techniques, there are some methods that merely serve as an additional aid to the measurement of corrosion. These methods are generally used in the field for the classification of the reinforcement state or concrete quality. Two of the most used semi-qualitative methods are discussed below.

2.6.3.1 Concrete resistivity

Concrete surface resistivity can be measured by the 4-point Wenner point technique as schematised and measured by the four equally spaced probes shown in figures 2.32a and 2.32b respectively. By applying a small alternating current to the outer probes, a potential drop between the inner probes is measured. This, to some extent, eliminates any effects due to the surface contact resistances (Otieno 2014).

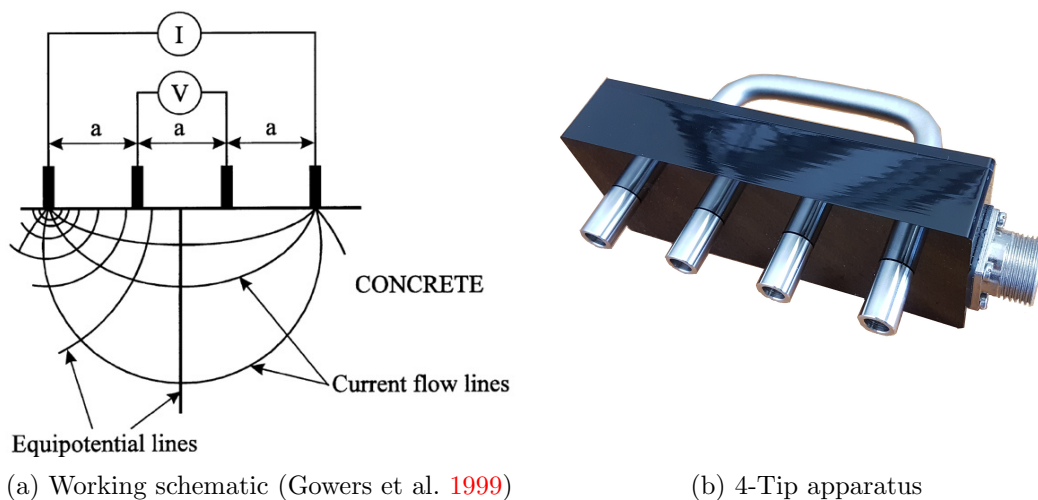


Figure 2.32: 4-Point Wenner probe technique

The electrical resistivity of concrete is expressed in ρ , and measured in $\Omega\text{-cm}$ as shown in equation 2.30 (Gowers et al. 1999).

$$\rho = 2 \cdot \pi \cdot \left(\frac{V}{I} \right) \cdot a \quad (2.30)$$

where a is the probe spacing in cm.

The 4-point Wenner probe of the GECOR-10[®] apparatus (used in this study) has probe spacings 4 cm apart and produces a nominal voltage of 1 V and a current of

2.6 Corrosion assessment and monitoring

100 μA with a resistance of 999 k Ω (*isdcorr* 2015). According to Whiting et al. (2003), there are other factors that influence the electrical resistivity of the 4-probe technique, such as:

- Surface contact
- Concrete non-heterogeneity
- Presence of reinforcement bars
- Geometrical constraints
- Ambient environmental conditions

The relationship between concrete resistivity and the corrosion rate have been investigated by Alonso et al. (1988). It is reported that when steel is passive the differences in resistivity are minor. However, when active corrosion is experienced, the electrical resistivity influences the corrosion rate as illustrated in figure 2.33. This scatter does not show an accurate relationship. Therefore, this technique is not used in the accurate corrosion assessment of concrete structures.

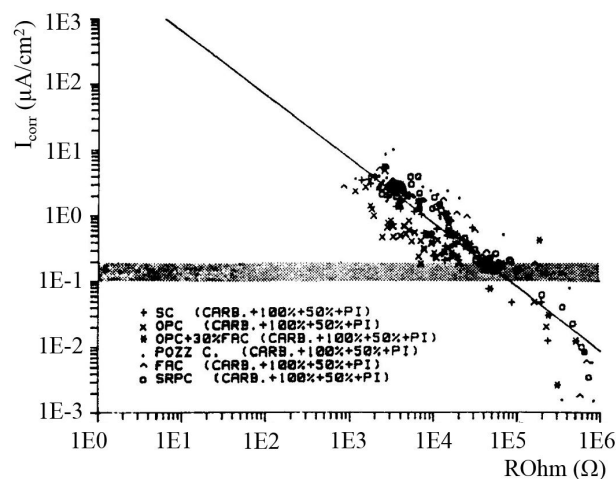


Figure 2.33: Scatter of I_{corr} vs. resistivity (Alonso et al. 1988)

2.6.3.2 Half-cell potential

Perhaps one of the more common techniques for measuring corrosion probability in RC structures is the half-cell potential electrochemical method. This method is based on the difference between the potentials of the embedded reinforcement and the reference electrode. The reference electrode is referred to as the half-cell which consists of a solution, for example, copper-copper sulphate (Cu/CuSO_4) or silver-silver chloride (Ag/AgCl) (Broomfield 2002). The basic circuitry to this

2.6 Corrosion assessment and monitoring

technique is shown in figure 2.34.

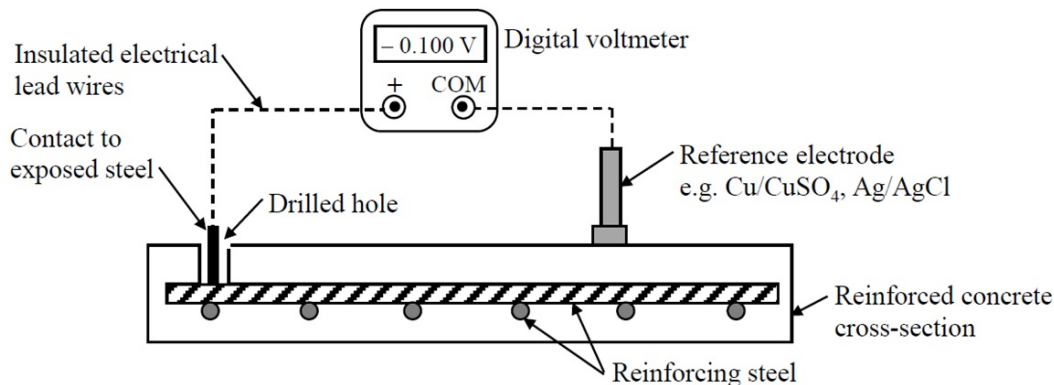


Figure 2.34: Schematic half-cell potential circuit (Broomfield 2002)

The basic circuitry illustrates the need to make an electrical connection to the reinforcement rods within the concrete. This is a standard method for inspecting the corrosion probability or RC structures as set out by the American Standards (ASTM 2015). The measured potential of the rebar is then used to indicate a probability of corrosion at certain corrosion potential (E_{corr}) values for both types of half-cells, namely the copper-copper sulphate electrode (CSE) and the silver-silver chloride electrode (SCE) as shown in table 2.7.

Table 2.7: Corrosion probability for half-cell potential (ASTM 2015)

Corrosion potential (E_{corr})		Probability of corrosion
(mV vs. CSE ^a)	(mV vs. SCE ^b)	
$E_{corr} \geq -200$	$E_{corr} \geq -125$	Low risk
$-200 \leq E_{corr} \leq -350$	$-126 \leq E_{corr} \leq -125$	Intermediate risk
$E_{corr} \leq -350$	$E_{corr} \leq -276$	High risk
$E_{corr} \leq -500$	$E_{corr} \leq -426$	Severe corrosion

Note: ^a $Cu/CuSO_4$ and ^b $Ag/AgCl$

The potential measuring probe containing the CSE solution is shown in figure 2.35. The tip of the half-cell generally consists of a porous material which allows it to remain wet by capillary action. The outer sleeve of the probe consists of a non-conductive

2.7 Concluding remarks

plastic tube that houses the saturated solution of copper sulphate in which the copper rod is suspended.

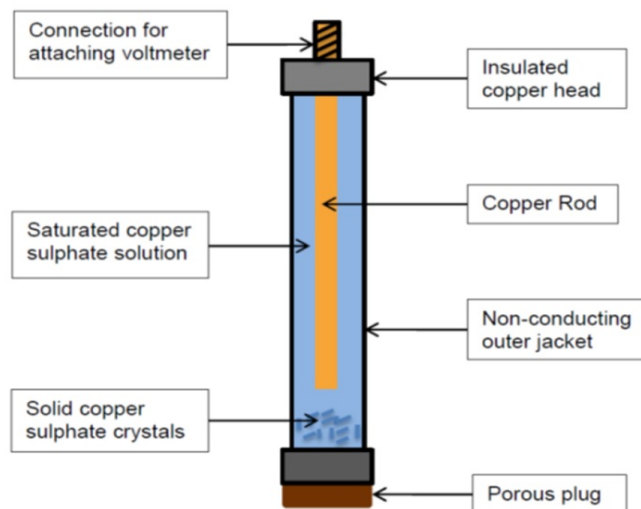


Figure 2.35: HCP reference electrode components (Paul 2015)

It is important to note that this test is only applicable to embedded reinforcing steel that has not been coated with di-electric material. The presence of cracks within the measuring surface also have a significant impact on the potential reading. This is because this method is not calibrated to account for the sodium chloride solution which penetrates through the cracks toward the reinforcement. Various other factors significantly affect the half-cell potential reading. These factors include corrosion inhibitors, oxygen levels, type of steel, concrete density, epoxy-coated reinforcement and chloride content (Paul 2015). Another important consideration is that the half-cell corrosion potential method provides no correlation with the corrosion rate, as these measures respond differently to variables such as concrete resistivity, temperature and moisture content (Broomfield 1994).

2.7 Concluding remarks

This chapter summarises the necessary information for the key topics in the background to chloride-induced corrosion, its accompanying electrochemical processes, factors retarding or propagating it and its assessment. Concrete quality is identified as an important parameter in the durability of RC structures, as it is directly linked to the rate at which corrosion constituents reach the reinforcement

and the continuous supply thereof.

In the presence of cracks in RC members, the period of time before the corrosion constituents reach the steel can be significantly shortened. Cracks facilitate easy transport of the corrosion constituents to the reinforcement, and consequently, result in an increase in corrosion rate. Various crack properties can affect the corrosion rate in a multitude of ways, perhaps most prominently is that of multiple cracks. It is hypothesised in literature that a single crack can lead to localised pitting corrosion, while multiple closely spaced cracks can result in a reduced pitting effect. The pitting corrosion phenomenon is identified as very influential to the durability and structural performance of a RC member.

The electrochemical process between multiple reinforcement rods, and the accompanying complex formations of anode and cathode regions between them and potentially even multiple cracks, still remain uninvestigated. The majority of literature only considers a single crack and steel rod with varying parameters in other fronts. Finally, the definition of corrosion rate was provided, which was identified as critical to performing corrosion assessments of the experimental work executed in chapter 3.

3. Experimental Framework

3.1 Introduction

This chapter describes the experimental methodology followed in this study. The significance to the broader research investigation is discussed along with the technical details and measurement instrumentation used in the experimental setup and configuration. This is followed by the test execution methodology.

In order to test the effects of crack spacing and quantity of reinforcing steel on the corrosion rate, beam size specimens of 150 x 150 x 700 mm were constructed and tested for 36 weeks under accelerated corrosion rate tests. The manufacturing of the specimens is presented in section 3.5. At the end of the experiment the specimens were dismantled to determine the total gravimetric mass loss of the reinforcement. This discussed in section 3.9.

This investigation focuses on the corrosion propagation phase of cracked RC. Concrete specimens were, therefore, cracked in flexure with the crack widths being monitored and maintained monthly to allow for constant crack widths as discussed in section 3.6. Accelerated corrosion testing was performed in laboratory conditions with a constant temperature and relative humidity. This is described in section 3.7. Corrosion rate readings were performed weekly with a commercial corrosion rate measurement device as described in section 3.8.

Finally, supplementary tests were conducted on the reinforcement rods to determine their respective properties. This is concluded in section 3.10.

3.2 Experimental Variables

3.2.1 Reinforcing Steel

All the beam specimens were reinforced with a high yield strength, 10 mm diameter ribbed (Y10) steel bar. This type of steel is typically used in practice locally. To investigate the effects of multiple reinforcement rods on the corrosion rate, three different reinforcement layout configurations are used. These layouts are schematically

3.2 Experimental Variables

shown in figure 3.1 and denoted by the first number representing the number of bars, followed by the bar type (Y represents a high yield ribbed bar) and the second number specifies the diameter of the bar in mm as follows:

- R1 - single reinforcement, 1Y10 bar centrally placed
- R2 - double reinforcement, 2Y10 bars spaced 50 mm apart
- R3 - triple reinforcement, 3Y10 bars spaced 35 mm apart

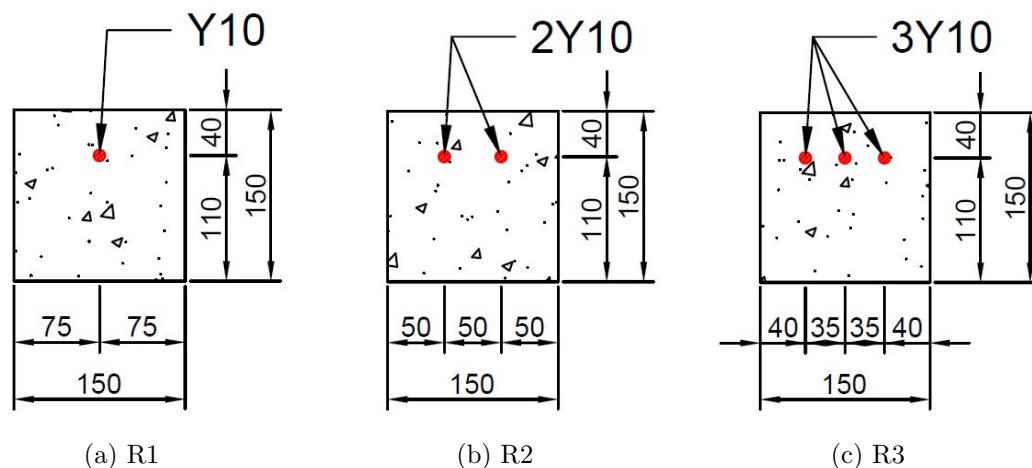


Figure 3.1: Specimen cross-section configurations (dimensions in mm)

It is important to note that all the configurations of reinforcement maintain a 40 mm concrete cover from the exposed side (top) of the specimen. Multiple reinforcement rods in specimen types R2 and R3 are electrically connected in order to study the effect of the electrochemical process on the corrosion rate in the RC beams.

3.2.2 Crack Density

It is postulated in section 2.7 that a single crack might lead to localised corrosion (pitting) while multiple cracks might lead to a more widespread corrosion region over the length of the reinforcement. Widespread cracking also affects the anode to cathode ratio of the corrosion process. Notches of 10 mm deep and 3 mm wide were cut along the specimen in order to facilitate the formation of flexural cracks at the approximate locations. Three different configurations were used and the layout of notches is illustrated in figure 3.2. The notch configurations were labelled as follows:

3.2 Experimental Variables

- N1 - single notch at the center
- N3 - three notches spaced 50 mm apart
- N5 - five notches spaced 30 mm apart

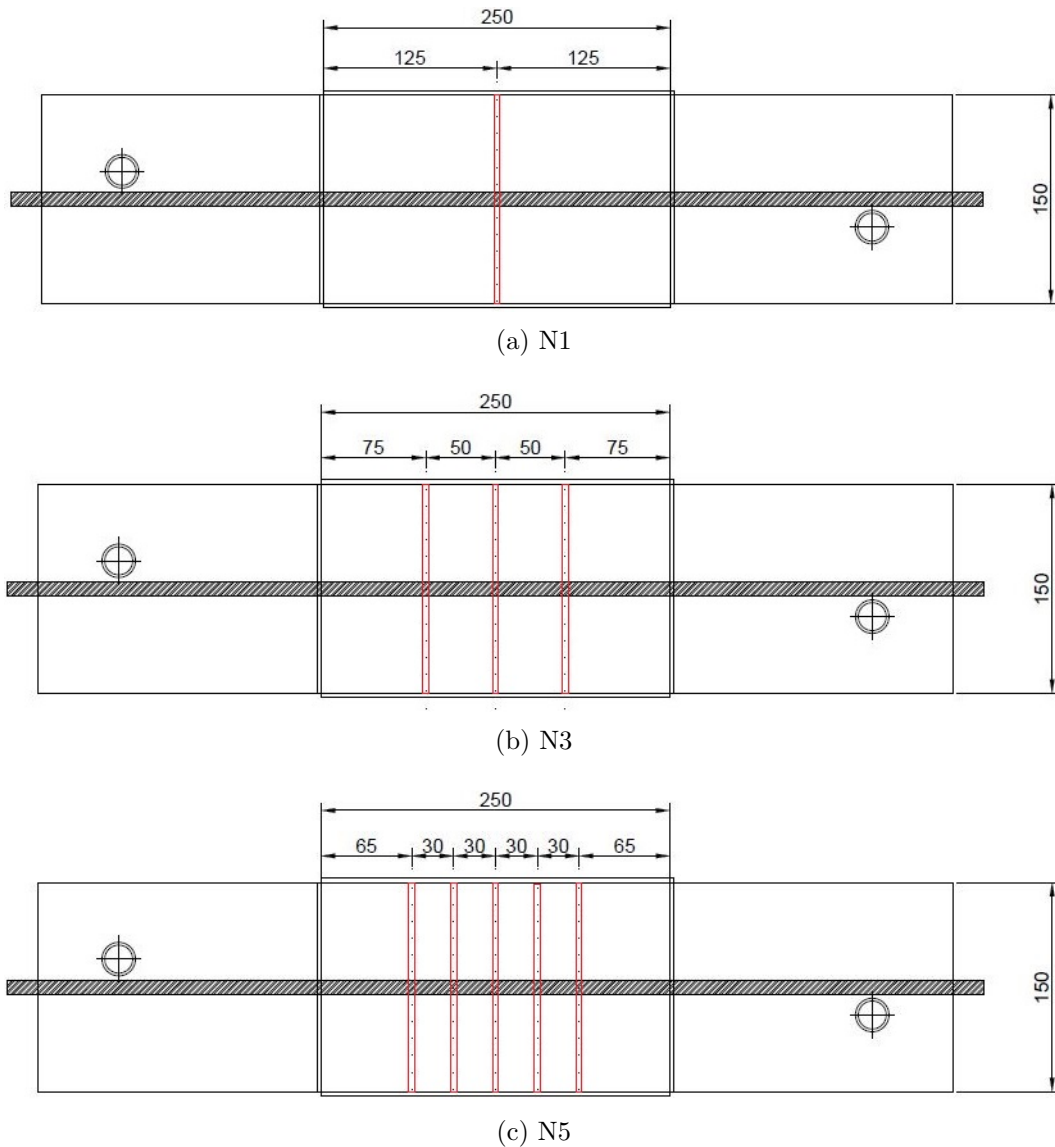


Figure 3.2: Top view of specimen notch configurations (dimensions in mm)

As reported in a later section (section 3.6), not all cracks formed at the approximate notch locations and as a result the crack densities had to be taken into account for each individual specimen. The specimens were then categorized into four different

crack spacings in order to investigate the effect of crack spacing on the corrosion rate.

3.3 Experimental Constants

3.3.1 Binder, Coarse and Fine Aggregate

In order for the emphasis to be placed on the experimental variables discussed in section 3.2, the binder type, w/b ratio, coarse and fine aggregates used in this study are kept constant. Even though it is not recommended to omit the use of extenders in the mix design of chloride laden environments (Owens 2009, Chapter 9), a 100% ordinary Portland Cement (OPC) (Sephaku CEM I 52.5) is used in this mix. This is to ensure that external influences do not affect the consistency of the mix design. For example the influence extenders have on the concrete penetrability and ultimately the corrosion rate.

It is also important to consider that extenders have only been extensively used in recent years. Therefore, RC structures typically older than 30 years are most likely constructed with OPC. As maintenance and rehabilitation for these structures is currently an issue, the long term durability performance of OPC is an important consideration.

Aggregates used in this study are selected based on their attainability and economic viability within the local setting to simulate typical RC mix designs for coastal structures. A 19 mm Greywacke stone, also referred to as Malmesbury shale, was used as course aggregate. It is a metamorphic rock characterised by its grey colour and angular shape and can be a highly reactive with respect to alkali-silica reaction (ASR)(Alexander et al. 1991). Malmesbury coarse sand (size up to 2.36 mm), an evenly graded fine aggregate with a fineness modulus (FM) of 3.3, was used in this study. The grading curves of the coarse and fine aggregate are shown in figure 3.3.

3.3 Experimental Constants

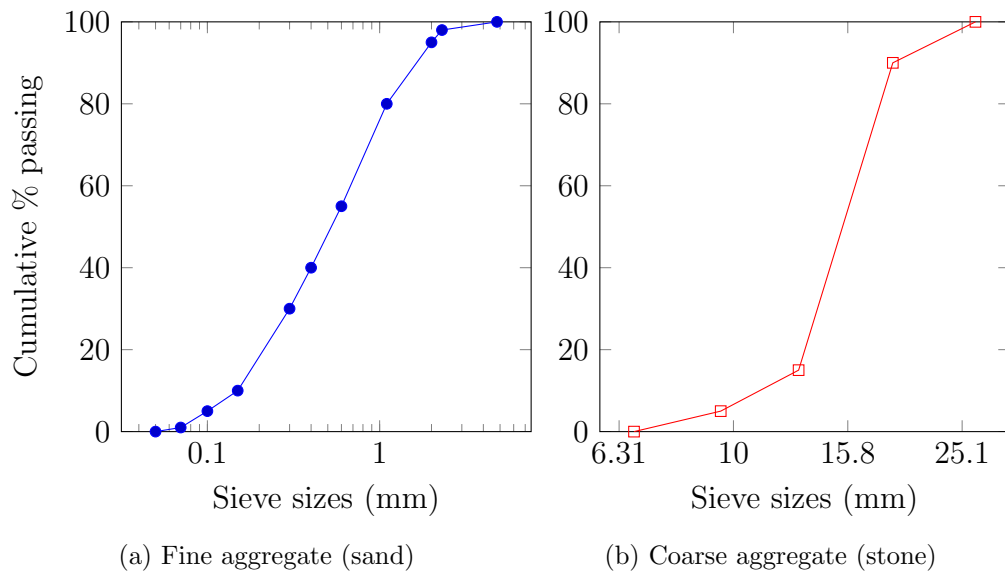


Figure 3.3: Aggregate grading curves

3.3.2 Water/Binder Ratio

For marine exposure Class XS3a (refer to table 2.2) that this study is designed for, the maximum allowed w/b ratio is 0.45 as proposed by the EN-206 (2000). The w/b ratio is inversely proportional to the strength of the concrete and is limited to 0.45 due to its influence on the penetrability of concrete. Higher w/b ratios lead to more penetrable concrete, allowing faster ingress of Cl^- , H_2O and O_2 . A w/b ratio of 0.45 is used in this investigation to keep the variation in specimen penetrability and strength to a minimum.

3.3.3 Crack width

The surface crack width has a substantial effect on the corrosion rate of RC specimens by allowing harmful substances to easily penetrate the concrete. As this study focuses on concrete in the cracked state, a surface crack width of 0.4 mm (tolerance of 0.1 mm) is maintained throughout the experiment to accurately measure the effects of the experimental variables defined in section 3.2. The FIB/Model Code 2010 has previously proposed that 0.4 mm be considered a universal corrosion threshold crack width. Above this threshold adverse crack conditions occur and below corrosion might occur similar to uncracked concrete (Otieno 2014, pg. 200).

3.4 Concrete Specimen Properties

Another important thing to note is that surface crack widths of less than 0.3 mm are prone to self-healing (Neville 2002). This process is generally retarded in the presence of dynamic loads as discussed in section 2.5.4.5. Furthermore, the effects of self-healing of small cracks with large covers (typically > 40 mm) are enhanced due to the effective crack width reducing along the depth of the cover. It was not possible to quantify or ascertain the effects of self-healing in this experimental program, but this is limited as far as possible by avoiding load dormancy (discussed in section 3.6).

3.3.4 Concrete Cover

The concrete cover in all the specimens were designed according to the South African concrete design code (SANS 10100-2) and the Eurocode (Eurocode 2 (2004)). These standards allow a minimum cover of 40 mm for normal density concrete exposed to severe environmental conditions. This investigation therefore emulates normal design practice for concrete structures within the tidal marine conditions.

3.4 Concrete Specimen Properties

3.4.1 Concrete mix design

In order to achieve good durability performance, a suitable mix design is determined to ensure the concrete mix meets anticipated properties in both the fresh and hardened state. Mix design methods generally compose of graphs, charts, tables and empirical relations to form standards for locally available materials. The ACI 211.1-91 method of calculating mix proportions is modified for South African practice and is referred to as the Cement and Concrete Institute (C & CI) volumetric mix design method. This mix design method is based on the requirement that the total volume of concrete should be equal to the sum of the absolute volume of the mix constituents, which are calculated by their respective masses (Owens 2009, Chapter 11). The mix proportions used in this study is shown in table 3.1.

3.4 Concrete Specimen Properties

Table 3.1: Concrete mix proportions

Material	(kg/m ³)	Comment
OPC (CEM I 52.5N)	467	Supplied by Sephaku
Water	210	Potable tap water
Fine Aggregate	425	Malmesbury Coarse Sand
Coarse Aggregate	1326	Greywacke Stone (19 mm)
	1000 <i>l</i>	
w/b ratio	0.45	
a/b ratio	3.10	
Slump (mm)	105	

Compressive tests were performed on 100 mm cube specimens to characterise the concrete class according to [SANS-5863 \(1994\)](#). One day after casting, all of the specimens were stripped from the moulds and water cured at $23 \pm 2^\circ\text{C}$ for 7 days. Thereafter, the specimens were kept in laboratory conditions at $25 \pm 2^\circ\text{C}$ and RH of $65 \pm 5\%$. Specimens were kept in these conditions until the compression testing date. Compression tests were performed in a 2 MN Contest Materials Testing Machine (MTM). Table 3.2 shows the compressive strength (f_{cu}) results.

Table 3.2: Concrete compressive strength properties

Age of testing	f_{cu} (MPa)	CoV (%)	Nr. of cubes
7 day average	49.4	7.2	12
28 day average	59.1	11.9	12

3.4.2 Specimen dimensions and sample size

In a study by Angst et al. (2010), it was identified that the size of the specimen can affect the corrosion process if the areas available for the cathode is inefficient within the specimen. However, localized corrosion is assumed to be the dominant corrosion mechanism within this study. It is important to provide an adequate spacing between the reinforcing bars which obeys steel bar detailing rules that allow aggregates to pass through, in order to simulate actual RC beams adequately. Therefore, a specimen size of 150 x 150 x 700 mm was chosen as shown in figure 3.4.

3.5 Casting and Curing of Specimens

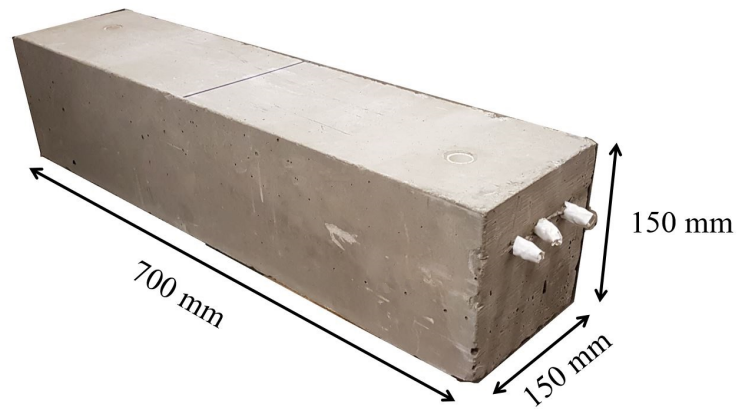


Figure 3.4: Typical 150 x 150 x 700 mm concrete specimen

A total of three specimens were cast for each experimental variable. It is acknowledged that this is a small sample size, but it represents a minimum from which trends may be derived. The summary of experimental variables is illustrated in figure 3.5 representing $3 \times 3 \times 3 = 27$ specimens.

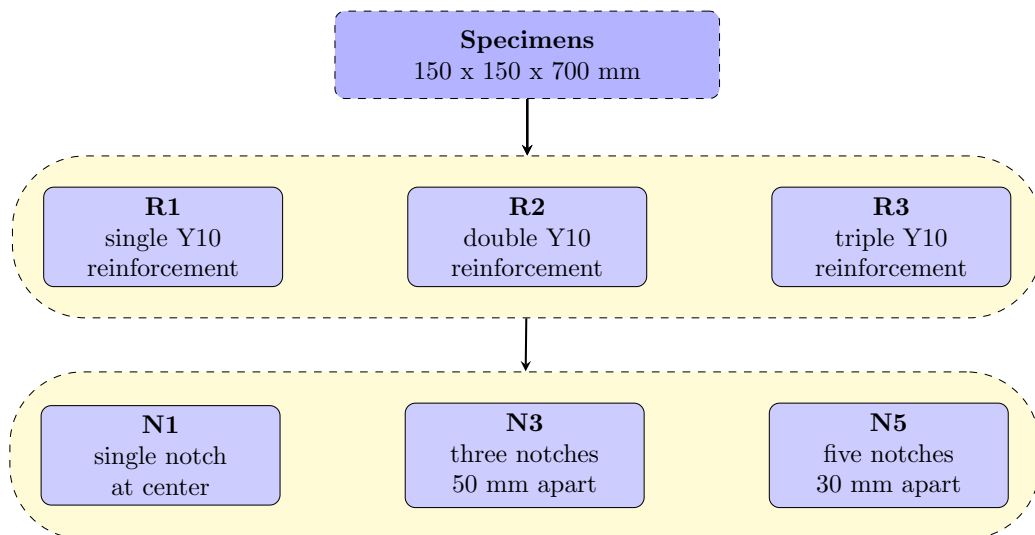


Figure 3.5: Summary of experimental variables and sample size

3.5 Casting and Curing of Specimens

Specimens were cast in 150 x 150 x 700 steel moulds that were thoroughly cleaned and lubricated with de-moulding oil prior to each cast. The high yield strength 10 mm diameter ribbed bars complying to **SANS-920** were wire brushed and thoroughly

3.6 Crack Inducement

cleaned with acetone prior to casting. As the reinforcement rod extended out of the concrete specimen on both sides, insulation tape was used to cover the exposed ends. This was done to ensure no corrosion processes outside the specimen would effect the readings (as seen in figure 3.4). The reinforcement rods were then held in place with wooden spacer blocks at both ends of the mould. Provision for thread bar was made by placing a pvc tube at the ends of the specimen as shown in figure 3.6a. Fresh concrete placed in the moulds was vibrated with a poker vibrator to ensure good compaction (figure 3.6b) before being covered by a polythene sheet for 24 hours to ensure good curing practice.

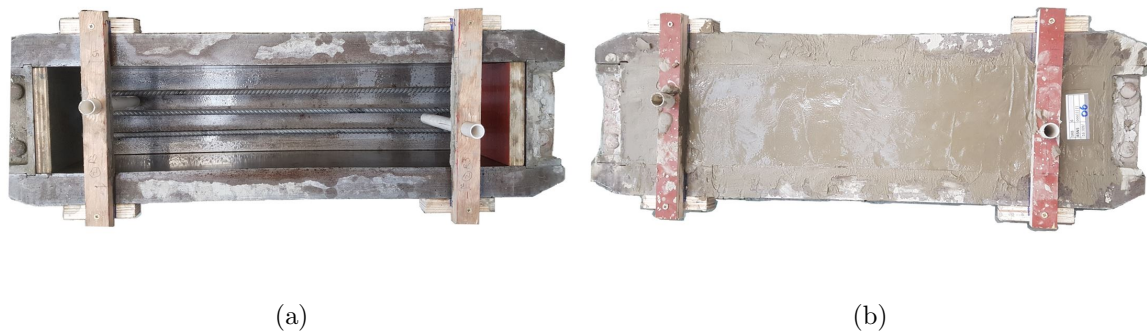


Figure 3.6: (a) Specimen mould prior to, and (b) after casting

Specimens were then cured for 24 hours within the cast iron moulds at ambient laboratory conditions ($23 \pm 3^\circ\text{C}$). Afterwards, they were de-moulded and then cured for a further 28-days in a water bath ($23 \pm 2^\circ\text{C}$) before cracks were induced.

3.6 Crack Inducement

3.6.1 Pre-cracking

All 27 beam specimens were pre-cracked in flexure before being subjected to corrosion testing. After 28-days of water bath curing, specimens containing a single notch were subjected to three-point flexural bending (figures 3.7a and 3.7c) while specimens containing multiple notches were subjected to four-point bending (figures 3.7b and 3.7d). The pre-cracking was performed using an Instron materials testing machine (MTM), at a constant cross-head rate of 0.05 mm/min. Specimens were unloaded once a crack width of 0.3 ± 0.1 mm was observed or if a load drop of 250 N was detected.

3.6 Crack Inducement

The crack width is initially measured with a crack width gauge card, and in later stages confirmed with a digital vernier caliper with a 0.01 mm resolution.

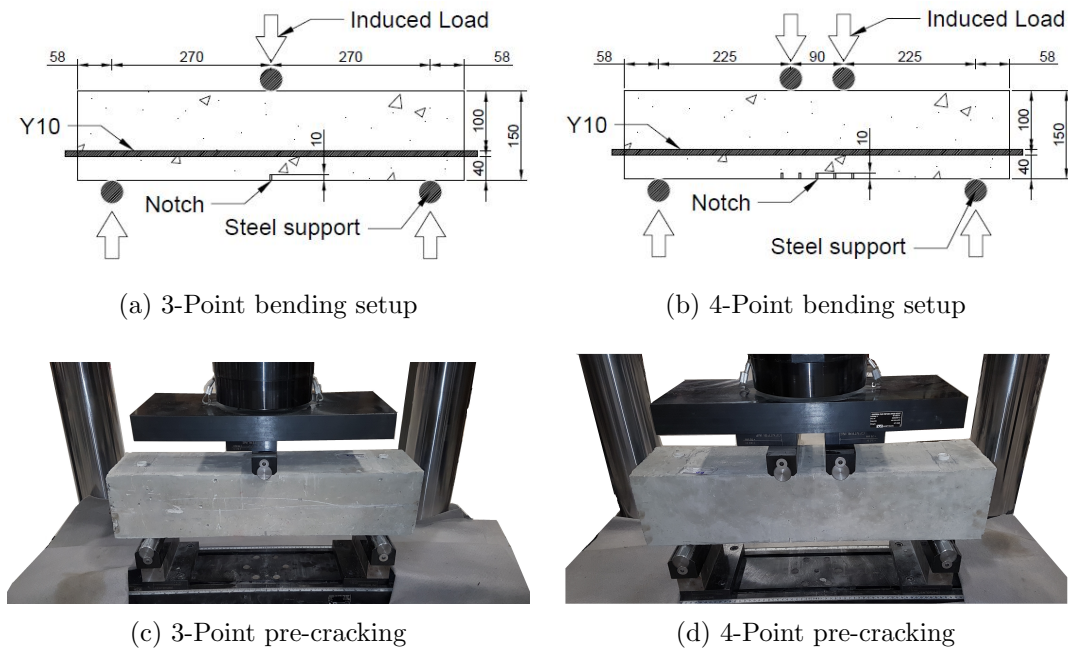
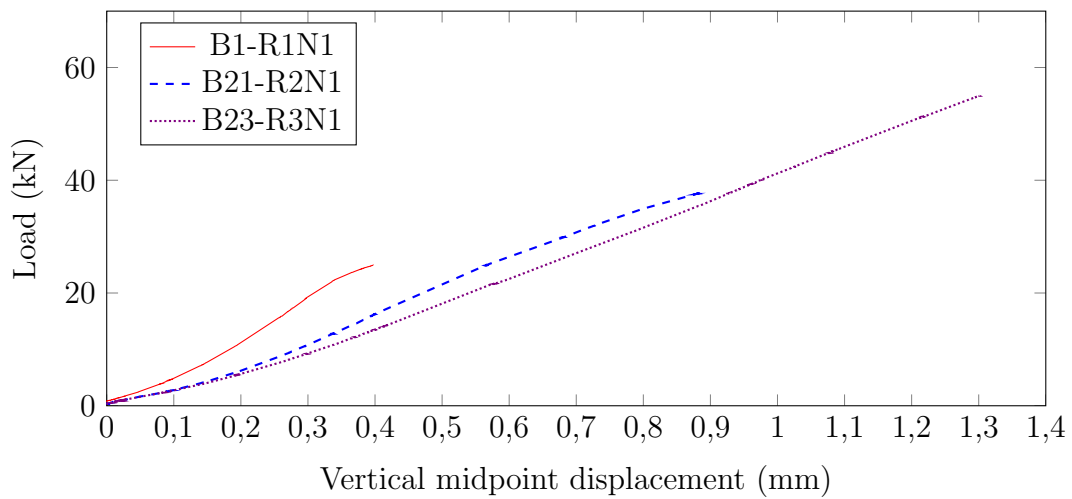


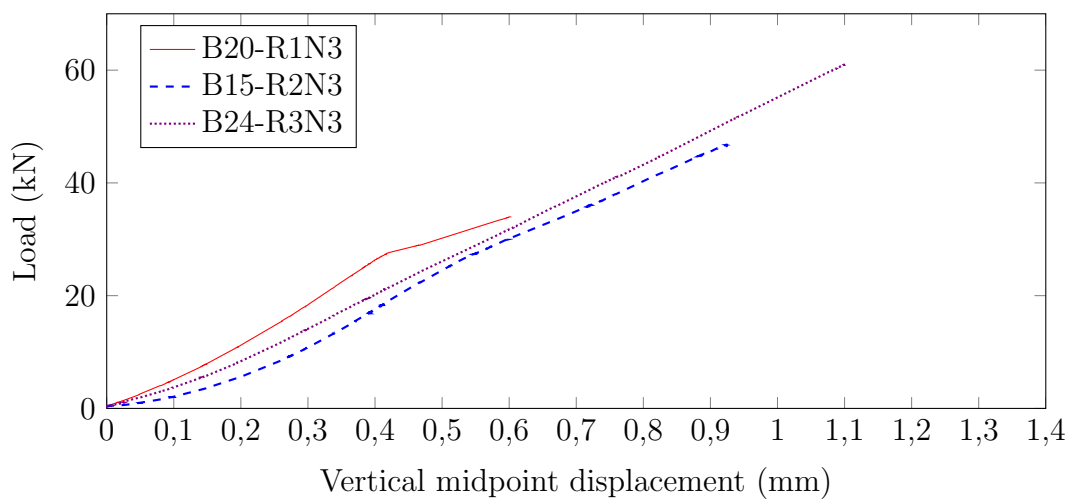
Figure 3.7: Specimen pre-cracking in MTM

The imposed load required to attain the given crack width in each specimen was recorded. The flexural pre-cracking forces are summarised in table 3.3, while the full documentation of results are given in appendix A.1. A typical response curve for the three different reinforcement layouts subjected to three- and four-point bending is shown in figure 3.8. An approximately linear response curve is observed. Once the load was removed, all the cracks closed to their incipient crack state with virtually zero surface crack width. Due to this, all specimens were then placed in a 3- and 4-point loading rig for sustained loading as discussed in section 3.6.2.

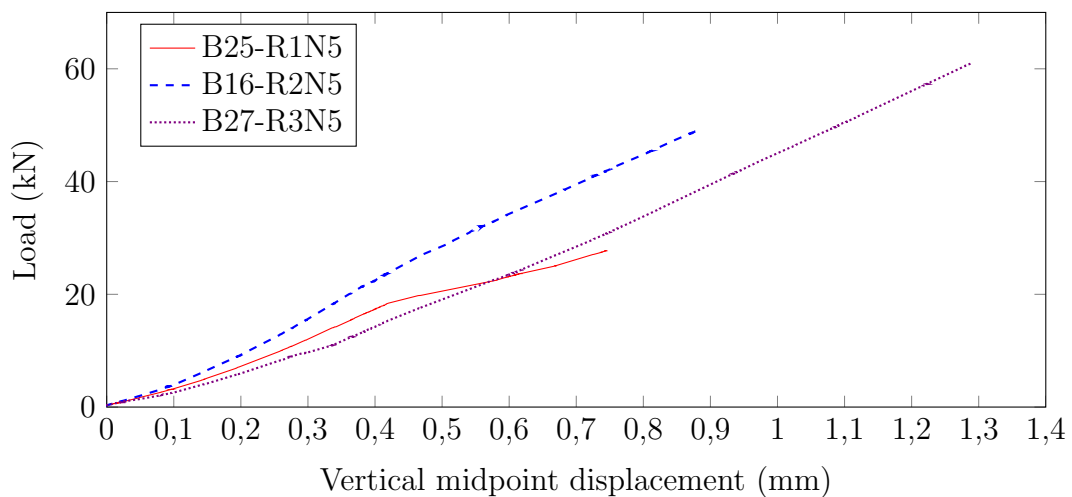
3.6 Crack Inducement



(a) N1 - 3-point bending at center



(b) N3 - 4-point bending at 75 mm apart



(c) N5 - 4point bending at 100 mm apart

Figure 3.8: Typical specimen response

Table 3.3: Flexural pre-cracking loads

Series	Notch spacing (mm)	Avg. load (kN)	CoV (%)
R1	1 N - Single notch	24.3	4.74
	3 N - 50	30.4	10.6
	5 N - 30	31.3	9.75
R2	1 N - Single notch	40.1	5.00
	3 N - 50	46.3	3.29
	5 N - 30	49.0	1.22
R3	1 N - Single notch	55.1	1.81
	3 N - 50	60.1	3.45
	5 N - 30	62.3	0.92

As reported in section 5.2, the level of steel stress influences the corrosion rate. A higher steel stress generally leads to an increased number of micro-cracks. These micro-cracks weaken the steel-concrete bond, inducing more micro-cracks and increasing the penetrability of the concrete (Blagojević 2015). The influence of the steel-stress level was not considered as an experimental variable but was analytically verified in section 5.2 and compared between the different steel stresses of R1, R2 and R3 series.

3.6.2 Sustained specimen loading

After the incipient cracks were formed by the Instron MTM, the specimens were once again loaded in either 3- or 4-point loading to achieve a surface crack width of 0.4 ± 0.1 mm. Specimens with multiple notches were cracked in 4-point bending as shown in figure 3.9, while single notch specimens were loaded in 3-point bending.

3.6 Crack Inducement

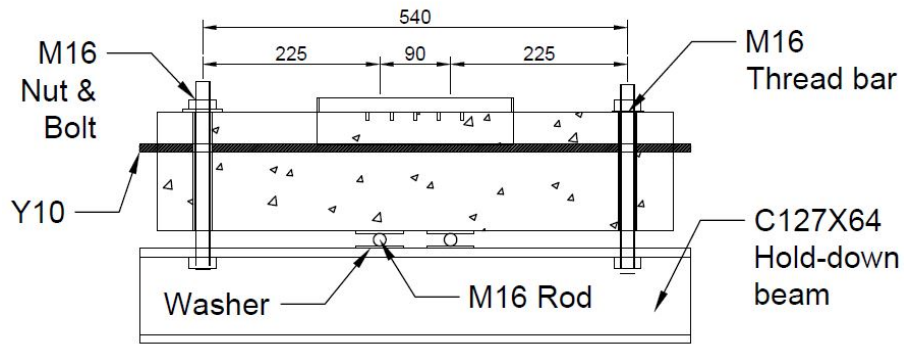


Figure 3.9: Schematic of 4-point loading rig (dimensions in mm)

A crack width gauge was used to monitor the surface crack width (w_c) monthly. This was done to ensure a constant 0.4 mm crack width over the course of the experiment. If any adjustments were required, the loading rig was manually adjusted by tightening the bolts to achieve the required w_c . For all three reinforcement configurations, all cracks observed were transverse to the steel bar and there were no parallel cracks. As not all cracks formed by the notches, the actual crack spacing (S_c) between the formed cracks had to be measured. The crack spacings were then accounted for in a frequency graph along the length of the beam as shown in figure 3.10. These frequency graphs include all the cracks for in the R1, R2, and R3 series. Individual specimens had an average of two cracks per beam (excluding single cracked specimens).

3.6 Crack Inducement

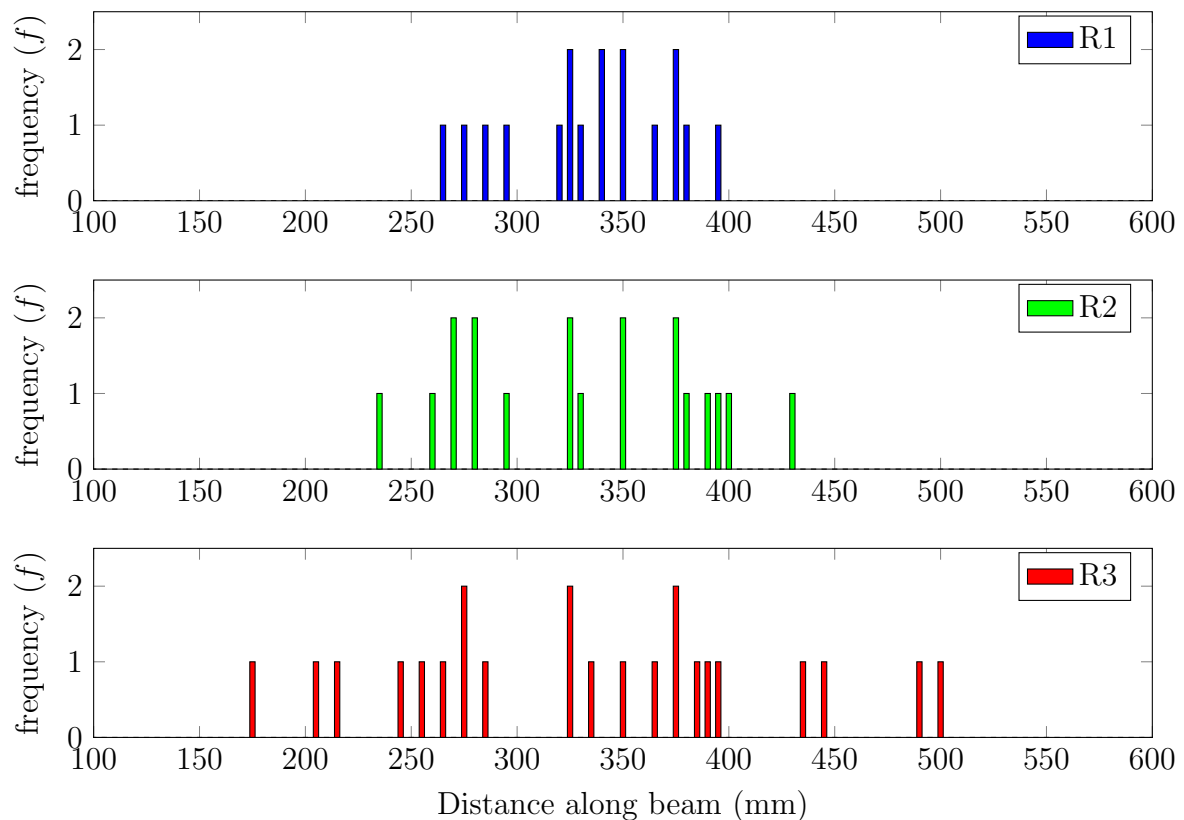


Figure 3.10: Surface crack distribution

From the crack distribution results, it appears that the single bar (and weakest bending capacity) reinforced beams of the R1 series show an expected flexure cracking result at the midpoint (350 mm) of the beam. The R2 series also shows a good cracking concentration about the midpoint the beam. The stronger RC beams of the R3 series are prone to shear cracking, and therefore, the cracks are more widely distributed with less cracks concentrated around the beam center.

Table 3.4 shows the summary of the crack spacings recorded on each of the specimens (see table A.2 for full results). The cracks spacings are categorised into 4 different groups. The majority of cracks formed with crack spacings of between 85 and 100 mm apart. Specimens with single cracks are presented last in the table as they are considered to have virtually infinite crack spacing. In other words, large enough to ensure that the cathode and anode areas of different cracks are not affected by each other.

Table 3.4: Summary of specimen crack spacings

Series	S_c (mm)	w_c (mm)	Nr. of cracks	Nr. of specimens
S75	$70 \leq S_c \leq 85$	0.4 ± 0.1	2	6: $3 \times R1 + 1 \times R2 + 2 \times R3$
S90	$85 < S_c < 100$	0.4 ± 0.1	2	8: $2 \times R1 + 4 \times R2 + 2 \times R3$
S105	$100 \leq S_c \leq 120$	0.4 ± 0.1	2	6: $1 \times R1 + 2 \times R2 + 3 \times R3$
SC	Single crack	0.4 ± 0.1	1	7: $3 \times R1 + 2 \times R2 + 2 \times R3$

Typical crack formations are shown in figure 3.11 where it is evident that cracks form irregularly despite the notches. In other words, wherever they find the weakest path. For consistency, crack spacing was measured from center to center of the surface cracks.

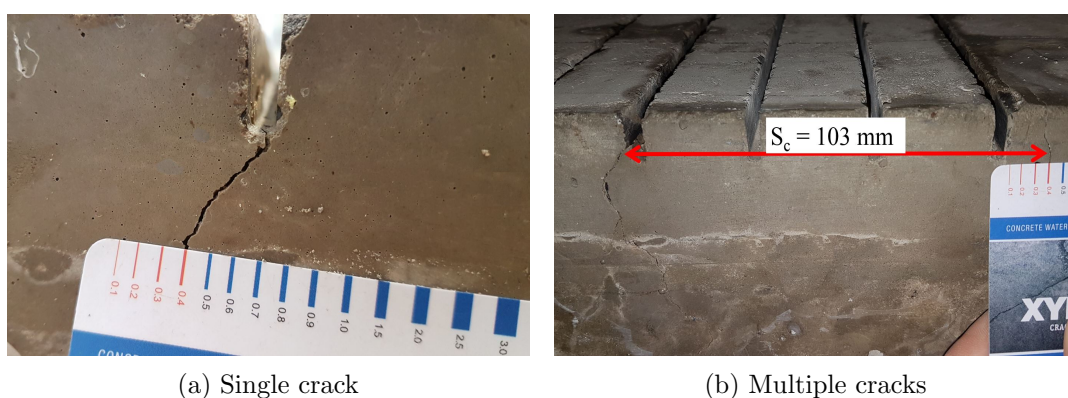


Figure 3.11: Typical crack formation

3.7 Exposure Conditions

3.7.1 Ponding basin

While flexural loading was maintained in the specimens, the upper tensile face was subjected to corrosion testing. This face is referred to as the exposure face. A non-absorbing Perspex frame was constructed on top of the specimen to contain the aqueous saline solution as shown in figure 3.12. The ponding basin was 250 mm long and covered the full beam width (150 mm). This resulted in a exposed surface area of approximately $37\,500\text{ mm}^2$. The perspex frame was tightly sealed to the surface of the concrete with silicone (Alcolin[®] Neutral Cure Silicone, see appendix C.1.2 for product details) to ensure that the basin was watertight. The unexposed sides of the specimens were not coated with epoxy as to allow for internal drying of the concrete.

3.7 Exposure Conditions

The cracks (and a 50 mm offset around them) protruding beyond the Perspex frame on the sides of the beam were sealed with silicone to prevent solution leakage and ingress of corrosion agents (H_2O , O_2 and Cl^-) from the sides of the beam specimens.

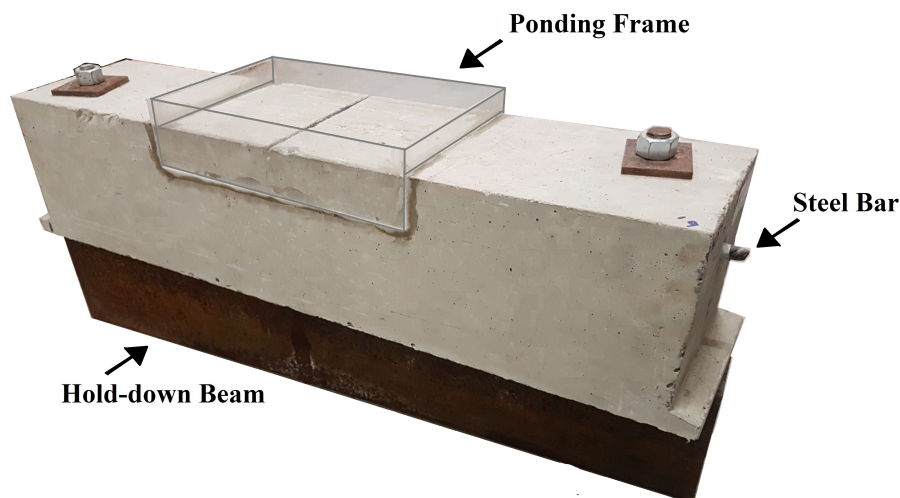


Figure 3.12: Specimen ponding basin on tensile face

3.7.2 Saline solution and ponding cycle

The specimens were ponded with a 5% Sodium Chloride ($NaCl$) solution to simulate Class XS3a (refer to table 2.2) exposure conditions. The 5% $NaCl$ was chosen on the basis that this concentration would yield an equivalent chloride content of about 3% which is roughly 50% more than the chloride content of local sea water (2% Cl content) which was recently measured by Otieno (2014).

This 5% $NaCl$ was then mixed with potable tap water to form a saline solution. Specimens were ponded for 4 days at a time, where after the solution was drained and the specimens were air dried for 10 days. This 2 week cycle was performed continuously for 36 weeks (18 ponding cycles) until the termination of the experiment. See figure 3.16 for the ponding and measurement schedule.

3.7.3 Laboratory conditions

After the 28-day water bath curing and flexural pre-cracking, specimens were positioned in a temperature and humidity controlled room for 40 weeks ($25 \pm 2^\circ C$ and $RH 65 \pm 5\%$) as seen in figure 3.13. All corrosion rate measurements (discussed

3.8 Corrosion assessment

in section 3.8) were performed in this room to ensure that readings were not effected by a variation in temperature or humidity.



Figure 3.13: Photograph of some of the laboratory specimens

3.8 Corrosion assessment

3.8.1 Modulated confinement of the current

The corrosion rate was measured using the galvanostatic pulse technique (a linear polarization resistance technique) whereby a small current ($10 - 100 \mu\text{A}$) is applied statically between the reinforcement and the sensor for a short period (5 – 30 s). The resulting potential from the anodically polarized reinforcement is then recorded by the reference electrode as a function of the polarization time (Elsener et al. 1997). The potential response for a typical galvanostatic pulse measurement is shown in figure 2.26. As discussed in section 2.6.2.2, the principles and theoretical development of the galvanostatic pulse technique is available in literature (Andrade et al. (1996), Wang et al. (2014)).

From chapter 2 it is noted that the quasi-infinite length of the reinforcement can give errors when obtaining the actual length of reinforcement polarized by the counter electrode. This actual length is referred to as the “critical length”. Typical approaches

used to solve this uncertainty of critical length, and therefore, the area really polarized (*true* R_P), are as follows (Andrade et al. 1996, pg. 322):

- Transmission line model - lateral spreading of the electrical signal compensation
- Non-uniform lateral spreading of the current technique
- Confinement of the applied electrical signal

However, only the confinement of applied electrical signal to determine the *true* R_P is used in this study.

The confinement of current technique relies on a guard ring counter electrode (GRCE) to confine the current in a particular reinforcement area as shown in figure 2.31. A galvanostatic step is applied to both the central counter electrode (CCE) and the GRCE. It is important to note that the difference between uncontrolled and controlled applications of the outer applied current, as the former generally results in erroneous *true* R_P values. To eliminate this error, two reference electrodes (see figure 3.14a) are placed between the central and external ring counter electrodes. This equilibrates internal and external current to allow for the correct calculation of *true* R_P . For accurate corrosion intensity results, it is vital to make use of the modulated confinement of current (MCC) method for determining the correct *true* R_P .

The corrosion rates are measured by a commercially available portable corrosion rate measurement device, GECOR-10[®], supplied by ISD[®] (see appendix C.1.1 for instrument details). The GECOR-10 implements the MCC method in the application of the galvanostatic pulse technique when corrosion rate readings are taken. The corrosion rate sensor, shown in figure 3.14a, has an outer guard ring counter electrode diameter of 14.0 cm and a central counter electrode diameter of 3.0 cm. The two auxiliary reference electrodes, S_1 and S_2 , are placed at 2.375 cm and 4.125 cm away from the central electrode respectively. This allows for an effective sensor polarization diameter of $\varnothing_{sensor} = 6.5$ cm ($A_{eff} = 33.20$ cm²).

3.8.2 Measurement procedure

As mentioned in section 3.2.1, all reinforcement bars were electrically connected by a wire at the beginning of the experiment. Upon taking readings with the GECOR-10, the bars were kept connected. Equation 3.1 shows the adjustments made to the polarization area of the steel rod to include the effects of all the bars present in the corrosion rate measurement. This adjustment is directly entered into the GECOR-10 by specifying the total bar diameter present in the corrosion rate measurement. The sum of their diameters is used for the calculation of the affected area as shown in equation 3.1 (*isdcorr 2015*).

$$A_{pol} = N_{bars} \cdot \varnothing_{rebar} \cdot \pi \cdot \varnothing_{sensor} \quad (3.1)$$

$$A_{R1} = 1 \cdot 1.0 \cdot \pi \cdot 6.5 = 20.4 \text{ cm}^2$$

$$A_{R2} = 2 \cdot 1.0 \cdot \pi \cdot 6.5 = 40.8 \text{ cm}^2$$

$$A_{R3} = 3 \cdot 1.0 \cdot \pi \cdot 6.5 = 60.2 \text{ cm}^2$$

where A_{pol} is the area of bar polarized by the equipment (cm^2), N_{bars} is the number of bars present in the corrosion rate reading, \varnothing_{rebar} is the diameter of a single reinforcement rod (cm) and \varnothing_{sensor} is the effective diameter of the corrosion rate sensor (GECOR-10 $\varnothing_{sensor} = 6.5 \text{ cm}$).

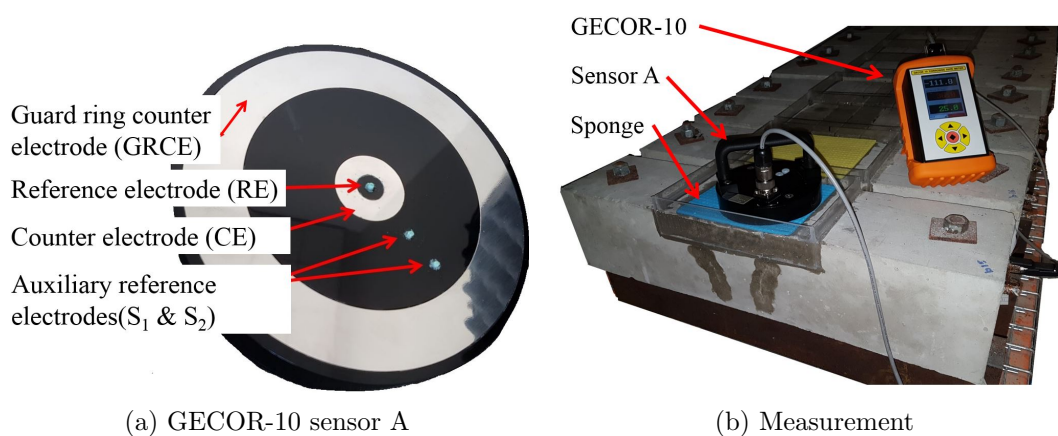


Figure 3.14: Measurement of corrosion rate with GECOR-10

Prior to measurement, a thin (5 mm) water saturated sponge is placed between the sensor and the concrete specimen to ensure good contact between the specimen and the reference electrodes. The saturated sponge is conductive to the applied galvanic pulse and care is taken to ensure that the sponge always maintains a similar level

3.8 Corrosion assessment

of moisture. Another check done before performing a reading is ensuring that the electrode tips (see figure 3.14a) are blue. This indicates that they are saturated with $Cu/CuSO_4$ necessary for taking a measurement. If both these checks are fulfilled, three corrosion rate readings are performed on a beam specimen in the pattern shown in figure 3.15. Each corrosion rate reading is taken approximately 60 seconds after the previous reading to allow for the storage of data and the repositioning of the sensor.

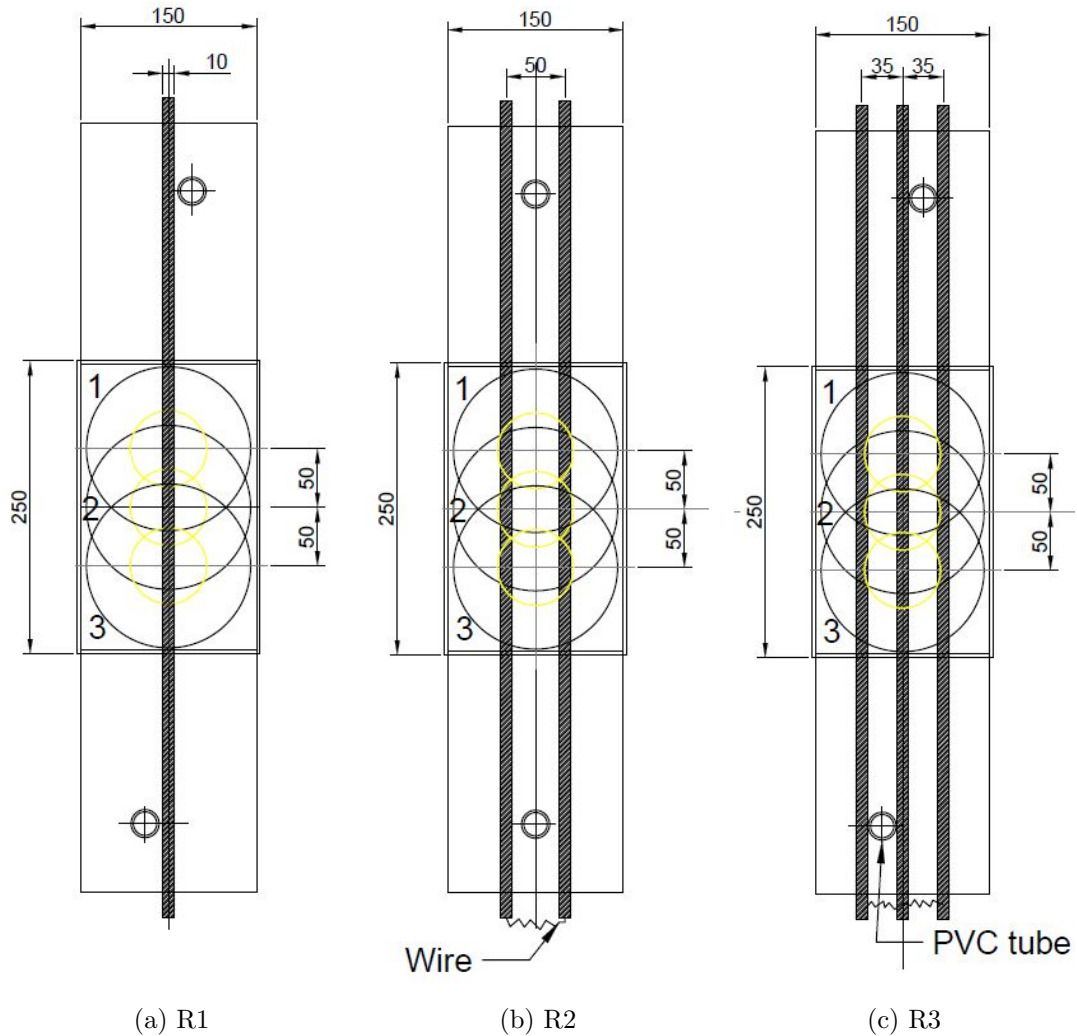


Figure 3.15: Locations of corrosion rate readings (dimensions in mm)

Three readings were taken per beam, each spaced 50 mm apart from the previous reading. The average of the three corrosion rate readings is reported in chapter 4, and is referred to as the 3-point moving average i_{corr} reading. In summary, the corrosion

3.9 Destruction of specimens

rate reported is equivalent to the corrosion current divided by the polarization area underneath the sensor as entered into the GECOR-10.

As shown in chapter 4, the period when corrosion rate readings are taken also influences the corrosion rate. Figure 3.16 shows the cyclic wetting and drying cycle in relation to when corrosion rate readings were taken. One day after ponding is referred to as a “Wet measurement”, while corrosion rate readings taken 8 days after ponding is referred to as a “Dry measurement”. Corrosion rates were taken once a week for 36 weeks.

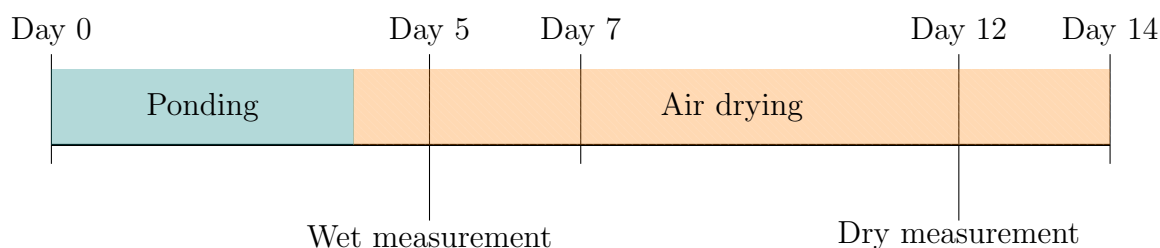


Figure 3.16: 14-Day measurement and ponding schedule

3.9 Destruction of specimens

3.9.1 Gravimetric mass loss

The comparison between the predicted electrochemical weight loss and the actual weight loss is made through a gravimetric study of the bars after corrosion testing. After 36 weeks of corrosion testing, the specimens were broken in preparation of the gravimetric weight loss method used to determine the actual mass of iron oxidized in the corrosion process. The preparation, cleaning and estimation of mass loss is done in accordance with standard practice of corrosion testing ([ASTM G1-03 \(2011\)](#)). The cleaning involves the use of 100 g of stannous chloride, 40 g of antimony trioxide and 2000 ml of hydrochloric acid. The gravimetric mass loss is then calculated as follows:

$$\Delta W = W_{start} - W_{end} \quad (3.2)$$

where ΔW is the total mass loss suffered by the steel bar, W_{start} is the mass after cleaning with acetone and prior to casting and W_{end} is the mass after the end of the experiment and cleaning, all measured in grams. The gravimetric mass loss is then compared to the electrochemical mass loss calculated by integrating the i_{corr} readings

3.9 Destruction of specimens

over time (each week's mass loss is added cumulatively). The electrochemical mass loss is calculated from Faraday's law, shown in equation 3.3 (Andrade et al. 2005).

$$\frac{i_{corr} \cdot t}{F} = \frac{\Delta W}{P_{eq}} \quad (3.3)$$

where i_{corr} is the corrosion current density ($\mu\text{A}/\text{cm}^2$), t is the time of the electrolysis (s), F is the Faraday constant (96 500 C) and P_{eq} is the equivalent mass of the oxidation reaction ($Fe \rightarrow Fe^{2+}$). As shown in equation 2.17, P_{eq} is simply the molecular mass of iron ($M_{Fe} = 55.845 \text{ g/mol}$) divided by the valency of iron ($Z = +2$). Equation 3.3 is then simplified to equation 3.4.

$$\Delta W = 0.0116 \cdot i_{corr} \cdot t \cdot \alpha_{pit} \quad (3.4)$$

where α_{pit} is the localised pitting factor to account for the occurrence of localised pits. For this investigation, a localised pitting factor of $\alpha_{pit} = 5$ is used based on the discussion in section 2.5.5.

3.9.2 Residual reinforcement capacity

After the gravimetric study on the reinforcement rods, the yield stress of the reinforcement rods are tested to determine the residual tensile capacity. This loss in tensile capacity based on the mass loss is compared to a similar study on reinforced strain hardening cement-based composite (R/SHCC). In this R/SHCC study, Paul (2015, pg 220) proposed equations 3.5 to 3.7 to determine the loss of yield force per unit area based on the mass lost per unit length of the reinforcement rod.

$$m_1 = \rho_s \cdot A_s \quad (3.5)$$

$$A_r = \frac{A_s \cdot \Delta W}{m_1} \quad (3.6)$$

$$Y_{loss} = \frac{1}{k} \cdot \sigma_y \cdot A_r \quad (3.7)$$

where Y_{loss} is the loss of yield force per unit area (kN/cm^2), A_r is the reduced reinforcement area due to corrosion (cm^2), m_1 is the mass of steel per unit length of reinforcement (g/cm), ρ_s is the density of steel ($7.86 \text{ g}/\text{cm}^3$), A_s is the cross-sectional area of the reinforcement (cm^2), ΔW is the equivalent corrosion mass loss per unit length of bar (g/cm^2) and, k is an experimental factor depending on the specimen

3.10 Reinforcement Tensile Test

age, duration of the corrosion process and specimen scenario. For the study in R/SHCC, Paul (2015) found a value of $k = 2.8$ and this is compared to the RC in this study.

After 36 weeks of accelerated corrosion testing, the corrosion mass loss per unit length (ΔW) is determined from the total equivalent gravimetric mass loss of the steel bar divided by the average anode region length (pitting length, L_{anode}). An example of determining the average pitting length is shown in figure 3.17. This pitting length is measured with a 150 mm vernier caliper. The start and end of the pitting zone is defined as the two furthest points of visually observed damaged (or discolouration) along the length of the corroded reinforcement bar. The average anode length of the 14 steel bars that were tensile tested in section 4.6 is approximately $L_{anode} = 35$ mm.

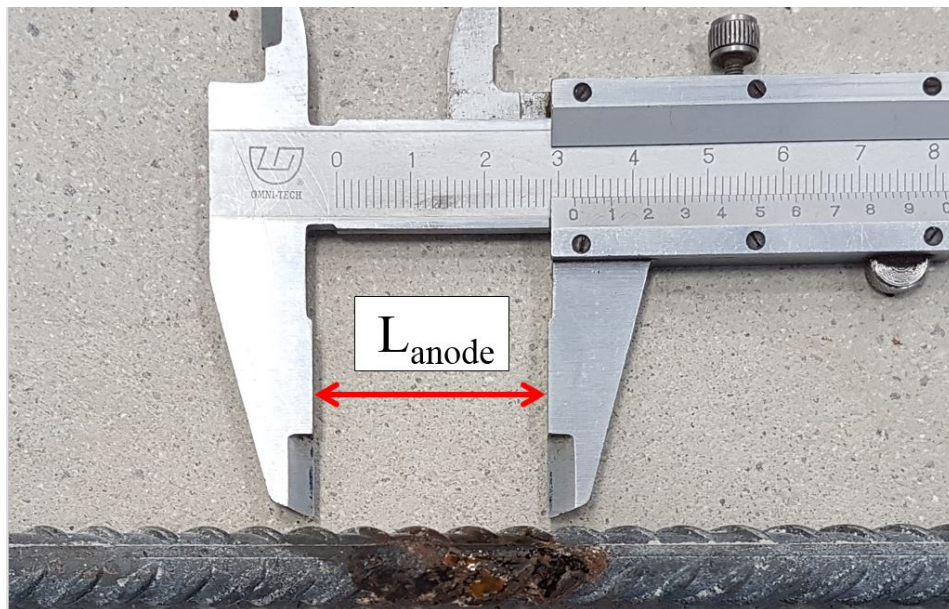


Figure 3.17: Corroded Y10 anode region length (L_{anode})

3.10 Reinforcement Tensile Test

The Y10 high tensile strength rods were selected from a batch supplied by D&E Steel, Western Cape. According to Robberts et al. (2010), the high strength steel bars have a characteristic yield strength (f_c) of 450 MPa. Tensile tests were conducted with the Zwick Z250 MTM in accordance with SANS 6892-1 (2010) to obtain the elastic modulus and actual yield strength of the reinforcement to aid in the residual tensile

3.10 Reinforcement Tensile Test

capacity predictions (described in chapter 5). The test setup for the tensile tests is shown in figure 3.18.

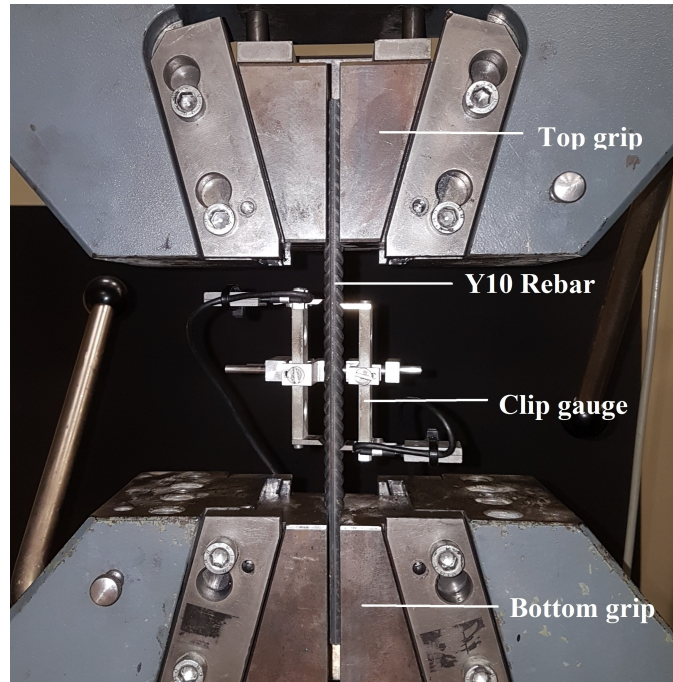


Figure 3.18: Tensile test in Zwick Z250 MTM

Four virgin Y10 reinforcement rods are tested to determine the average reference yield resistance. The specimens are cut to a length of 300 mm, and an extensometer (clip gauge) with a length of 80 mm is attached to the bar to determine the bar deformation in the gauge length. In order to ensure that the samples are securely fixed in the grips of the machine, a pre-load of 1000 N is applied. Thereafter, the samples are loaded at a constant rate of 600 N/s.

The resultant strain-stress curve is shown in figure 3.19. The elastic modulus (E_s) and yield stress (σ_y) are calculated from this curve. The displacement measured by the extensometer is divided by the original gauge length, resulting in the strain of the rod. The stress is calculated by dividing the applied force by the reinforcement cross-sectional area ($Y10_{A_s} = 78.54 \text{ mm}^2$), and the elastic modulus is then calculated from the linear portion as shown. [ASTM E8/E8M-09 \(2011\)](#) describes the offset method for determining the the yield stress, whereby the gradient of the elastic region (elastic modulus) is offset to a strain (x axis) of 0.002 mm/mm (0.2%). The yield stress

3.10 Reinforcement Tensile Test

is assumed to be the intersection between the stress-strain curve and the offset line. The yield stress and elastic modulus are given in table 3.5.

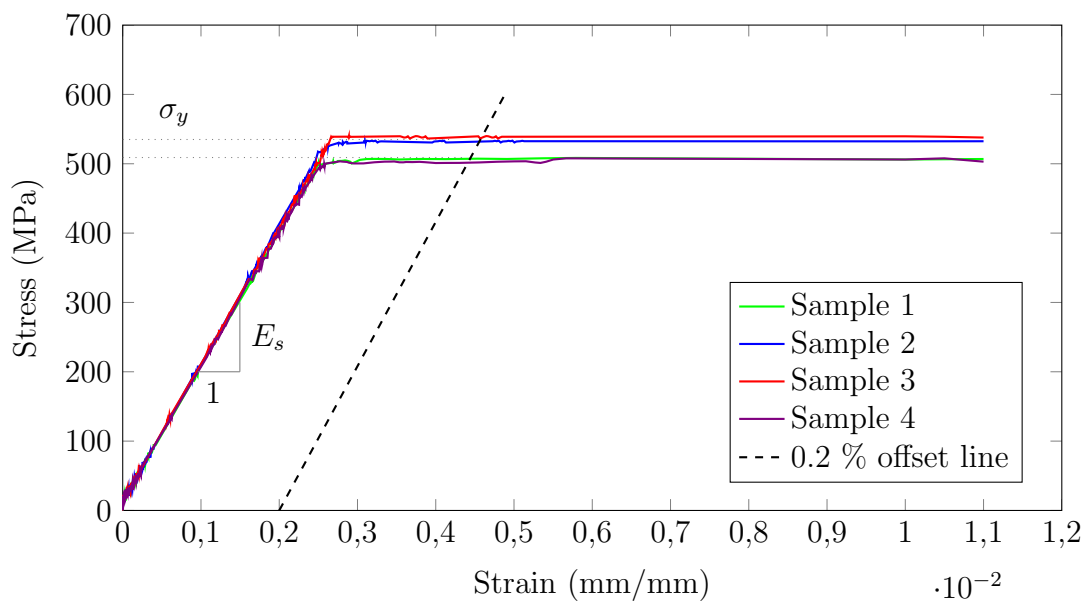


Figure 3.19: Reinforcement tensile capacity results

Table 3.5: Y10 reinforcement mechanical properties

Parameter	Sample 1	Sample 2	Sample 3	Sample 4	Average
Yield stress (MPa)	507.1	528.1	537.2	506.1	519.6
Elastic modulus (GPa)	208.0	212.9	223.5	207.6	213.0

4. Experimental results and analysis

4.1 Introduction

This chapter presents the results, analysis and discussion of the various tests outlined in chapter 3 with regard to the corrosion assessments carried out in this study.

The visual observations of the corroded reinforcement rods are discussed in this chapter, followed by a discussion of the general trends observed in corrosion rates among the 27 RC specimens. It is important to note the specimen notation used to present the experimental results shown in figure 4.1. Thereafter, correlations between the crack density and reinforcement layout are explored with regard to corrosion rate (i_{corr}). General trends in corrosion potential (E_{corr}) for the experimental period (36 weeks) are reported on, followed by a discussion on the relationship between i_{corr} and E_{corr} . The gravimetric mass loss results are compared to the theoretical equivalent electrochemical mass loss suffered by the reinforcement rods. Finally, the results, along with a discussion, of the reinforcement tensile strength between the corroded and un-corroded steel bars concludes the chapter.

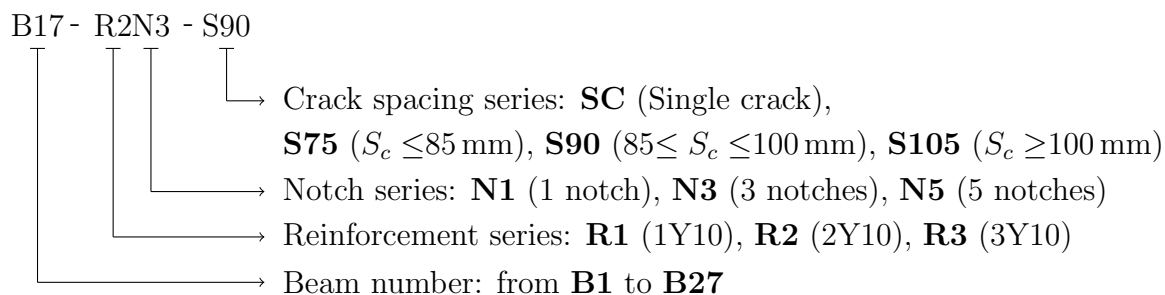


Figure 4.1: Experimental study specimen notation

4.2 General visual observations

Upon termination of the experiment, the 27 beam specimens were destructed and the corrosion damaged reinforcement rods were carefully extracted and visually inspected. No corrosion-induced cover cracking was observed in any of the three reinforcement

4.2 General visual observations

series. In all cases, the anodic area coincides with the crack location. The anodic region is defined as the corrosion damaged region in the steel rod as shown in figure 4.2.

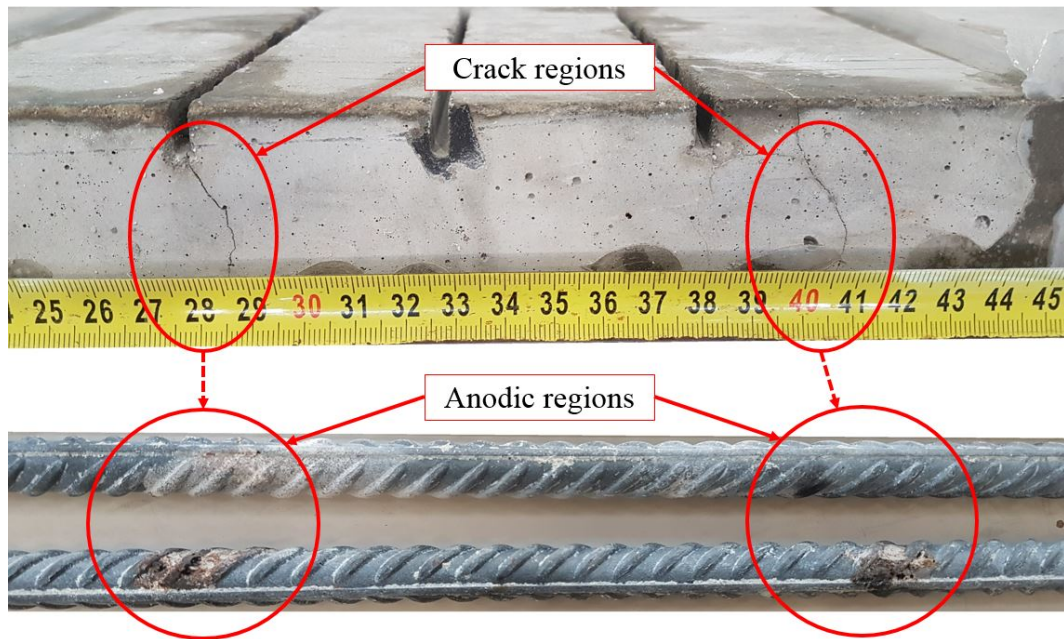


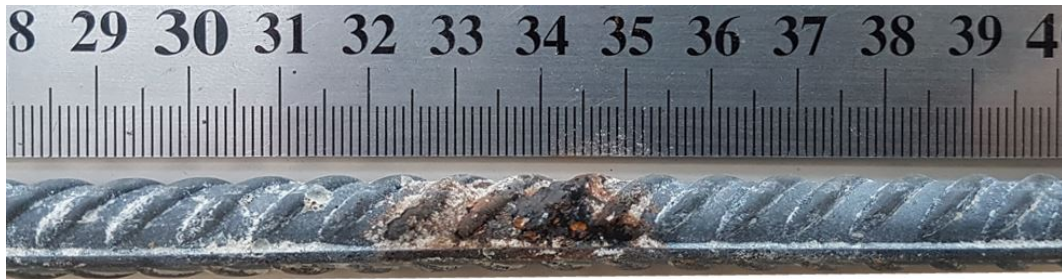
Figure 4.2: Typical crack and coinciding anodic regions

Figures 4.3 and 4.4 show the observed corrosion damage for single cracked specimens and multiple cracked specimens respectively. Whereupon figures 4.3a to 4.3c shows single, double and triple reinforced specimens respectively.

It is observed that in the case of the single cracked specimens (figure 4.3), the size of the anodic regions differs between the multiple reinforcement rods present of the same beam. In figure 4.3b it is evident that a single crack at 35 cm resulted in two different sized anodic regions. Figure 4.3c further supports this observation as the three reinforcement rods have significantly different anode region sizes. This observation is explained by:

- (i) Inconsistent crack geometry at reinforcement level. With certain parts of the crack better accommodating the corrosion process and build-up of corrosion products. This is due to the irregular nature of the formation of the crack void width along the length of the crack. Different crack widths at reinforcement level will also inhibit or facilitate the flow of Cl^- , O_2 and H_2O .

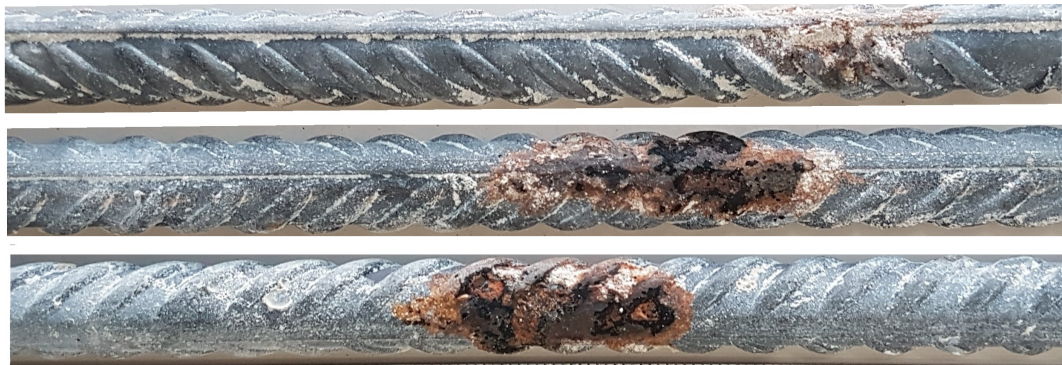
4.2 General visual observations



(a) R1 - single crack



(b) R2 - single crack



(c) R3 - single crack

Figure 4.3: Typical single crack specimens prior to cleaning with *HCl*

- (ii) It is postulated in section 2.5.6 that the “less” actively corroding bar is aiding the more actively corroding bar with electrons.

Another trend observed in specimens with multiple cracks (figure 4.4a) is that one of the crack’s anodic region’s surface area is generally larger than the second crack’s anodic region’s surface area. It was expected that the anodic regions would be similarly sized between the different steel rods that the crack crosses. However, this is not the case. This trend is also observed on specimens containing multiple reinforcement rods, where the one anodic region is larger than the other. A typical example of this trend is shown in figure 4.4b, where the second reinforcement rod has a larger anode region than the first reinforcement rod of the same beam.

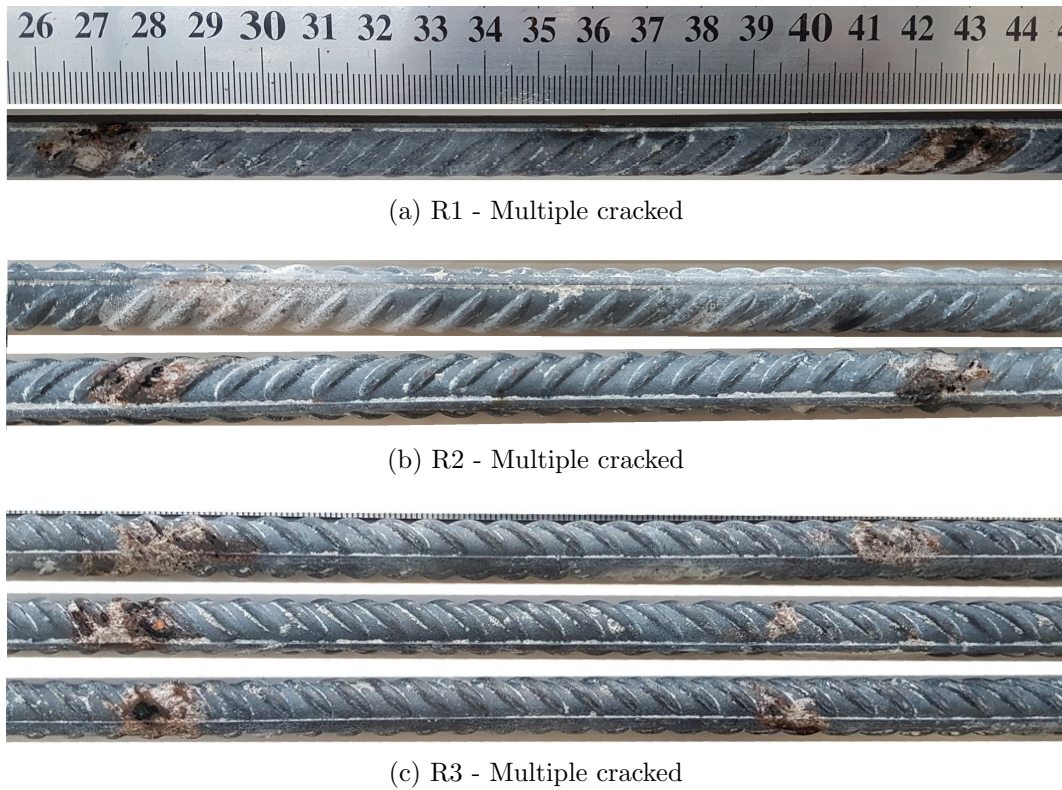


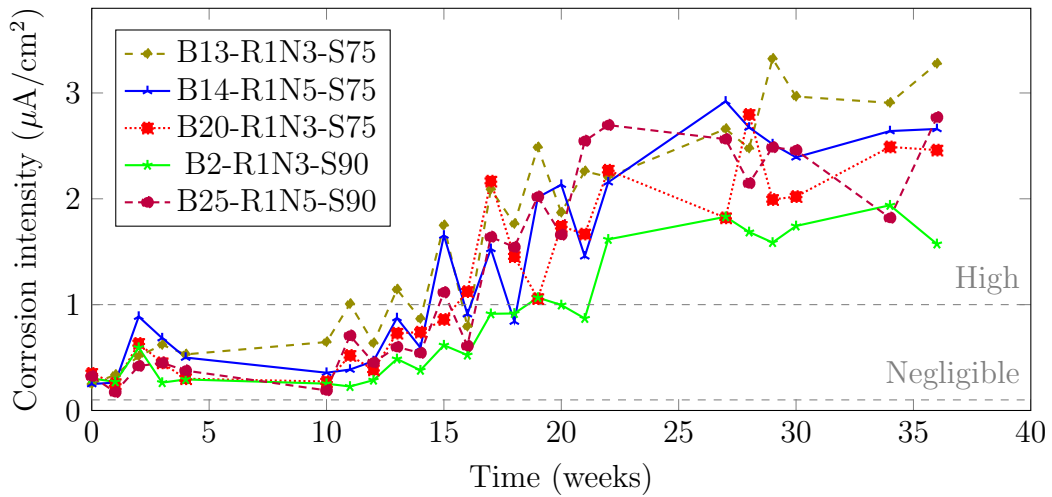
Figure 4.4: Typical multiple cracked specimens prior to cleaning with HCl

4.3 Corrosion rate results

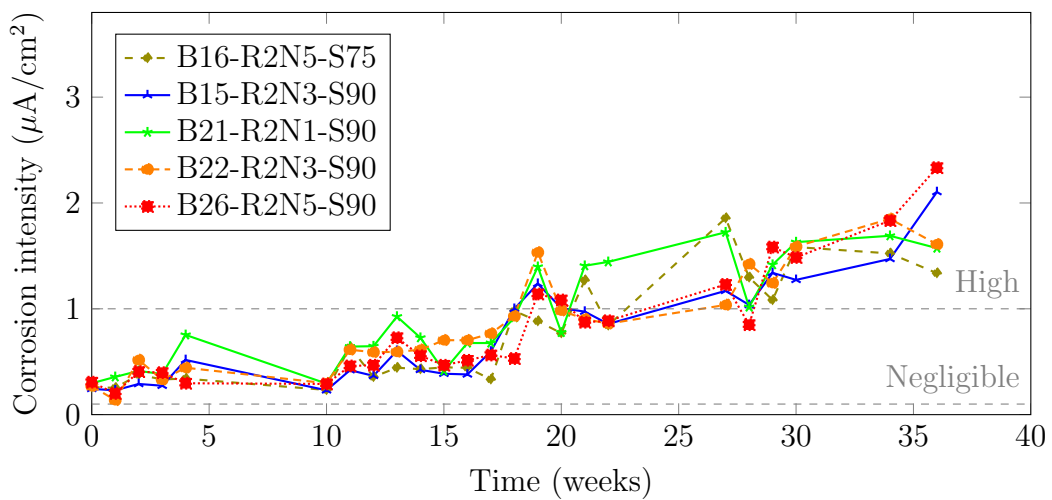
4.3.1 General overview of corrosion rate results

The time-development trends for the corrosion rate of the 27 beam specimens are shown in figures 4.5 and 4.6. As mentioned, each i_{corr} point resembles the 3-point average of corrosion rate readings taken in the pattern shown in figure 3.15. The corrosion rate of the 27 specimens was monitored for 36 weeks. The reinforcement configurations for R1, R2 and R3 series are shown together with the SC, S75, S90 and S105 crack spacing series.

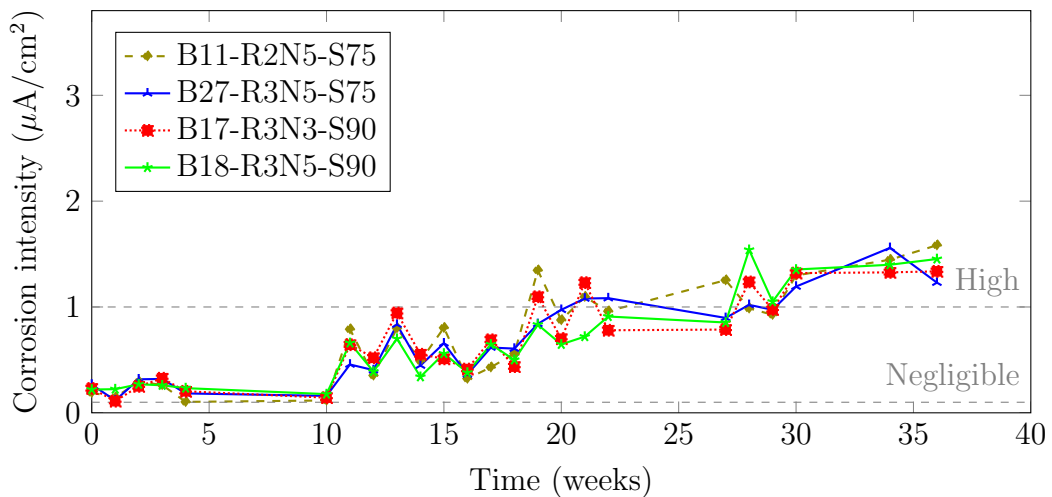
4.3 Corrosion rate results



(a) R1-S75 and R1-S90 series



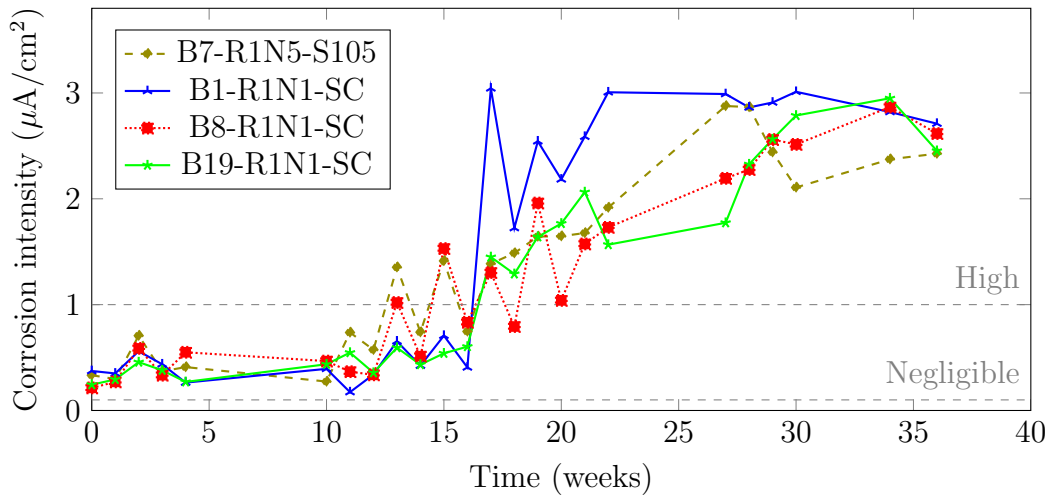
(b) R2-S75 and R2-S90 series



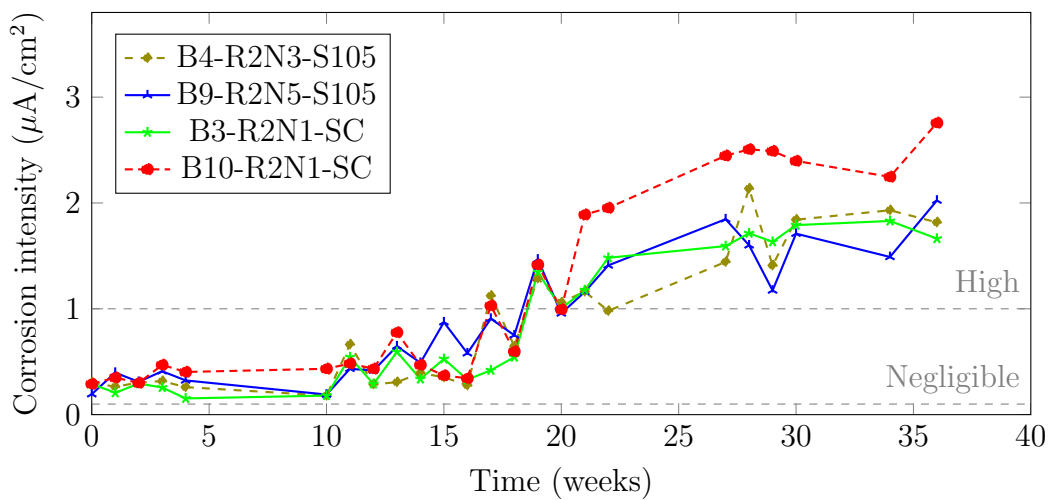
(c) R3-S75 and R3-S90 series

Figure 4.5: Typical corrosion rate time-development graphs

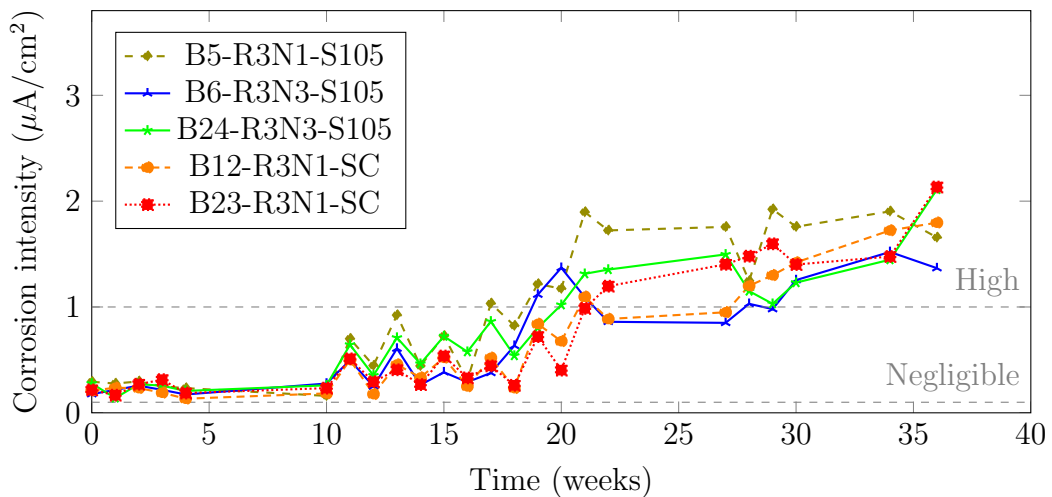
4.3 Corrosion rate results



(a) R1-S105 and R1-SC series



(b) R2-S105 and R2-SC series



(c) R3-S105 and R3-SC series

Figure 4.6: Typical corrosion rate time-development graphs

4.3 Corrosion rate results

From figures 4.5 and 4.6, the following general trends are identified in the corrosion rate readings taken during the experimental period:

- (i) The sudden rise and fall between week 10 and 20 indicate the sensitivity of the i_{corr} readings to the saturation of the concrete. Recall from section 2.2 that a higher saturation leads to an increase in the conductivity of the concrete. A sudden rising rate typically corresponds to the measurement taken 1 day after the end of the ponding cycle (concrete still moist, 1 day of air drying), while the dip that follows corresponds to the measurement taken 1 day before the next ponding cycle (concrete dried out, 8 days of air drying). Refer to figure 3.16 for the corrosion measuring schedule between ponding cycles.
- (ii) Active corrosion was achieved by all of the specimens soon after the initial ponding cycle. Up until week 10, a low level of corrosion state was achieved.
- (iii) At week 12, the specimens were unloaded and re-loaded in the loading rig to prevent autogenous healing of the cracks. The re-loading of the specimens to a w_c of 0.4 mm had an increasing effect on the corrosion rates on all of the specimens. This re-loading may serve to re-activate self-healed cracks, widen the cracks, increase the loading level or a combination of all of the above (Otieno et al. 2008). From week 12 onwards, the corrosion rates increased for all three rebar series, but increased more rapidly for the R1 series.
- (iv) At week 20, all of the R1 series specimens recorded a high level of corrosion ($i_{corr} \geq 1.0 \mu\text{A}/\text{cm}^2$). In contrast, all R2 series only surpassed the $1.0 \mu\text{A}/\text{cm}^2$ mark after 27 weeks and the R3 series remained the lowest throughout, only exceeding the high corrosion classification after 30 weeks. Refer to table 2.6 for the classification of corrosion rates.

4.3.2 Effect of crack density on corrosion rate

The three-point moving average corrosion rate of the three reinforcement layouts between the four different crack spacings is shown in figure 4.7. The single cracked specimens (SC series), are compared to the multiple cracked specimens in the series S75, S90 and S105.

4.3 Corrosion rate results

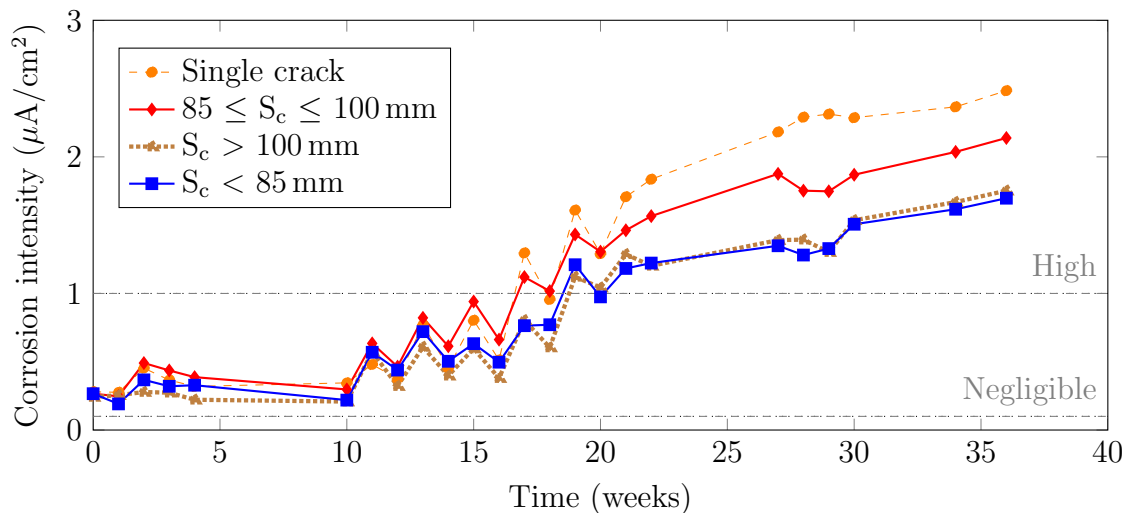


Figure 4.7: Average corrosion intensity between different crack spacings

Among the different crack spacings, the single cracked specimens obtained the highest corrosion rate for most of the test duration, while the specimens with crack spacings less than 85 mm achieved the lowest corrosion rate. This result can be explained by looking at the chemical processes present at the reinforcement level from an electrochemical point of view. As mentioned in chapter 2, the anodic region typically forms at the exposed reinforcement rod location (at the crack), while the cathodic reactions take place some distance from the anodic regions. This is labelled as “A” and “C” in figure 4.8 respectively. The anodic and cathodic reactions, are defined in equations 2.1 and 2.2 respectively.

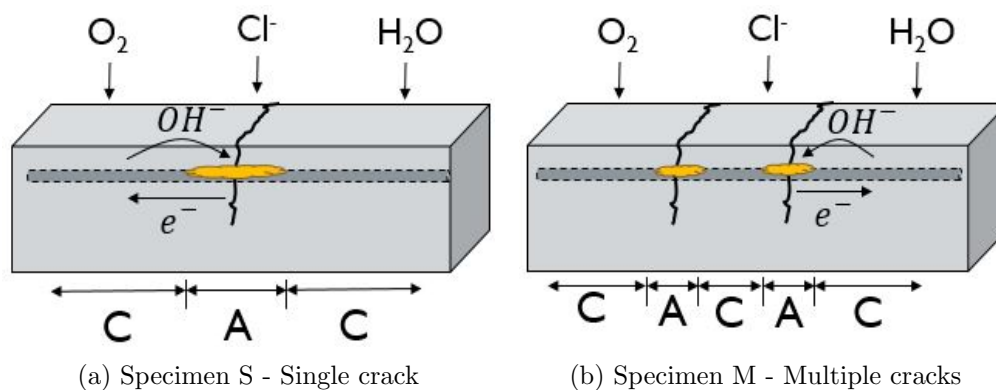


Figure 4.8: Schematic of anode to cathode ratio

Consider the schematic shown in figure 4.8, which shows concrete specimen S with a

4.3 Corrosion rate results

single crack, and specimen M with multiple cracks (figures 4.8a and 4.8b respectively). In comparison to specimen M, specimen S has a smaller anode to cathode ratio. Therefore, the closer the cracks are to each other, the larger the resulting anode to cathode ratio. The relatively smaller anode to cathode ratio of specimen S has better access to hydroxyl ions and more space to develop corrosion processes and products when compared to specimen M. It is clear from figure 4.7 that the single cracked specimens suffered the highest corrosion rate, while the multiple cracked series recorded the lowest corrosion rates in this investigation. This observation supports the schematic presented in figure 4.8.

4.3.3 Effect of reinforcement density on corrosion rate

From the general corrosion rate trends discussed in section 4.3.1, the average corrosion rates for each of the three reinforcement layouts is shown in figure 4.9.

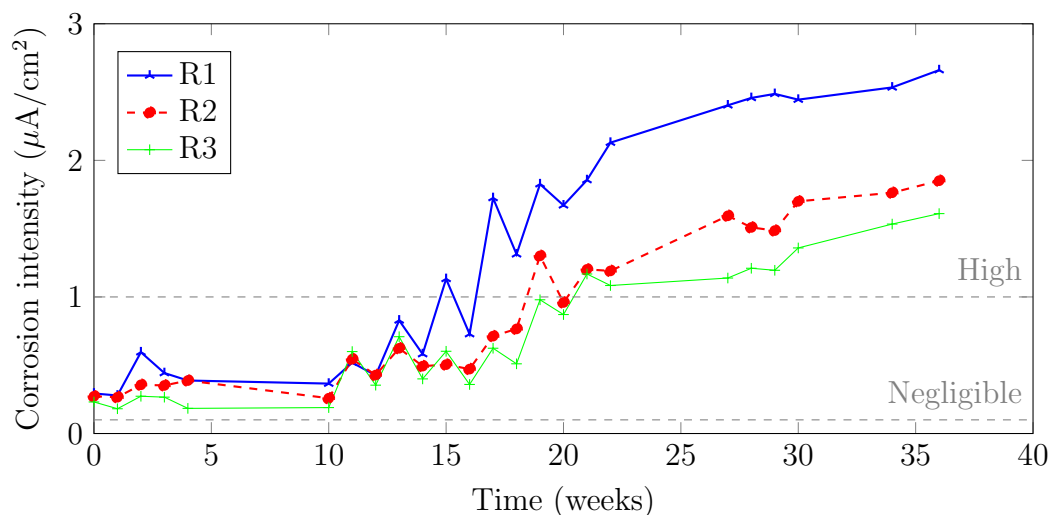


Figure 4.9: Average corrosion intensity for different reinforcement layouts

Two possible explanations for the observation of different corrosion rates between the three reinforcement layouts that are shown in figure 4.9 are given:

- (i) A difference in anode to cathode ratios between the three reinforcement layouts. This is similar to the observation made for crack spacings where there is a reduced space for corrosion products to form. In other words, a specimen with more reinforcement rods present, has larger anode to cathode ratio between the reinforcement rods. Figure 4.10 schematically shows this concept.

4.3 Corrosion rate results

- (ii) The steel-stress level of the single reinforcement rods is higher than that of the double or triple rebar configurations. This is discussed in more detail in section 5.2, but as Blagojević (2015) pointed out, the steel-stress level may have an influence on the corrosion rate. R1 required a lower pre-cracking force to reach the same crack width as the R3 specimens (table 3.3 and figure 3.8). This is verified analytically in chapter 5.

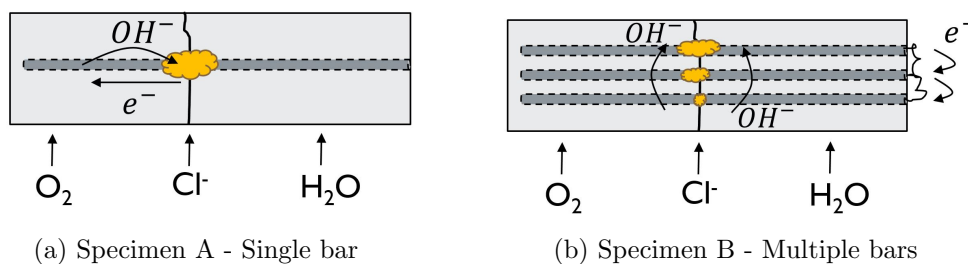


Figure 4.10: Schematic of anode to cathode ratio in multiple reinforcement beams

The anode region formed at the reinforcement level is depicted as an orange cloud above the reinforcement rod in the picture. Differently sized anode regions can be seen in figure 4.3. This result supports the first hypothesis of figure 4.10 as figure 4.9 clearly shows that a single reinforcement rod suffered the highest corrosion rate. The R3 series with the highest reinforcement density recorded the lowest corrosion rate further supporting this concept. With regard to steel stress, this is analytically verified and discussed in section 5.2.

4.3.4 Correlation between crack density and reinforcement density

From the results of sections 4.3.2 and 4.3.3, a comparison of corrosion rates as a function of crack spacing is shown in figures 4.11 and 4.12.

4.3 Corrosion rate results

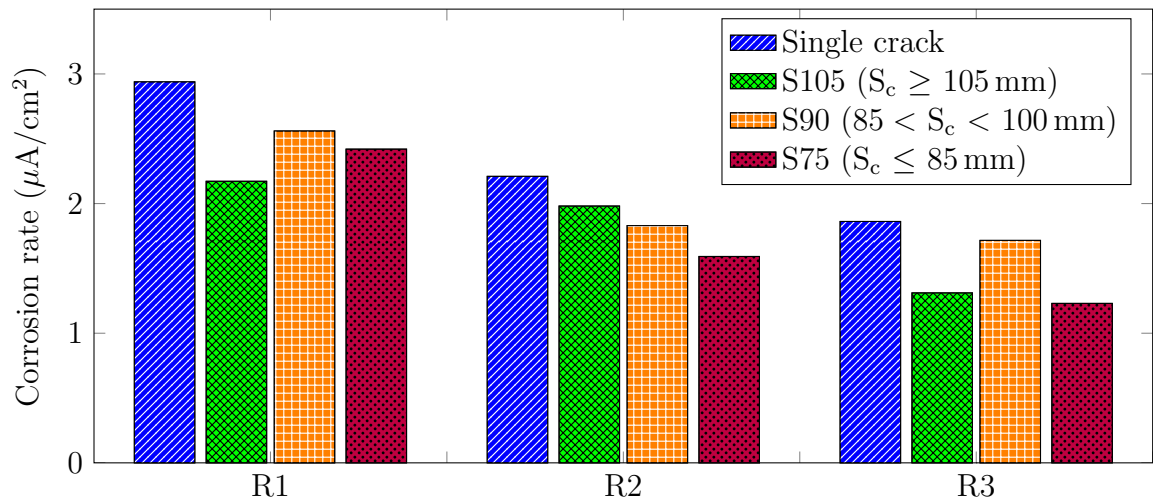


Figure 4.11: Average corrosion rates after 36 weeks

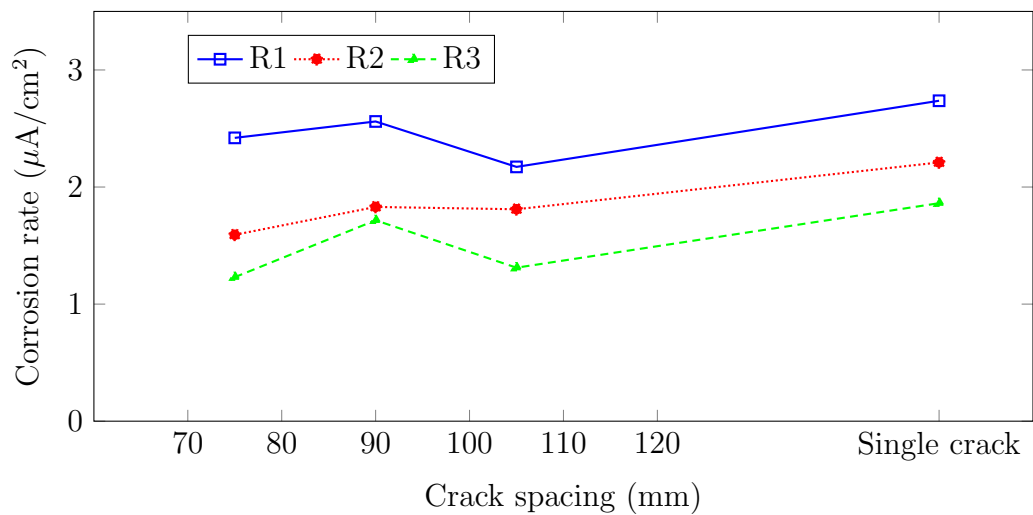


Figure 4.12: Correlation between crack spacing and reinforcement layout

The hypothesis that a complex electrochemical relationship exists between the different reinforcement bars and crack spacings is supported by the results in corrosion rates. The three reinforcement densities (R1, R2 and R3), combined with the four crack spacing series (S75, S90, S105 and SC) gives rise to the postulation that the anode to cathode ratio effects the corrosion rate. An increase in reinforcement density leads to a decrease in corrosion rate, while a decrease in crack spacing also leads to a decrease in corrosion rate.

4.4 Corrosion potential results

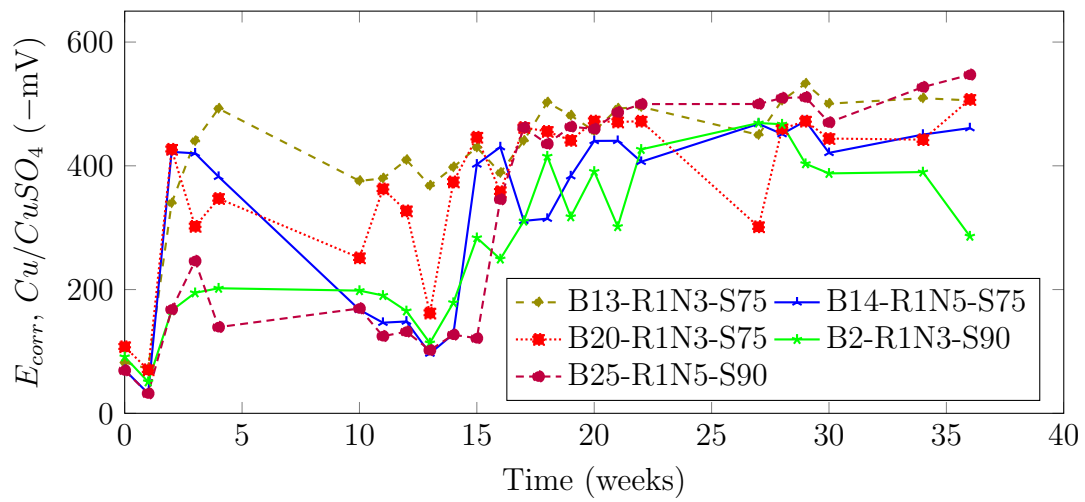
As a general overview, the single reinforcement series was susceptible to the highest corrosion rate for each crack spacing. Similarly, the highest reinforcement ratio suffered the lowest corrosion rate for each crack spacing respectively. The corrosion rates increased based on the following trend: R3-S75,S105,S90,SC → R2-S75,S90,S105,SC → R1-S105,S75,S90,SC. Apart from an intricate relationship between anode and cathode regions, the influence on the corrosion rate is affected more by an increase in reinforcement density rather than crack spacing. Furthermore, a single crack suffered a higher corrosion rate than multiple cracks on a RC member.

4.4 Corrosion potential results

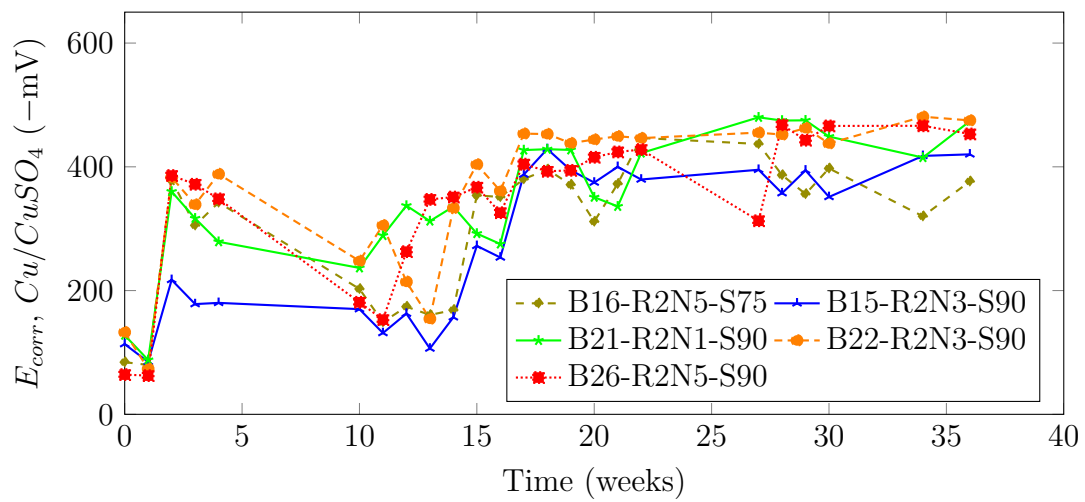
4.4.1 General overview of corrosion potential results

The time-development trends of the corrosion potential (E_{corr}) measurements obtained during the experimental period are shown in figure 4.13. This general overview shows the trends between the different crack spacings and reinforcement layouts. According to ASTM (2015), a corrosion potential of less (more negative) than -350 mV has a high probability of active corrosion, and less than -500 mV has a severe risk of corrosion (refer to table 2.7). It should be noted that the corrosion potential shown in figure 4.13 is measured against a copper-copper sulphate (Cu/CuSO_4) reference electrode and that the vertical axis is the negative of the corrosion potential ($-\text{mV}$).

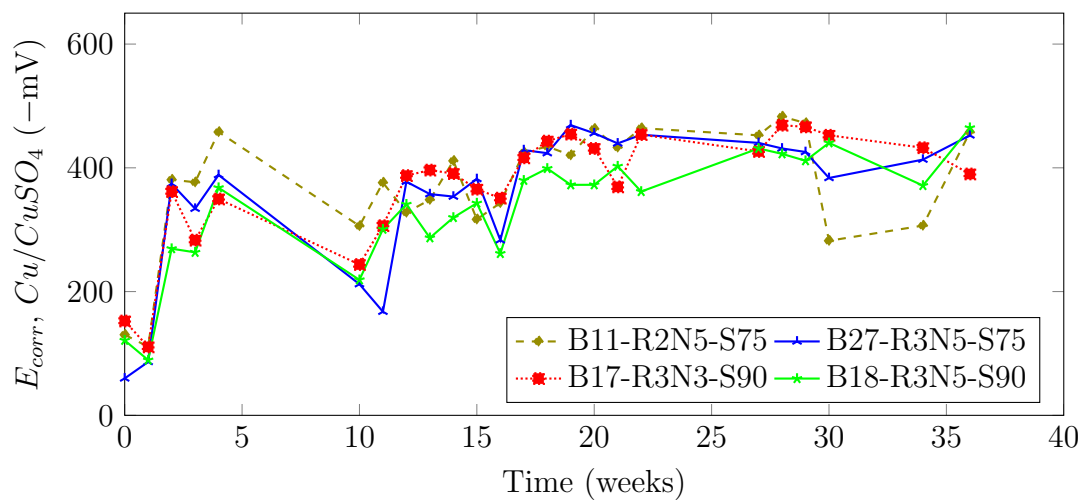
4.4 Corrosion potential results



(a) R1-S75 and R1-S90 series



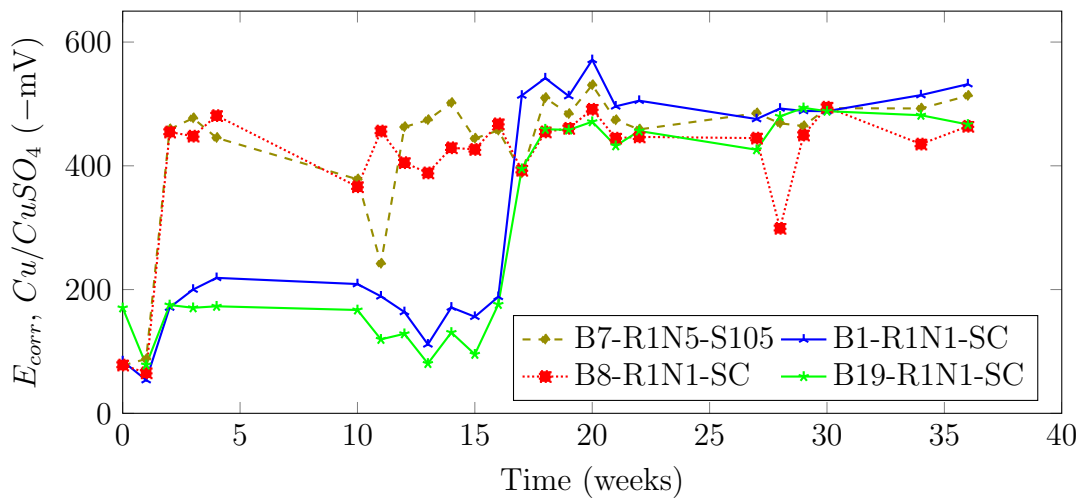
(b) R2-S75 and R2-S90 series



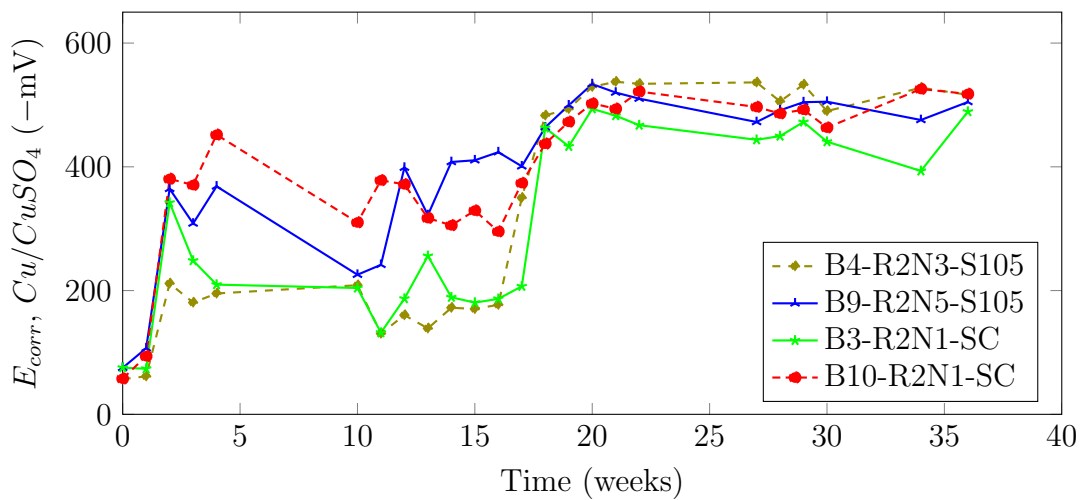
(c) R3-S75 and R3-S90 series

Figure 4.13: Typical corrosion potential time-development graphs

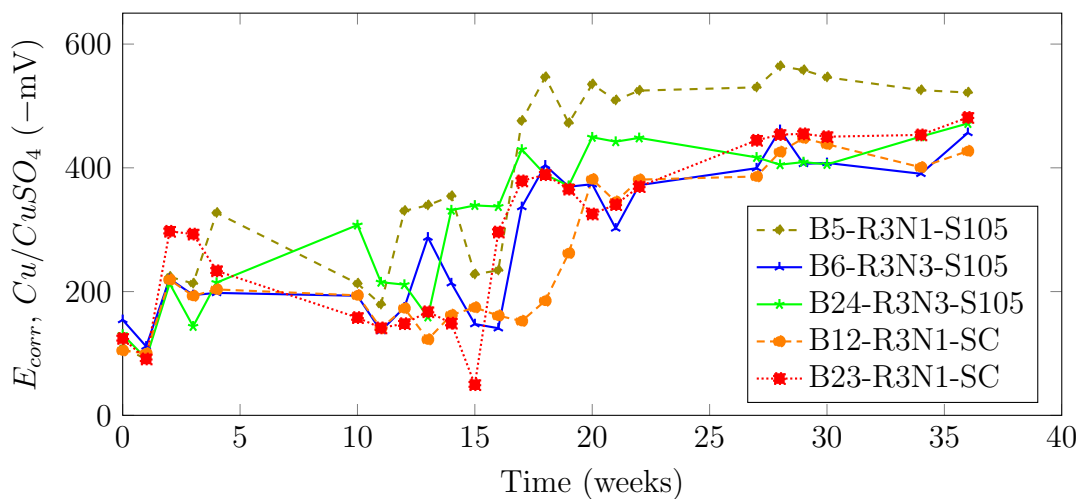
4.4 Corrosion potential results



(a) R1-S105 and R1-SC series



(b) R2-S105 and R2-SC series



(c) R3-S105 and R3-SC series

Figure 4.14: Typical corrosion potential time-development graphs

4.4 Corrosion potential results

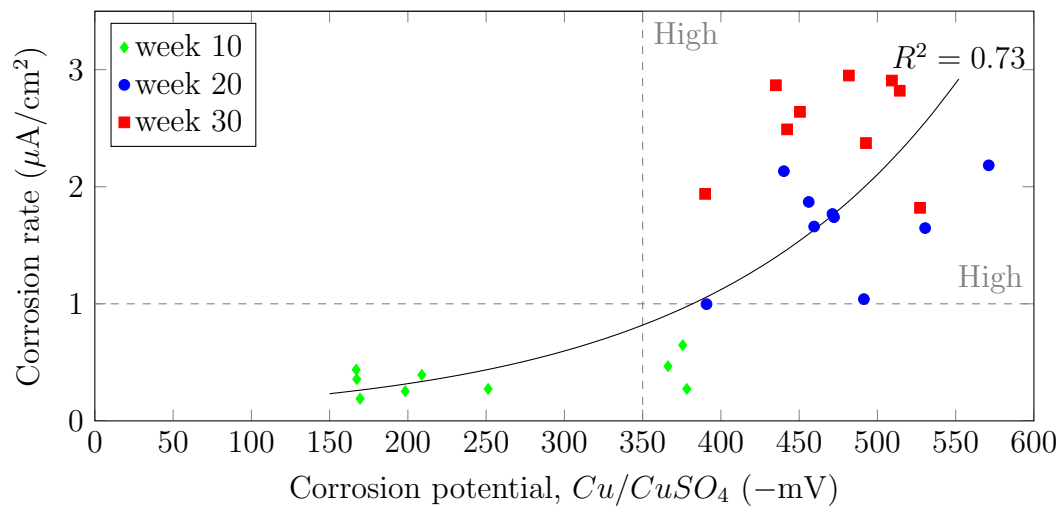
It is important to note that the corrosion potential indicates the corrosion condition of the reinforcement in the concrete (Broomfield 2002). Therefore, specimens with the same concrete properties (w/b ratio, binder type, crack width and cover depth) should have similar corrosion potential trends as the corrosion rate trends presented in the section 4.3. From figures 4.13 and 4.14, the following general trends are noted in the corrosion potential measurements taken during the experimental period:

- (i) Corrosion potential has an initial spike after the first ponding in week 1, after which it remains relatively consistent at an average of -350 mV. Recall from section 2.3 that the reaction of the penetrating chlorides reduces the ferrous ion concentration by lowering the pH of the concrete and breaking down the passive film (depassivation). This decrease in ferrous ion concentration leads to a reduction in corrosion potential. According to the ASTM (2015), a corrosion potential ≤ -350 mV vs. the $Cu/CuSO_4$ demonstrates a 90% certainty of active corrosion. At week 15, after the third reopening of cracks, the corrosion potential for the majority of the specimens decreased to a more severe risk level (-500 mV).
- (ii) For most of the specimens, from week 5 to week 15, the corrosion potential increased. This could indicate that the specimens may have been susceptible to autogenous crack healing. This hypothesis is supported with the reopening of cracks at week 12, where the corrosion potentials begin to decrease again. This occurrence is similar to the trend in corrosion rates after the re-loading of the specimens, as mentioned in section 4.3.1.

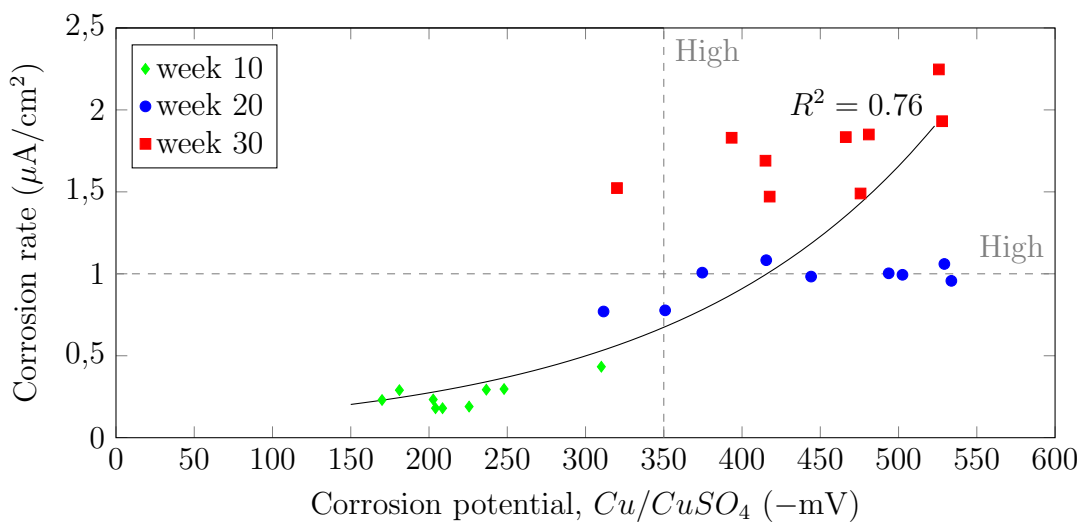
4.4.2 Relationship between corrosion potential and corrosion rate

Figure 4.15 shows the relationship between the average corrosion potential and average corrosion rate for the specimen series R1, R2 and R3. The exponential trend lines shown in these figures indicate that there is considered to be a correlation for the R1, R2 and R3 series.

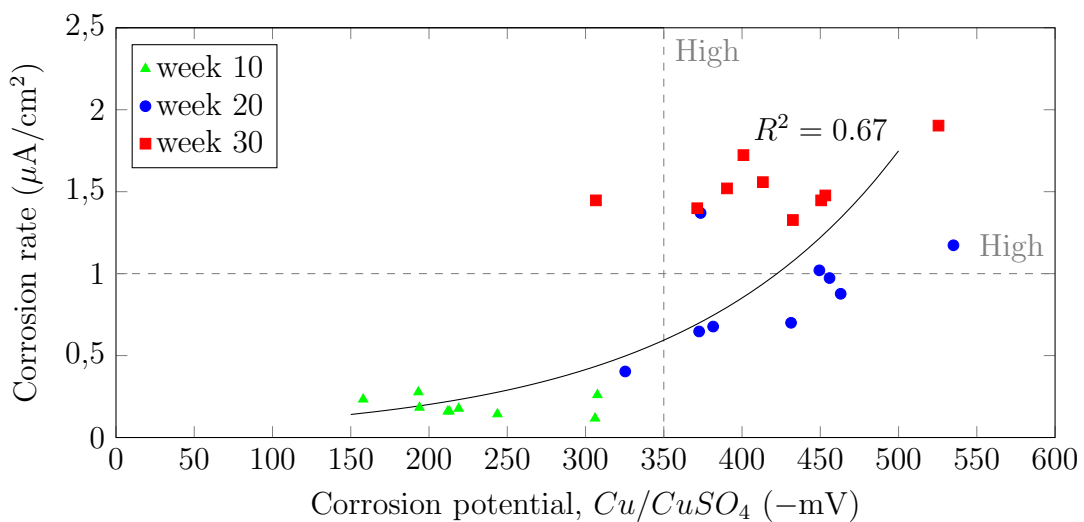
4.4 Corrosion potential results



(a) R1



(b) R2



(c) R3

Figure 4.15: Corrosion rate vs. corrosion potential

From figure 4.15 it is noted that the corrosion potential needs to be supplemented with other corrosion assessment techniques to provide an accurate prediction of the state of corrosion. As mentioned section 3.8, this study implemented the use of the galvanostatic corrosion assessment technique to convert the corrosion rate into an equivalent mass loss. Both the corrosion rate and corrosion potential depend on the ease of ion movement in the concrete, which is governed by the concrete resistivity (chapter 2). Concrete resistivity is, therefore, seen as the link between the corrosion rate and corrosion potential (Otieno et al. 2008, pg.111). Figure 4.16 shows the comparison between the average i_{corr} and the average E_{corr} for every 5th week of corrosion assessment. A gradual increase for both the corrosion rate and potential is observed over the course of this investigation.

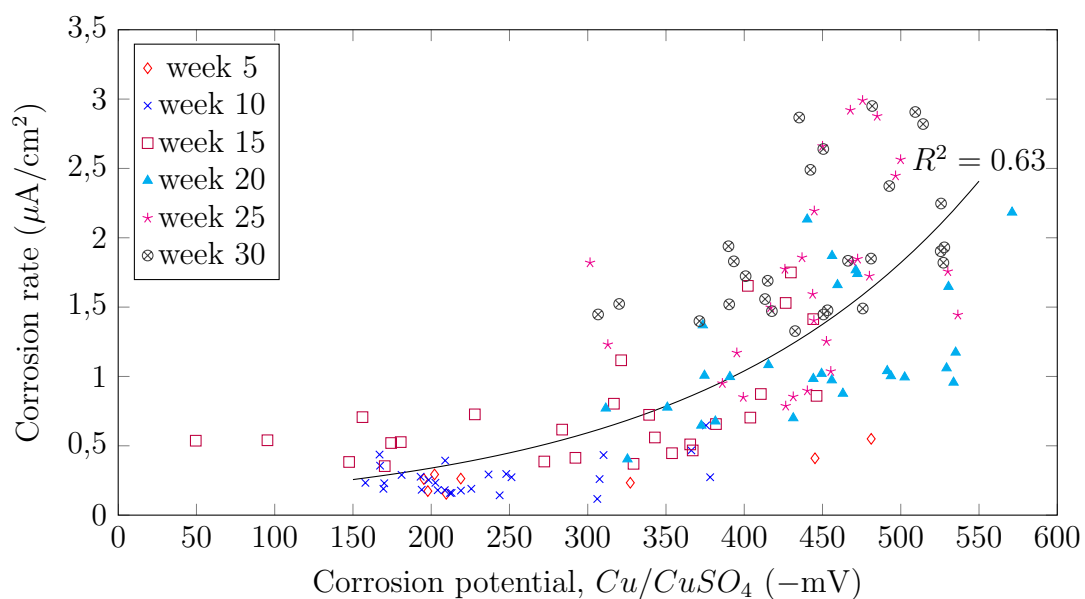


Figure 4.16: Average i_{corr} vs. E_{corr}

4.5 Mass loss results

4.5.1 Electrochemical mass loss

Typical time-development trends for theoretical electrochemical cumulative mass loss during the experimental period are calculated according to equation 2.17. The i_{corr} value is multiplied by the time (t) between each measurement and a conservative pitting factor (α_{pit}) of 5 is used, as discussed in section 2.5.5. The cumulative mass

loss time-development curve for the reinforcement layouts and crack spacings is shown in figures 4.17 and 4.18 respectively.

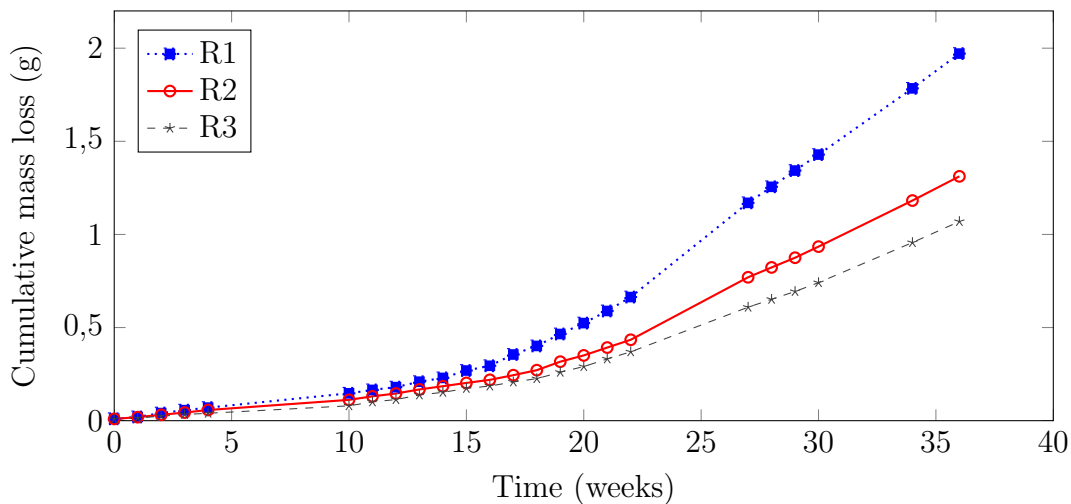


Figure 4.17: Average reinforcement layout electrochemical mass loss over time

Figure 4.17 is the equivalent mass loss for the corrosion rates reported in figure 4.9, where the following trends based on the predicted electrochemical mass loss is noted:

- (i) As expected, the specimens containing a single reinforcement rod theoretically suffered greater mass loss than both the double and triple reinforcement layouts. Upon termination of the experiment, the R1 is expected to have lost approximately twice the mass of the R3 series specimens.
- (ii) The triple reinforcement series (R3) experienced the lowest corrosion rate throughout the experimental period, and consequently, the smallest calculated mass loss.
- (iii) After week 25, the mass loss gradient for R1 increased rapidly in comparison to the series R2 and R3.
- (iv) Upon termination of the experiment, the mass loss rate of the R1 series is 1 g every 10 weeks.

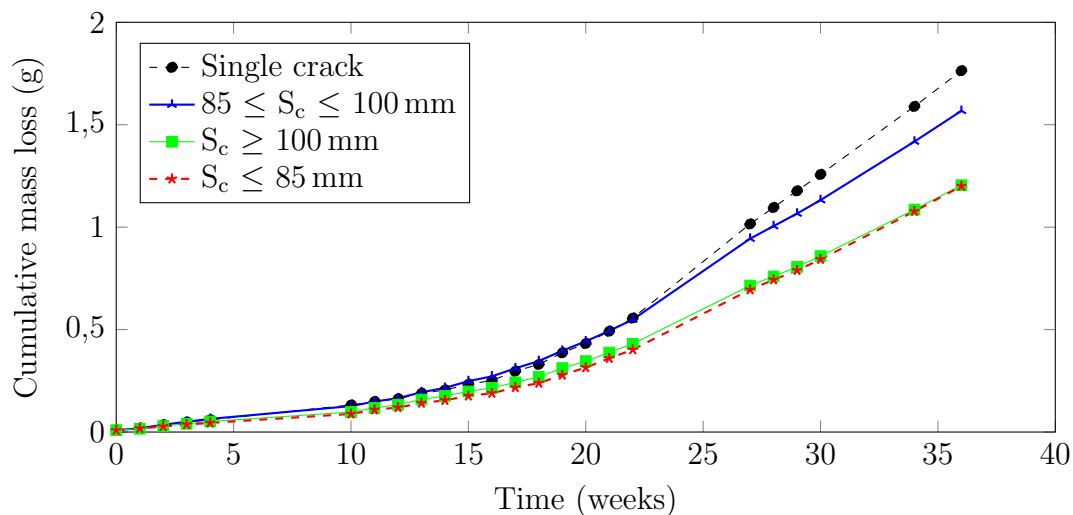


Figure 4.18: Average crack spacing electrochemical mass loss over time

For the second time-development mass loss curve, figure 4.18 is the equivalent mass loss over time for figure 4.7 that compares the calculated mass loss suffered between the crack spacings. The following is noted with regard to the average crack spacing mass loss:

- (i) The single cracked specimens (SC) suffered the highest mass loss among the different crack spacings. Upon termination of the experiment, the average single cracked specimens theoretically lost approximately 1.5 times more mass than the specimens with cracks spaced less than 85 mm.
- (ii) For the first 20 weeks of the experiment, there is no clear distinction between the mass loss suffered by the specimens with crack spacings smaller than 85 mm and the single cracked specimens. Only after 25 weeks the mass loss gradient of the SC series starts to increase at a higher rate.
- (iii) Specimen series S90 and S105 show a similar mass loss trend. This is attributed to the similar corrosion rates of the beams with these crack spacings.
- (iv) Upon termination of the experiment, the mass loss rate of the SC series is 1 g every 13 weeks.

4.5.2 Gravimetric mass loss

The mass loss procedure followed in this investigation is described in more detail in section 3.9.1. The resultant mass loss suffered by the reinforcement rods through the duration of the experiment is shown in figure 4.19.

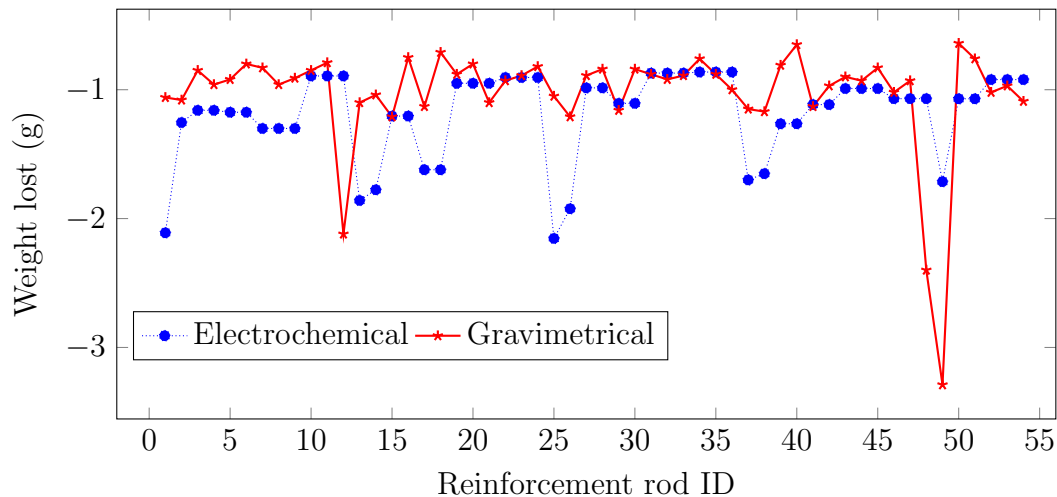


Figure 4.19: Initial weight vs. final weight

The actual mass loss measured in the gravimetric study is then compared to the calculated mass loss suffered through the use of electrochemical formations as described in chapter 3. The comparison between the theoretical and the actual mass loss is discussed in section 4.5.3.

4.5.3 Relationship between electrochemical and gravimetric mass loss

The relationship between the electrochemically predicted (Faraday's law, equation 2.16) and the actual gravimetric mass loss is now explored. For each of the 27 beam specimens, the average measured gravimetric mass loss is shown with the predicted electrochemical mass loss and grouped according to the four crack spacings as shown in figure 4.20. The dashed and dotted line for each crack series represent the group average gravimetric and electrochemical mass loss respectively.

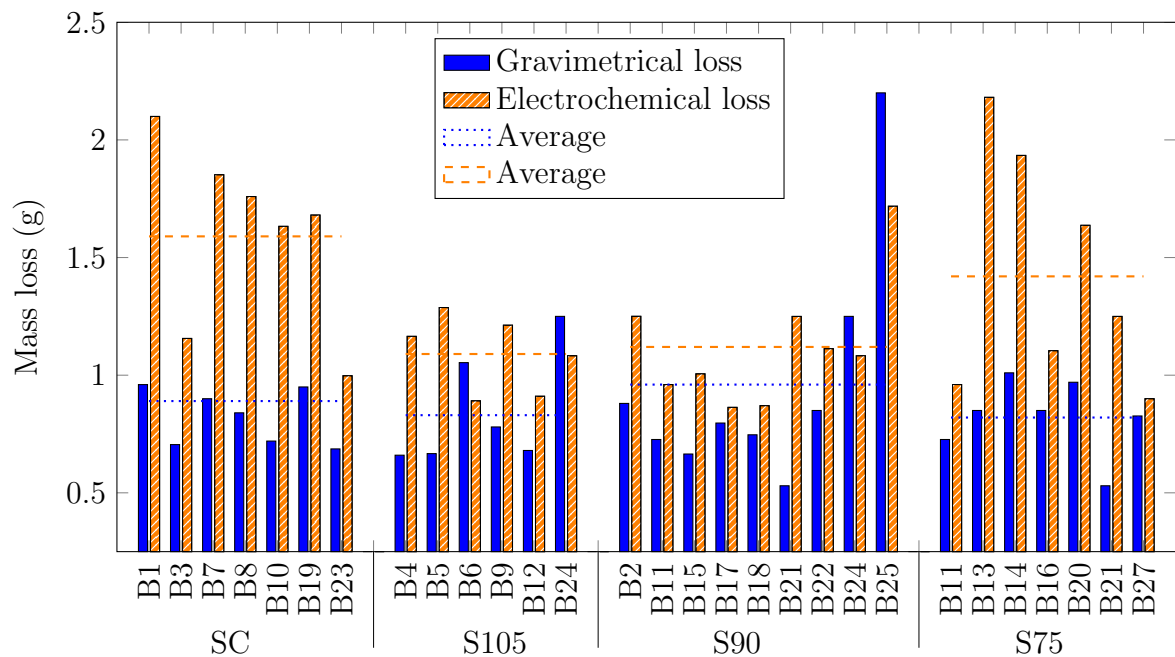


Figure 4.20: Crack spacing vs. mass loss

From figure 4.20 the following is observed:

- (i) As expected, the SC average electrochemical mass loss is the highest among the crack spacings, while the S75 series is the lowest.
- (ii) Crack spacing series S90 has the highest actual mass loss among the four crack spacings. Beam specimen B25 has the highest actual mass loss of 2.3 g. If B25 was treated as an outlier to the results, as it showed much higher mass loss on average to the other specimens (approximately 2.5 times more than the average specimen), the S90 series would have the lowest actual mass loss. This correlates better with the predicted electrochemical mass loss.
- (iii) For all four crack spacings, the difference between the actual mass loss and the predicted mass loss is approximately 0.56 g (26%) for a pitting factor equal to 5. As mentioned in section 3.9.1, the result of the electrochemical mass loss is dependent on the assumed pitting factor (α_{pit}). Andrade et al. (1997) recommend a conservative pitting factor in the range of 4 to 10. However, in recent investigations Otieno (2014, pg. 37) uses $\alpha_{pit} = 10$ for accelerated corrosion testing. If $\alpha_{pit} = 3$ is used, the difference between the actual and predicted electrochemical mass loss would be approximately 0.04 g (2%).

4.6 Reinforcement tensile capacity results

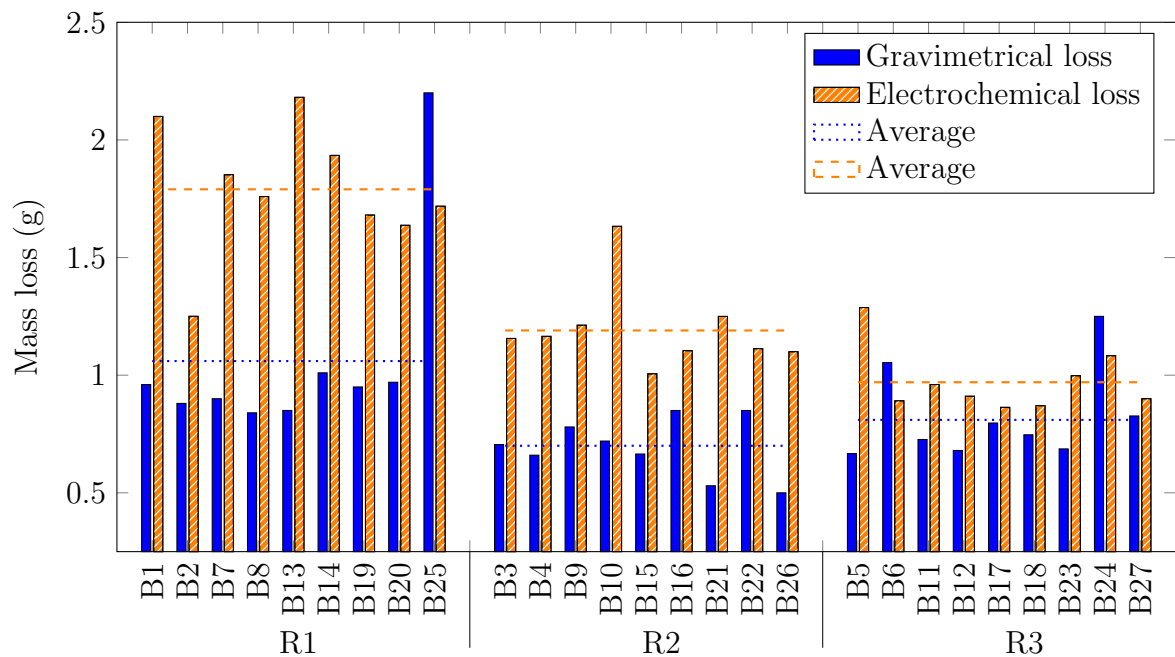


Figure 4.21: Reinforcement density vs. mass loss

For the three different reinforcement layouts, the electrochemical vs gravimetrical mass loss is shown in figure 4.21, from where the following is noted:

- (i) The R1 series had the highest expected and actual mass losses between the three layouts. This is expected as the corrosion rate from section 4.3.3 is the highest for the R1 series throughout the experiment's duration.
- (ii) Between the multiple reinforcement series R2 and R3, the later recorded the highest mass loss and the former lost the least. The R3 showed a good correlation between the electrochemical and gravimetrical mass loss (84%).

4.6 Reinforcement tensile capacity results

4.6.1 Relationship between tensile capacity and corrosion rate

After termination of the experiment, the reinforcement rods were carefully broken out of the concrete matrix and thoroughly cleaned. Fourteen bars were selected from the specimens for tensile tests. The bars were selected based on the condition of

4.6 Reinforcement tensile capacity results

either the highest corrosion rate, and/or suffered the highest mass loss and/or was visually observed to have undergone the most corrosion damage in the respective series. Generally, the bar that had suffered the highest mass loss was usually the same bar found to have had recorded the highest corrosion rate and visual damage to the surface of the bar. The 14 steel bars were then tensile tested in the Zwick Z250 MTM procedure as described in section 3.10 (and complying to SANS 6892-1 (2010)). The four undamaged Y10 bars tensile yield capacity was then taken as the reference yield capacity. Figure 4.22 depicts the yield force between the undamaged (U series) bars versus the damaged corroded bars.

Recall from section 4.2 that among the R2 and R3 series beams, it was observed that one of the two/three bars generally has a larger anode region than the other bar(s) from the same beam. This observation motivates the need to test bars from the same beam to determine the difference in yield force loss between rods of the same beam.

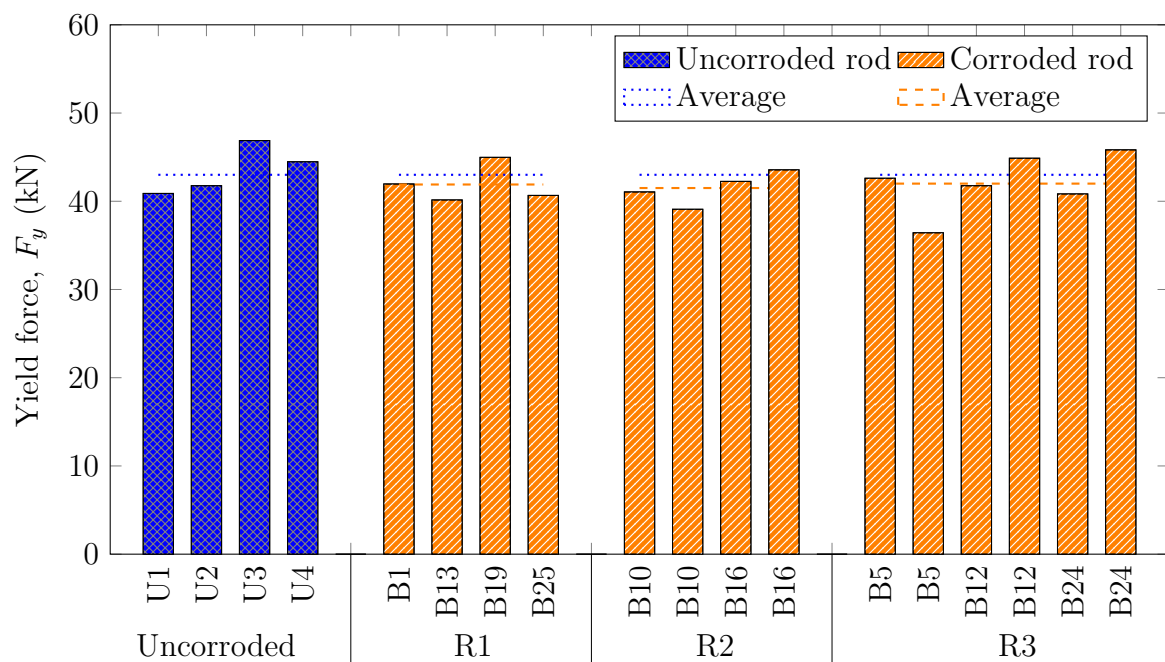


Figure 4.22: Yield force between uncorroded and corroded reinforcement bars

Taking into consideration that the sample size of the corroded bars is larger (4 un-corroded bars vs. 14 corroded), the un-corroded reinforcing bars have a higher average yield force of $F_y = 43.01$ kN in comparison to the $F_y = 41.86$ kN average of

4.6 Reinforcement tensile capacity results

the corroded rods. There is no clear distinction between the yield forces of different reinforcement configurations, 41.94 kN, 41.58 kN, 42.00 kN for the R1, R2 and R3 series respectively. However, as can be seen for series R2 and R3 with multiple rods per beam, there is in some cases a difference in yield force between rods of the same beam. For example, in the case of beam specimen B5, from where it can be seen that the second reinforcement rod reached a yield force much lower (36.4 kN) than the first B5 rod (42.6 kN, 14.5 % higher). This observation supports the hypothesis from the visual observations (section 4.2) where it is observed that one rod generally sustained more corrosion damage than the other rod(s).

Figure 4.23 shows the plot of gravimetric mass loss suffered per unit length versus the equivalent loss of yield force per unit area with respect to the average uncorroded bar F_y . The average uncorroded bar yield force, $F_y = 43$ kN, is taken as the yield force intercept at a mass loss of 0 g, and a trend line is plotted for the corroded bars to an experimental k value of 4.6. As expected, the trend line shows that an increase in mass loss leads to a reduction in yield force. This model is based on equations 3.5 to 3.7 proposed by Paul (2015, pg 220) and discussed in section 3.9.2.

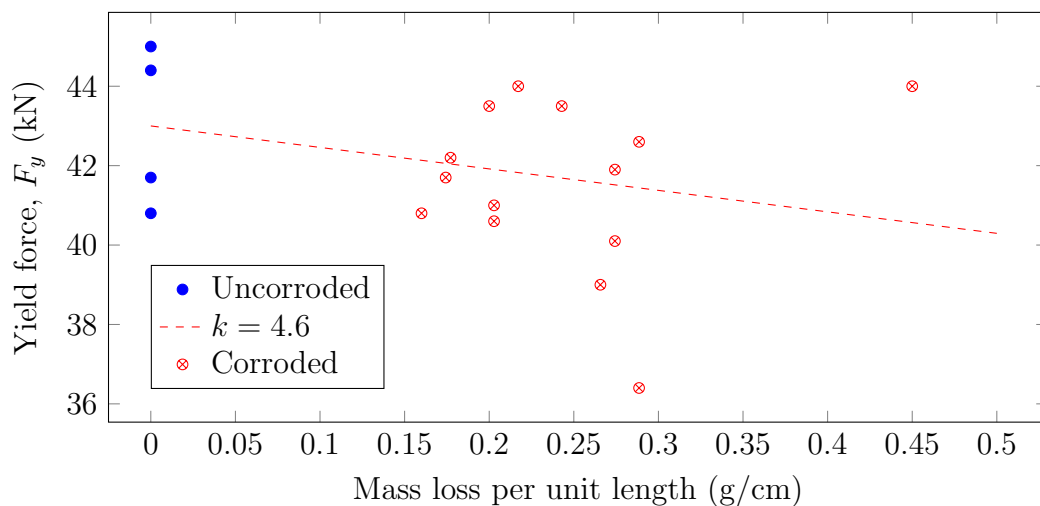


Figure 4.23: Relationship between loss of yield force and the mass loss of the steel bar

In section 3.9.2 it is shown that the average anode length was approximately 35 mm. The yield strength of the steel is 520 MPa as determined in section 3.10 and a steel density of 7.875 g/cm^3 is used in this model.

4.6 Reinforcement tensile capacity results

However, these results can be improved by:

- (i) Allowing for longer periods of accelerated corrosion testing may potentially ensure that no steel sample exceeds the yield strength as the loss is expected be greater. Therefore, ensuring that all the samples are weaker than the uncorroded bars.
- (ii) Including a larger sample size of uncorroded and corroded bars. This will remarkably improve the accuracy of both the uncorroded yield strength and the loss of yield strength in tensile tests.

This model cannot be justified by the limited set of data available in this regard. Apart from one of the reinforcement rods suffering up to 2.2 g mass loss, the majority of the rods lost approximately 1 g of mass loss over the course of 36 weeks of corrosion testing. It should therefore be noted that the experimental period was too short to show the potential loss in reinforcement yield force over the mass loss. It is expected that a longer corrosion study would indicate that the higher the mass loss suffered, consequently, the greater the loss in yield force due to a reduction in a rod cross-sectional area.

5. Towards residual service life prediction

5.1 Introduction

The accurate and reliable prediction of chloride-induced corrosion rate in RC structures is paramount to determining the remaining service life of a structure. In recent years, many research efforts have been undertaken towards the prediction of corrosion rate. Some of these selected corrosion rate prediction models is discussed in more detail in section 5.3.1. The accuracy of these prediction models and the limits to their input parameters is discussed in sections 5.3.2 and 5.3.3 respectively. This chapter includes the analytical calculations to the average reinforcement-stress levels for a given surface crack width. This is discussed in section 5.2. A relationship between the steel-stress level and the corrosion rates observed in chapter 4 is then deduced based on the concrete beams from this investigation.

A residual service life prediction is then proposed for RC beams based on the measured corrosion intensity, pitting factor and reinforcement diameter. This is discussed in section 5.3.3. Prior to the discussion towards residual service life, it is important to define the difference in corrosion units, as corrosion can be measured in corrosion intensity ($\mu\text{A}/\text{cm}^2$), mass loss ($\text{g}/\text{cm}^2 \text{ year}$) and penetration rate (mm/year). This conversion table is shown in table 5.1. The formulae for conversion between the corrosion units is discussed in chapter 2 and is based on the electrochemical mass loss law of Faraday.

Table 5.1: Conversion between corrosion units

Parameter:	Corrosion intensity	Mass loss rate	Penetration rate
Unit:	$\mu\text{A}/\text{cm}^2$	$\text{g}/\text{cm}^2 \text{ year}$	$\mu\text{m}/\text{year}$
$\mu\text{A}/\text{cm}^2$	1	$8.95 \cdot M/n$	$3.28 \cdot M/z \cdot \rho$
$\text{g}/\text{cm}^2 \text{ year}$	$0.112 \cdot n/M$	1	$2.74 \cdot \rho$
$\mu\text{m}/\text{year}$	$0.306 \cdot z \cdot \rho/M$	$0.365/\rho$	1

Taking into account that this study will only be investigating the corrosion of iron bars (F_e), where $z = 2$ (valency of iron), $M_{Fe} = 56 \text{ g}$ (molar mass of iron), $\rho = 7.85 \text{ g}/\text{cm}^3$

(density of iron), table 5.1 is converted to table 5.2.

Table 5.2: Conversion between units of corrosion for F_e

Parameter: Unit	Corrosion intensity $\mu\text{A}/\text{cm}^2$	Mass loss rate $\text{g}/\text{cm}^2 \text{ year}$	Penetration rate $\mu\text{m}/\text{year}$
$\mu\text{A}/\text{cm}^2$	1	0.365	11.6
$\text{g}/\text{cm}^2 \text{ year}$	2.74	1	21.6
$\mu\text{m}/\text{year}$	0.0862	0.046	1

5.2 Steel-stress level

5.2.1 Analytical calculation of steel-stress level

The analytical verification of crack widths and calculations of steel-stress levels in relation to the surface crack width is calculated in this section. For the concrete specimens used in this experimental investigation, table 5.3 shows a brief recap of the general properties used for the analytical verification of steel-stress levels and surface crack widths as assumed, observed and/or calculated.

Table 5.3: General experimental properties

Parameter	Magnitude	Refer to
Concrete parameters:		
concrete cover	$c = 30 \text{ mm}$	section 3.3
Beam width	$b = 150 \text{ mm}$	section 3.3
Beam height	$h = 140 \text{ mm}$	section 3.3
Concrete tensile strength	$f_{tc} = 3.1 \text{ MPa}$	section 3.4
Concrete flexural strength	$f_{c,fl} = 4.6 \text{ MPa}$	section 3.4
Concrete compressive strength	$f_{cu} = 59.1 \text{ MPa}$	section 3.4
Concrete modulus of elasticity	$E_{conc} = 31 \text{ GPa}$	SANS 10100-2
Reinforcement parameters:		
Reinforcement diameter	$\varnothing = 10 \text{ mm}$	section 3.3
Steel modulus of elasticity	$E_{steel} = 213.0 \text{ MPa}$	section 3.10
Steel yielding strength	$f_y = 519.6 \text{ MPa}$	section 3.10
Steel ultimate tensile strength	$f_{uts} = 525.5 \text{ MPa}$	section 3.10

The following equations follow, unless stated otherwise, from [SANS 10100-2](#) and [NEN 6720 \(1995\)](#) are used for the calculation of the crack formation stage.

Modulus of elasticity ratio:

$$\alpha_e = \frac{E_s}{E_c} = 6.87 \quad (5.1)$$

Moment of inertia:

$$I = \frac{b \cdot h^3}{12} = 34.3 \times 10^6 \text{ mm}^4 \quad (5.2)$$

Resisting moment:

$$W = \frac{I}{0.5 \cdot h} = 0.49 \times 10^6 \text{ mm}^3 \quad (5.3)$$

Area steel in the cross-section:

$$A_s = \frac{\varnothing^2 \cdot \pi}{4} = 78.5 \text{ mm}^2 \quad (5.4)$$

Reinforcement ratio of the cross-section:

$$\rho = \frac{A_s}{b \cdot d} = 0.00499 \quad (5.5)$$

Taking into account that up to first cracking the elastic state still applies:

$$\frac{\varepsilon_c}{\varepsilon_s} = \frac{x}{d - x} \quad (5.6)$$

$$\frac{x}{d} = -\alpha_e \cdot \rho + \sqrt{(\alpha_e \cdot \rho)^2 + 2 \cdot \alpha_e \cdot \rho} \quad (5.7)$$

with $d = 105$ mm and the height of the compressive zone at $x = 24.12$ mm, the internal lever arm is equal to:

$$z = d - 1/3 \cdot x = 96.6 \text{ mm} \quad (5.8)$$

Cracking moment:

$$M_r = f_{c,fl} \cdot W = 2.267 \times 10^6 \text{ Nmm} \quad (5.9)$$

Steel stress, σ_{ss} , in the crack is then equal to (refer to figure [5.1b](#)):

$$\sigma_{ss} = \frac{M_r}{A_s \cdot z} = 297.7 \text{ MPa} \quad (5.10)$$

The steel stress-surface crack width relationship can then be determined. For example, the further away from the primary crack, the smaller the steel stress becomes. This is

illustrated in figure 5.1b. The strain just before the onset of the next bending crack is then equal to:

$$\varepsilon_r = \frac{f_{c,fl}}{E_c} = 1.49 \times 10^{-4} \quad (5.11)$$

The concrete strain at reinforcement level:

$$\frac{\frac{h}{2} - d}{h/2} \cdot \varepsilon_r = -7.46 \times 10^{-5} \quad (5.12)$$

Steel stress at the end of the transmission length is then:

$$\sigma_{se} = E_s \cdot \varepsilon_c = 15.9 \text{ MPa} \quad (5.13)$$

Force introduced over the transmission length L_t to give rise to the steel stress:

$$N_t = (\sigma_{se} - \sigma_e) \cdot A_s = 22.134 \text{ kN} \quad (5.14)$$

The bond strength is therefore equal to:

$$\tau_{bs} = 1.8 \cdot f_{tc} = 5.58 \text{ N/mm}^2 \quad (5.15)$$

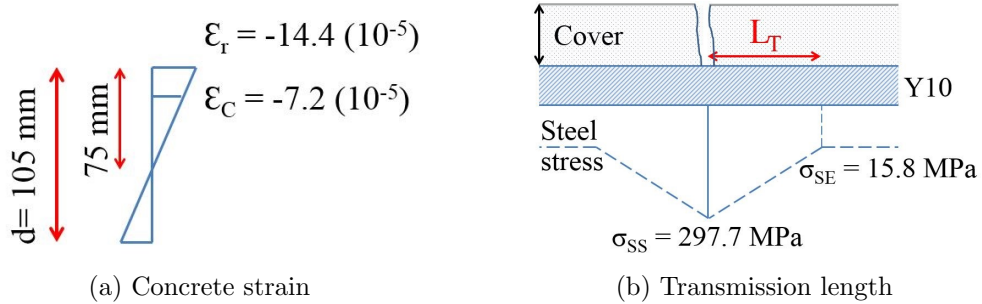


Figure 5.1: Concrete strain at surface and transmission length, adapted from Blagojević (2015, pg. 133)

With the contribution of the concrete cover, the transmission length can be calculated as follows:

$$L_t = 0.75 \cdot c + \frac{N}{\varnothing \cdot \tau_{bs} \cdot \pi} = 148 \text{ mm} \quad (5.16)$$

Typical crack spacing can vary between:

$$S_{min} = 1.0 \cdot L_t = 148.7 \text{ mm}$$

$$S_{mean} = 1.5 \cdot L_t = 223.1 \text{ mm}$$

$$S_{max} = 2.0 \cdot L_t = 297.5 \text{ mm}$$

To determine the strain over S_{mean} :

$$\varepsilon_{sm} = \frac{\sigma_s}{E_s} \cdot \left(1 - \beta_1 \cdot \beta_2 \cdot \left(\frac{\sigma_{sr}}{\sigma_s} \right)^2 \right) \quad (5.17)$$

where:

$\beta_1 = 1.0$ is the bond factor for ribbed steel

$\beta_2 = 0.5$ for long term loading

The mean crack width is calculated as follows:

$$w_{cw,mean} = S_{mean} \cdot \varepsilon_{sm} = \frac{\sigma_s}{E_s} \cdot \left(1 - \beta_1 \cdot \beta_2 \cdot \left(\frac{\sigma_{sr}}{\sigma_s} \right)^2 \right) \quad (5.18)$$

The relationship between steel-stress level and the surface crack width is shown in figure 5.2 where it can be seen that for a 0.4 ± 0.1 mm surface crack width in a beam specimen with a single reinforcement rod, the steel stress can be in the order of 350 to 500 MPa. It can also be seen that the relation between steel stress and surface crack width depends on the crack spacing. Therefore, the crack spacing and surface crack width vary as a function of the specific steel stress as shown in figure 5.2. S_{min} , S_{mean} and S_{max} refer to the minimum, average and maximum theoretical crack spacing respectively.

5.2 Steel-stress level

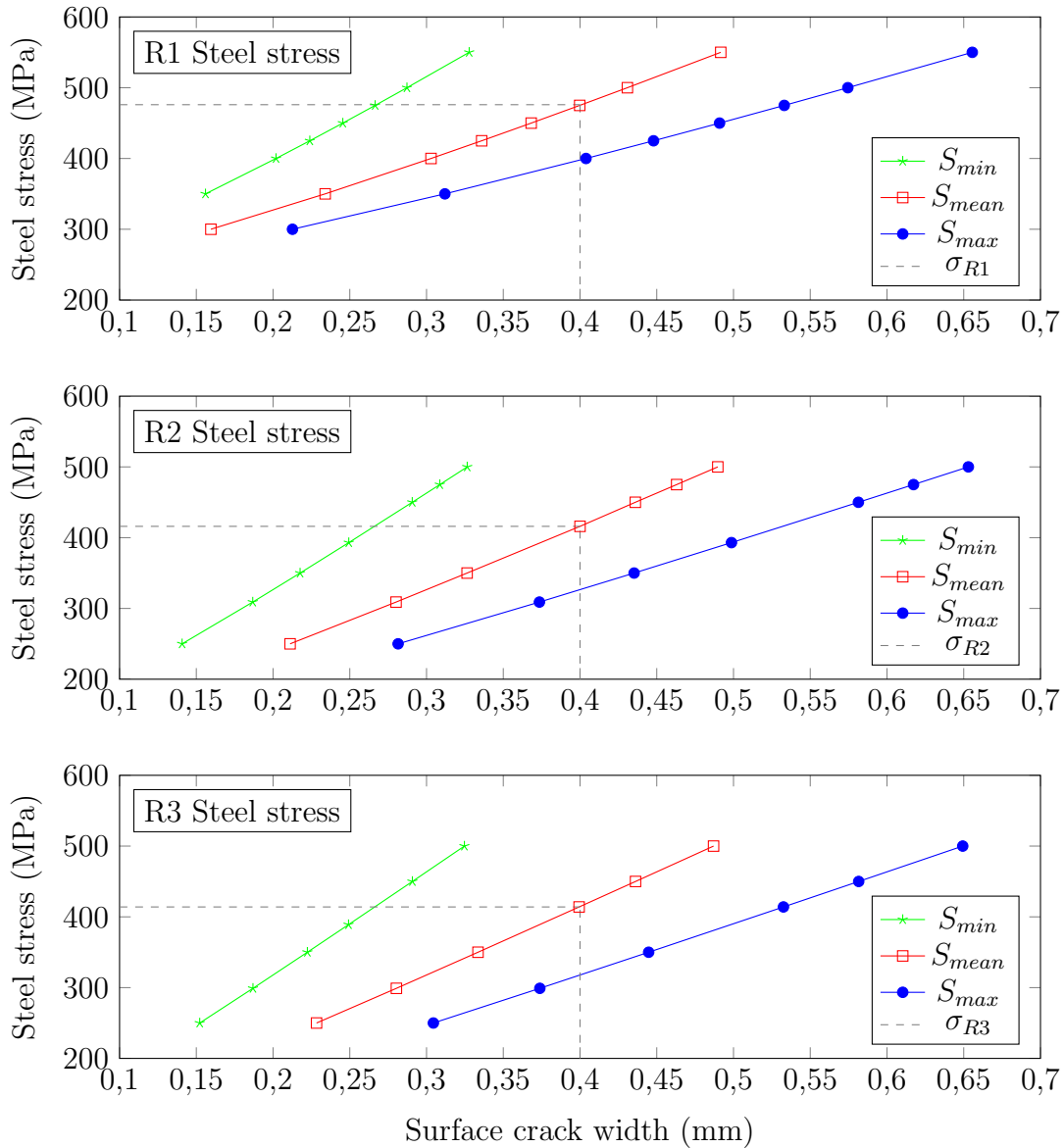


Figure 5.2: Relation between steel-stress level and surface crack width

It is observed from the figure 5.2 is that an increase in reinforcement rods decreases the average steel-stress level for the same surface w_c . The relation between the surface w_c and the steel stress depends on the amount of reinforcement in the cross-sectional area of the concrete beam. Therefore, for a specific target crack width, more reinforcement would result in a lower steel stress in the individual reinforcement bars. Section 5.2.2 explores the relationship between the steel-stress level in relation to the corrosion rates measured in chapter 4 this investigation.

5.2.2 Relationship between steel-stress level and corrosion rate

From the analytical calculation of the surface crack width-steel stress relationship for different reinforcement layouts, the mean steel stress is shown to be higher for wider crack widths. This is an expected result as a greater force is required to achieve a wider crack width. Wider surface crack widths is of importance as this is the region where localised corrosion occur. Recall from figure 5.1b that the highest steel stress typically coincides with this point where localised corrosion may occur. This point where the expected highest steel stress and localised corrosion occurs is defined as the “critical point” (Blagojević 2015). The mean steel-stress levels of all the concrete beam specimens in this investigation are shown in figure 5.3 for their respective measured surface crack widths. A 150 mm digital vernier caliper with a resolution of 0.01 mm is used to measure the crack widths reported in table A.2. The steel stress is calculated from the mean and max crack width relationship shown in figure 5.2, $w_{c,mean}$ and $w_{c,max}$ respectively. It is noted that the minimum crack width, $w_{c,min}$, is not presented on this curve. This is omitted due to some of the resulting steel-stress levels exceeding 520 MPa, which is determined as the yielding stress for this investigation. This would imply that the rod would have already yielded in the instance of minimum crack width.

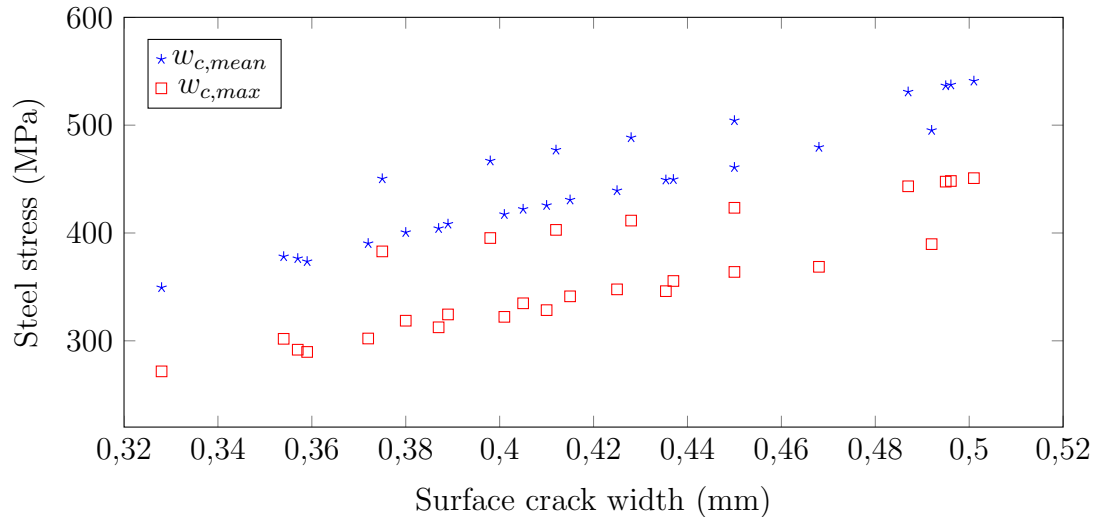


Figure 5.3: Relation between steel-stress level and surface crack width

From the surface crack widths of each beam specimen, the average steel stress for each

specimen is plotted against the corrosion rate measured in chapter 4. This relationship is shown in figure 5.4. $w_{c,min}$ is omitted from this illustration.

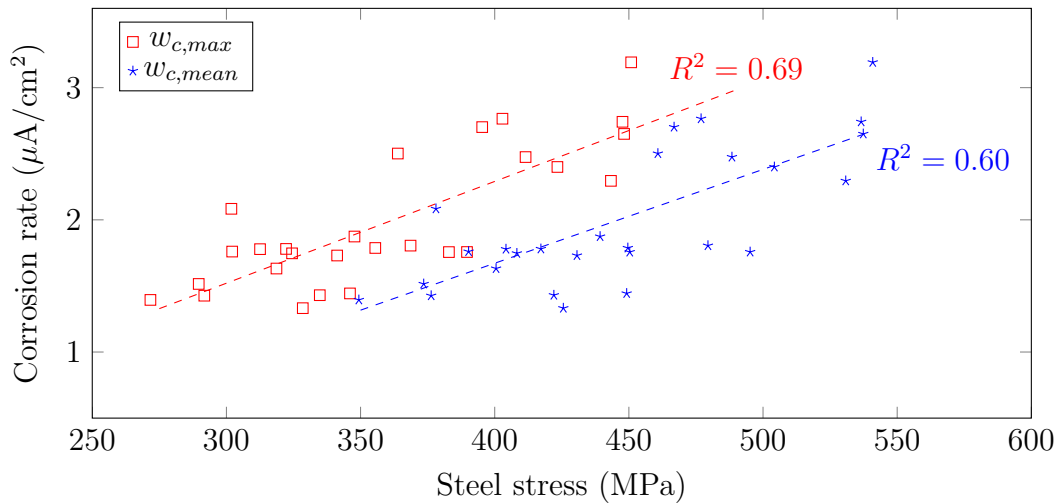


Figure 5.4: Relationship between steel stress and corrosion rate

Figure 5.4 shows that there is a correlation between corrosion rate and steel-stress level. However, this formulation does not account for the time dependant nature of corrosion rates and the fluctuations encountered throughout the study. For example, the corrosion rates reported in chapter 4 over the course of 36 weeks increased as follows: 0.201, 0.748 and $1.935 \mu\text{A}/\text{cm}^2$ for week 1, 15 and 35 respectively. This relationship may be an insight to how corrosion rate is influenced by the steel-stress levels as follows:

- (i) A higher steel stress will lead to more microcracking at the reinforcement level. This results in finer passages that follow from the initial crack* that allow corrosion agents (Cl^- , H_2O and O_2) greater access. And as a result, this may lead to a higher corrosion rate.
- (ii) With the introduction of finer cracks around the reinforcement rod, the size of the anode will also increase around the initial crack*. This will ultimately lead to a reduction in steel-concrete bond.
- (iii) As the steel-stress levels increase, this may result in propagating consequences whereupon a higher steel stress increases microcracking around the concrete-steel interface. Microcracking results in an increase in penetrability at the reinforcement level which then leads to the formation of a larger anode

5.3 Empirical corrosion rate prediction models

region(s). The anode region accumulates rust products and further reduces the concrete-steel bond. With a decrease in concrete-steel bond, the load bearing capacity of the RC member is reduced.

* initial crack refers to the crack that is joined to the surface.

It should be stated again that this study considers only a small range of surface crack widths (0.41 ± 0.05 mm [$\bar{x} \pm \sigma$]), for a small range of corrosion rate values (average i_{corr} values for weeks 34 - 36) and did not include factors such as creep, shrinkage and self-healing of the cracks.

5.3 Empirical corrosion rate prediction models

5.3.1 Review of existing empirical models

Empirical models are generally developed from laboratory experiments designed to isolate their basic concrete parameters such as binder type, w/b ratio and environmental exposure conditions (Bjegović et al. 2006). The main problem with empirical models is the set of limitations under which they are developed, which makes them neglect the interaction of other variables towards both the concrete and the corrosion process. Therefore, the problem is isolated to only one set of variables. These limitations associated with the models are commonly neglected and therefore may result in a gross under- or overestimation of residual service life (Otieno 2014).

5.3.1.1 Morinaga (1988)

A study by Morinaga (1988) showed that factors such as concrete quality (w/b ratio, binder type), concrete cover, exposure conditions (temperature and humidity), chloride content and dissolved oxygen content affect corrosion rate and should, therefore, be considered in the prediction of corrosion rate. The study was conducted on both chloride- and carbonation-induced specimens, however, only the chloride-induced corrosion model is discussed in this review. The experimental variables tested are w/b ratio (0.40, 0.55 and 0.70), concrete cover (4, 5, 6, 8, 9, 12, 13, 16, 20, 22, 27, 29 and 37 mm) and admixed chloride content (0, 0.1, 0.5, 1.0, 1.5 and 3% as sodium chloride by mass of mixing water). The gravimetric mass loss of the specimens was used as the corrosion rate method. A regression analysis ($R^2 =$

5.3 Empirical corrosion rate prediction models

0.95) was used to set up the prediction model presented in equation 5.19 (Morinaga 1988).

$$i_{corr} = \frac{d_{st}}{d^2} \cdot \left(-0.51 - 7.60 \cdot C_{cl} + 44.97 \cdot \left(\frac{w}{b} \right)^2 + 66.95 \cdot C_{cl} \left(\frac{w}{b} \right)^2 \right) \quad (5.19)$$

where i_{corr} is the corrosion rate (10^{-4} g/cm²/year), d_{st} is the reinforcement diameter (mm), d is the concrete cover (mm) and C_{cl} is the NaCl content % by mass of mixing water.

To incorporate the effects of temperature and humidity, Moringa further extended the study to create a more comprehensive model by exposing grout coated reinforcing steel to different conditions for 8 years. Temperature (20 and 40 °C), air oxygen concentration (0, 10 and 20 % O₂) and relative humidity (0, 51, 62, 100 % RH and submerged) yielded a new regression model ($R^2 = 0.85$) as shown in equation 5.20 (Morinaga 1988).

$$\begin{aligned} i_{corr} = & 2.59 - 0.05 \cdot T - 6.89 \cdot (RH - 0.45) - 22.87 \cdot C_{O_2}^{air} \\ & - 0.99 \cdot C_{cl} + 0.14 \cdot (RH - 0.45) + 0.51 \cdot T \cdot C_{O_2}^{air} + 0.01 \cdot T \cdot C_{cl} \\ & + 60.18 \cdot (RH - 0.45)_{O_2}^{air} + 3.36 \cdot (RH - 0.45) \cdot C_{cl} + 7.32_{O_2}^{air} \cdot C_{cl} \end{aligned} \quad (5.20)$$

where $C_{O_2}^{air}$ is the exposure air oxygen concentration (% O₂).

However, this model did not incorporate w/b ratio which was presented in the initial model in equation 5.19. The prediction model proposed in equation 5.20 also omitted the binder type which can substantially effect the corrosion rate as discussed in chapters 2 and 3. The question of validity of grout coated reinforcing also comes to mind as the factors such as porosity, resistivity and permeability are essentially different for concrete and grout. Although, this model comprised of long-term measurements, there is no guideline available for incorporating them (Otieno 2014).

5.3.1.2 Vu et al. (2005)

In an experimental study by Vu et al. (2000), a corrosion prediction model of the corrosion initiation and corrosion propagation stage was proposed. The experimental

5.3 Empirical corrosion rate prediction models

program was conducted over the course of one year in 20 °C and RH of 75%. The effects of w/b ratio and cover depth were investigated. The end of the corrosion initiation (after one year) stage and the corrosion propagation stage is represented in equations 5.21 and 5.22 respectively (Vu et al. 2000).

$$i_{corr(1)} = \frac{37.8 \cdot (1 - w/b)^{-1.64}}{c} \quad (5.21)$$

$$i_{corr} = i_{corr(1)} \cdot 0.85 \cdot t_p^{-0.29} = \left(\frac{(32.13 \cdot (1 - w/b)^{1.64})}{c} \right) \cdot t_p^{-0.29} \quad (5.22)$$

The proposed model has taken into account the effects of concrete quality by incorporating a w/b input parameter and concrete cover. However, when plotting the corrosion rate over time, it is uncertain whether or not the time-development curve of corrosion rate over time will decrease. Similarly, it is doubtful that the corrosion rate will start off at the highest possible rate and then decay to a lower corrosion rate.

5.3.1.3 Scott (2004)

In 2004 a model for cracked concrete was proposed by Scott (2004). The model is based on an experimental investigation in which the effects of crack width (0.2 and 0.7 mm), binder type (25/75; 50/50; 75/25 ratio PC/GGBS and 93/7 ratio PC/SF) and concrete cover (20 and 40 mm) on corrosion rate were observed. The investigation was performed on 120 x 120 x 375 mm specimens with a constant 0.58 w/b ratio in laboratory conditions of 30 °C. Although the effects of surface crack width were investigated, there is no input parameter for it in the proposed i_{corr} prediction model presented in equations 5.23 and 5.24 (Scott 2004).

$$i_{corr} = \left(1.43 \cdot \frac{CCI_{90}}{f} + 0.02 \right) \exp \left(\frac{40 - c}{20} \cdot 1.2 \cdot \left(\frac{CCI_{90}}{f} \right)^3 \right) \quad (5.23)$$

$$\text{and: } f = 10^{|0.5 - S| - 0.5 + S} \quad (5.24)$$

where CCI_{90} is the 90-day chloride conductivity index value (mS/cm), c is the concrete cover (mm) and f is the slag concentration factor (S is the fraction of slag).

5.3 Empirical corrosion rate prediction models

From the corrosion rate model proposed here, it is not clear what the effect of time will be on the corrosion rate, and whether the corrosion rate will increase for long-term predictions. Secondly, it seems that there is no input parameter for the surface crack width although cracked specimens were investigated in the experiment. Upon evaluation of the model, it appears that the model under-predicts the corrosion rate with the addition of GGBS. For example, it was found that for a 50/50 PC/GGBS binder composition, the corrosion rate of covers in the range of 0 to 50 mm is $0.2 \mu\text{A}/\text{cm}^2$. This indirectly implies that concrete members of 50% GGBS binder are not susceptible to durability issues.

5.3.1.4 Otieno (2014)

In a recent study by Otieno (2014), a chloride-induced i_{corr} prediction model based on an investigation over the period of 2.25 years is proposed. This model makes allowance for both cracked and uncracked concrete, as well as for laboratory (accelerated cyclic wetting and drying cycles) and field based (natural exposure) concrete specimens. The influence of concrete quality (binder type and w/b ratio), concrete cover and crack width was investigated on 120 x 130 x 375 mm concrete beam specimens. The concrete quality was influenced by two w/b ratios (0.4 and 0.55) and three binder types (PC, PC/GGBS and PC/FA). Two concrete covers (20 and 40 mm) and four different crack widths (uncracked, incipient crack, 0.4 and 0.7 mm) were investigated to produce the equations for the laboratory specimens and the field based specimens, presented in equations 5.26 and 5.26 respectively (Otieno 2014).

$$i_{corr} = (5.18 \cdot \exp(0.01 \cdot (D_{90} \cdot 10^{10}))) \cdot \left(\frac{c}{w_{cr}}\right)^{-0.96 \cdot (D_{90} \cdot 10^{10})^{-0.35}} \quad (5.25)$$

$$i_{corr} = (0.64 \cdot \exp(0.06 \cdot (D_{90} \cdot 10^{10}))) \cdot \left(\frac{c}{w_{cr}}\right)^{0.21 \cdot e^{0.02 \cdot (D_{90} \cdot 10^{10})}} \quad (5.26)$$

where i_{corr} is the corrosion rate approximately 2.25 years after corrosion initiation ($\mu\text{A}/\text{cm}^2$), D_{90} is the 90-day chloride conductivity index (cm^2/s), c is the concrete cover (mm) and w_{cr} is the surface crack width (mm).

The model showed good correlation with the predicted values as can be seen in figure 5.5. However, the model does not allow for variance of corrosion rate over time and, therefore, the accuracy of the model for long-term predictions is

5.3 Empirical corrosion rate prediction models

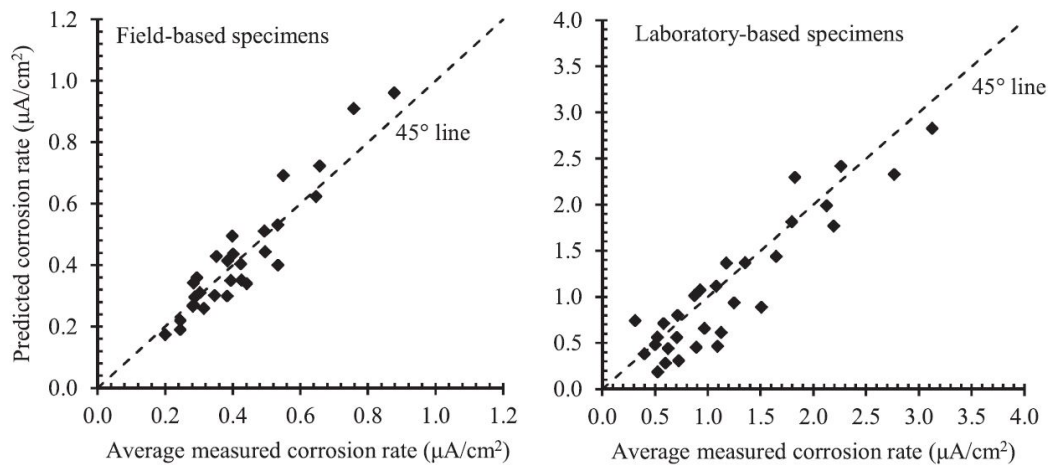


Figure 5.5: Otieno et al. (2016) prediction vs. measured i_{corr}

uncertain. Another aspect regarding the proposed model is the singularity of the measured variables, as only the corrosion effect on a single reinforcement rod and a flexure crack was investigated. In structures found in practise, the reinforcement and crack frequency can have an influence on the corrosion rate as shown in chapter 4.

5.3.2 Analysis of existing empirical models

Using the concrete variables that was implemented in this investigation, the measured i_{corr} in chapter 4 is compared to the predicted i_{corr} from the models discussed in section 5.3.1. This comparison is graphically plotted in figure 5.6 from the parameters listed in table 5.4.

Table 5.4: Model input parameters for i_{corr} prediction

Input parameter	Magnitude	Unit
Diffusion coefficient (D_{90})	10.1×10^{-10}	cm^2/s
Cover (c)	40	mm
Crack width (w_c)	0.4	mm
w/b	0.45	
\varnothing_{steel}	10	mm
Chloride content (C_{cl})	5	%
CCI_{90}	0.86	mS/cm

5.3 Empirical corrosion rate prediction models

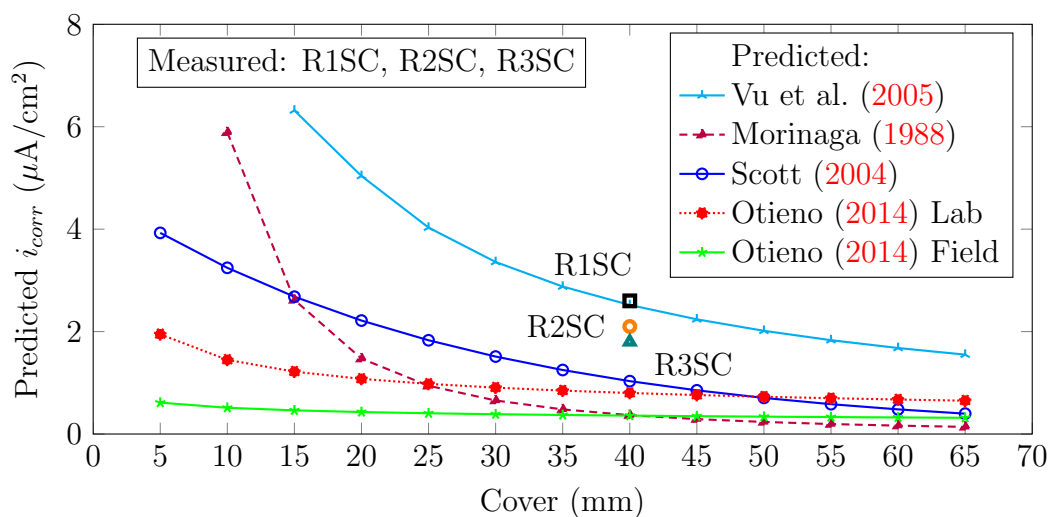


Figure 5.6: Predicted i_{corr} vs. measured i_{corr} for varying cover depths

Figure 5.6 shows that the measurement of corrosion rate on-site is still paramount to determining the prospects of a corroded structure. Only the average of the single cracks (SC) from the R1, R2 and R3 series are plotted. This is due to the fact that these models are based on single cracked specimens. Most of the models underpredicted the corrosion rate of the beams used in this investigation. However, the model proposed by Vu et al. (2005) correctly predicted the corrosion rate of the R1 series that was measured in this investigation. Therefore, it is vital to perform on-site corrosion rate measurements to calibrate these prediction models for successful integration into practice.

5.3.3 Model input parameter limitations

From the corrosion prediction models proposed in section 5.3.1, it is evident that the model input parameters are typically not easily measurable. For example, quantifying the chloride concentration at the steel level, or calculating the oxygen content, or the reinforcement temperature for instance. These inputs are generally a result of carefully designed laboratory experiments undertaken in well controlled environments. It should also be noted that the size of the specimens investigated in these models are almost always smaller than 500 mm in length, and thus far, have not included the influence that multiple reinforcement rods have on the corrosion rate. Lastly, from the literature presented in chapter 2, it is evident that the crack characteristics have an important role in the corrosion rate. The majority of the

5.4 Residual service life prediction

cracked concrete models that include the effects of crack width are only based on a singular flexural crack. It is therefore difficult to obtain a universally acceptable prediction model that can be fitted to most chloride-induced concrete members as there potentially exists a complex opposing and/or additive effect between the various corrosion rate factors.

5.4 Residual service life prediction

5.4.1 Definition of residual service life

In terms of chloride-induced corrosion, the service life of a structure within the propagation stage is governed by the condition of the steel within the concrete. This does not include the later stages of splitting cracks and spalling of cover concrete. In other words, the remaining service life of a structure is equivalent to the residual tensile capacity of the steel in in-service structures under serviceable loads. Therefore, the loss of steel capacity results in reduced structural performance (load bearing capacity). The loss of structural performance may be due to; (a) reduced effective diameter of reinforcement rods and, (b) a reduced concrete-steel bond at reinforcement level. In most cases, both a) and b) act in union resulting in substantial reduction in structural performance. Consequently, the usable service life is shortened. Deterioration generally leads to high maintenance costs and structure down-time due to rehabilitation and repairs.

5.4.2 Relationship between residual service life and corrosion rate

The cross-sectional damage of corrosion to reinforcement rods has always been seen as the most important aspect of deteriorated and corroded RC structures. Other reasons such as concrete spalling and corrosion stains for example have typically been aesthetic, although, acting as signs of damage to the loss of cross-sectional area (A_{st}) of the bars. The loss of steel cross-sectional area has therefore defined the limit state for the safe usage in terms of both meeting the ultimate limit state (ULS) and the serviceability limit state (SLS). Andrade et al. (1996) have suggested that the end of service life of a RC structure to be between when 5 % to 25 % of the cross-sectional area has been lost. The wide range is potentially because there

5.4 Residual service life prediction

are various other partial factors included in the design of RC members to justify SLS and ULS requirements. As there have not been explicit design code regulations specifying the loss of cross-sectional area or diameter, a reasonable assumption of 15 % will be defined as the limit state in this investigation.

Figure 5.7 illustrates this assumption in more detail. If the corrosion limits in table 5.1 are converted to penetration rate and plotted against time after the propagation period has started for a single Y10 reinforcement rod, the expected reduction in A_{st} for different corrosion rates is approximately linear.

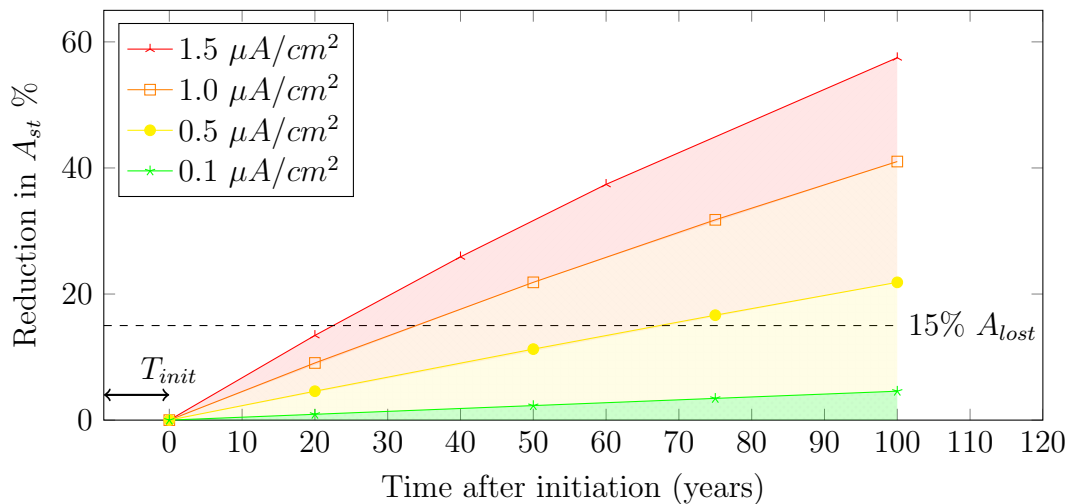


Figure 5.7: Residual time before the attainment of a 15 % limit state

After the corrosion initiation period (T_{init}), the start of the corrosion propagation period (T_{prop}) is plotted for different corrosion rates. From figure 5.7 it can be deduced that for a moderately-low corrosion rate of $0.5 \mu A/cm^2$, the expected time to the end of the propagation period will be reached in approximately 70 years. Similarly, for a 3 times higher corrosion rate ($1.5 \mu A/cm^2$, high to severe), the end of service life will be reached in approximately 20 years for a single Y10 steel rod.

5.4.3 Relationship between service life and reinforcement diameter

Similar to the relationship between the corrosion rate and the residual service life in section 5.4.2, the relationship between the diameter of the reinforcement and the residual service life is approximately linear. Once the end of the T_{init} has been

5.4 Residual service life prediction

reached, the residual service life of the structure is dependant on the diameter of the reinforcement. This relationship between reinforcement diameter and residual service life is shown in figure 5.8 for a corrosion rate of $1.0 \mu\text{A}/\text{cm}^2$. As expected, the larger the reinforcement diameter, the longer before the end of the T_{prop} is reached.

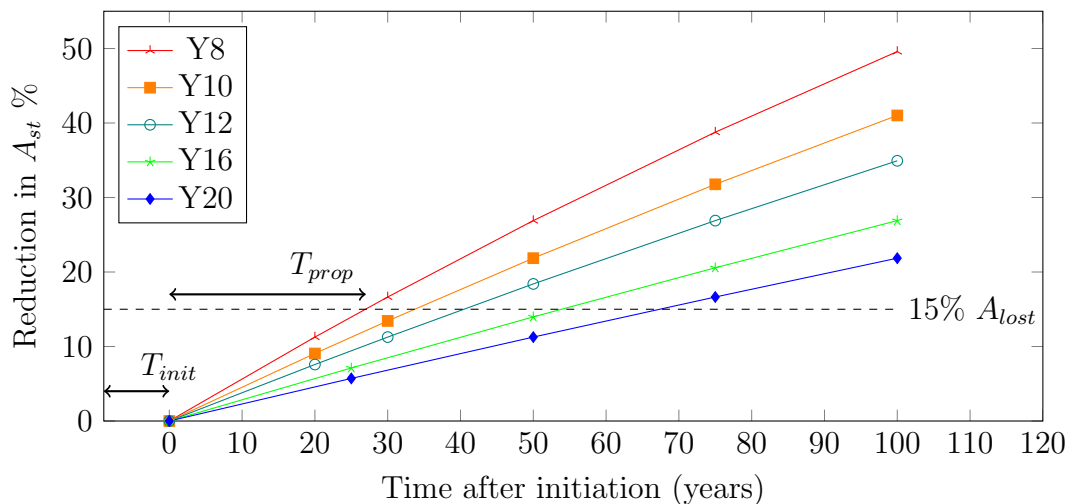


Figure 5.8: Relationship between reinforcement diameter and residual service life

5.4.4 Analysis of a proposed residual service life prediction model

From the relationships shown in sections 5.4.2 and 5.4.3, a model for predicting the time to the end of the T_{prop} may be deduced from Faraday's law of electrochemical mass loss, shown in equation 2.16. Firstly, figure 5.9 shows that the defined limit state can be a significant factor in determining the residual service life. For example, residual service life can be doubled if slightly more cross-sectional area is allowed to be corroded (5 % vs. 10 %).

5.4 Residual service life prediction

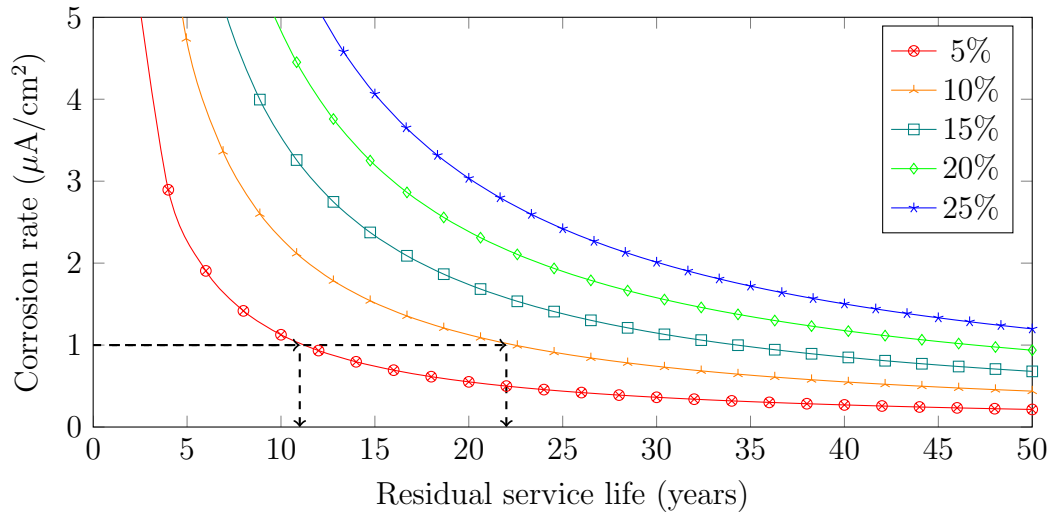


Figure 5.9: Limit states of Y10 reinforcement rod, $\alpha_{pit} = 5$

From a defined limit state, it can also be seen in figure 5.10 that the diameter of the reinforcement rod also affects the residual service life.

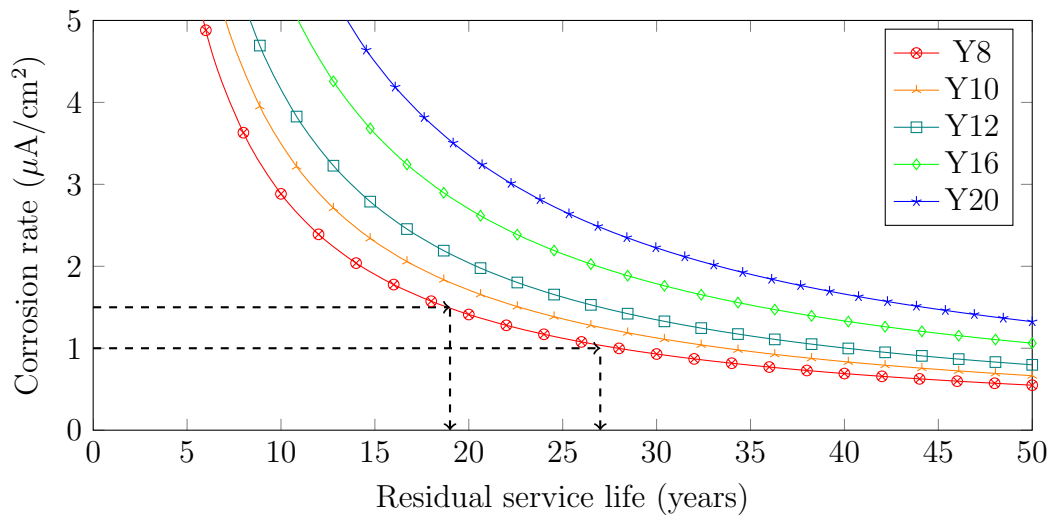


Figure 5.10: Residual service life's of reinforcement rods, $LS = 15\%$ and $\alpha_{pit} = 5$

Lastly, a pitting factor needs to be chosen to take into account the effects of localised pitting corrosion. Figure 5.11 shows the expected residual service life for a single Y10 and a 15% LS for different pitting factors.

5.4 Residual service life prediction

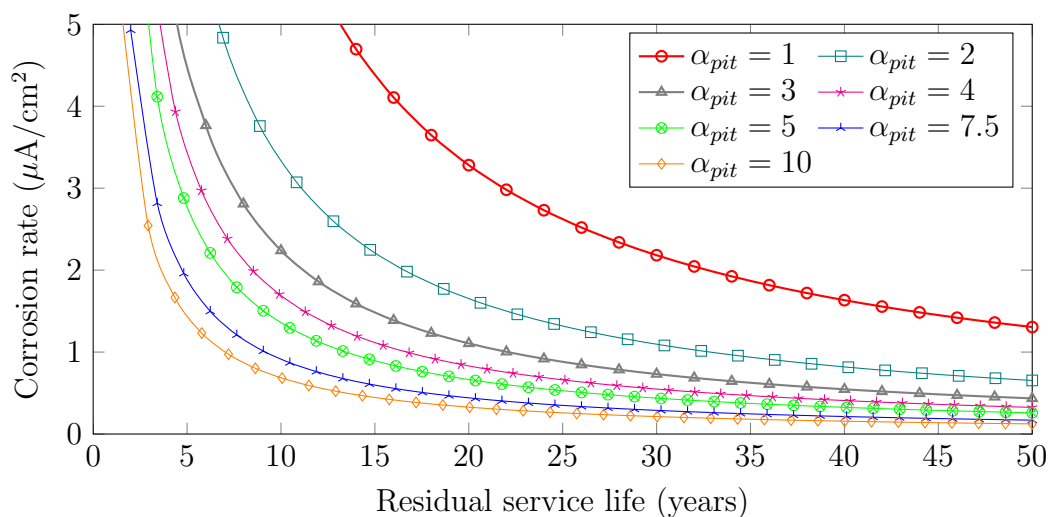


Figure 5.11: Residual service life between different α_{pit} factors, Y10 and $LS = 15\%$

By choosing the reinforcement diameter, an appropriate pitting factor and limit state, can be included into a model that, when accompanied by on-site corrosion rate readings may aid engineers in the following ways:

- (i) Determining whether or not a RC member would require maintenance and rehabilitation or if decommissioning is a more economical option.
- (ii) Planning appropriate maintenance schedules for existing structures.

Given knowledge in this regard, the remaining service life of a RC member is estimated. This model may be expanded for a variety of reinforcement diameters, limit states and pitting factors. For example, figures B.1 to B.3 illustrates the difference between multiple input parameters. The equation for determining the residual service life is given in equation 5.27.

$$T_{RSL} = \frac{LS \cdot 10}{\left(100 - \left(\left(\varnothing_{init} - (0.116 \cdot i_{corr} \cdot \alpha_{pit})\right)^2 \cdot \varnothing_{init}^{-2}\right) \cdot 100\right)} \quad (5.27)$$

where T_{RSL} is the time to the end of the propagation stage (years), LS is the limit state of the reduction in reinforcement diameter (recommended 5 - 25%), \varnothing_{init} is the initial reinforcement rod diameter (mm), i_{corr} is the measured corrosion rate ($\mu\text{A}/\text{cm}^2$) and α_{pit} is the pitting factor (recommended 1 - 10).

5.4 Residual service life prediction

However, it must be remembered that corrosion rate is an instantaneous rate for the specific instance of taking the corrosion rate reading. Therefore, this prediction is only made from the current corrosion rate. Fluctuations in corrosion rate can thus influence the estimated residual service life. It is recommended to perform multiple corrosion rate readings in order to improve the accuracy of the T_{RSL} prediction.

6. Conclusions and recommendations

6.1 Conclusions

The main aim of this study was to explore the effects of crack spacings and multiple reinforcement rods on the corrosion rate of cracked RC members exposed to chloride-induced corrosion. This investigation was motivated by the need to understand the corrosion propagation stage and consequently, the effect of the corrosion rate on the residual service life of a structure.

The results indicate that multiple cracks and multiple reinforcement rods have an effect on the corrosion rate. Taking into account that other factors are kept constant, an increase in the number of reinforcement rods connected to each other and exposed to chloride ions from the same crack resulted in a decrease in the corrosion rate. Single cracked specimens resulted in higher corrosion rates compared to multiple cracked specimens. With regard to crack spacings, smaller spacings result in higher corrosion rates. For a constant surface crack width, a higher steel-stress level leads to an increase in corrosion rate. The repercussion of a higher corrosion rate is a shorter residual structural service life. Based on the results and discussions from chapters 4 and 5, the influence of reinforcement density and crack spacing, along with other investigation objectives, are evaluated in this chapter in a more general sense.

6.1.1 Effect of multiple reinforcement rods on corrosion rate

Reinforcement density was varied in this investigation by implementing three reinforcement layouts with a constant cover of 40 mm. A single 10 mm diameter high yield strength reinforcement rod, Y10, placed at the center (R1); two Y10 rods placed 50 mm apart (R2); and three Y10 rods placed 35 mm apart were investigated. The general trend between the three layouts is the decrease in corrosion rate with an increase in reinforcement density as follows: R1 → R2 → R3.

The trend of increasing corrosion rate for decreasing reinforcement density was observed in all four of the different crack spacings investigated. After 36 weeks

of accelerated corrosion testing, corrosion rates of 2.57, 1.93 and $1.61 \mu\text{A}/\text{cm}^2$ were observed for series R1, R2 and R3 respectively. In general, an increase in reinforcement density leads to reduced anode to cathode ratio, as well as a reduced steel-stress level for the same surface crack width.

The reduced anode to cathode ratio forms due to the reduced space being available between the rods for the formation of corrosion products. Additionally, the ease of transport of the corrosion constituents to the anodic regions are limited due to the decrease in available space between the multiple reinforcement bars. Multiple reinforcement bars also lead to different steel-stress levels. This effect on the corrosion rate is discussed in section 6.1.4.

6.1.2 Effect of crack spacings on the corrosion rate

Four crack spacings were investigated by mechanically pre-cracking concrete members in three and four point bending. The crack width measured on the surface was kept constant for both the single cracked specimens (SC) and the multiple cracked specimens. The multiple cracked specimens were grouped according to crack spacing's (S_c), as follows: single crack, $65 \leq S_c \leq 85$ mm, $85 < S_c < 100$ mm and $100 \leq S_c \leq 120$ mm. An increase in corrosion rate was observed in the following crack spacing order: S75 \rightarrow S105 \rightarrow S90 \rightarrow SC. When only the multiple cracks are considered, no prominent trend is visible between the corrosion rates.

Upon termination of the experiment, the corrosion rates were 1.47, 1.78, 1.99 and $2.43 \mu\text{A}/\text{cm}^2$ for the S75, S105, S90 and SC respectively. This trend in corrosion rates was attributed to the difference in anode to cathode ratios between the different cracks. A single cracked specimen contained a relatively larger anode region than the accompanying cathode region, and hence, had a larger anode to cathode ratio. In contrast, multiple cracked specimens had smaller anode regions due to the crack spacings, and consequently, smaller anode to cathode ratios. From the electrochemical processes involved at the anodic region, the relatively larger anode to cathode ratio of the SC series specimens is able to have greater access to hydroxyl ions and more space to develop corrosion processes and corrosion products. Furthermore, it was observed that the average anode region length was approximately 35 mm upon dismantling of the specimens. It was visually observed that anode regions of

the single cracked specimen's were larger than the anode regions of the multiple cracked specimens. This trend in corrosion rates and visual observation supports the postulation made by Paul (2015) that a single crack is more vulnerable to localized pitting corrosion than multiple cracks.

6.1.3 Combined effect of crack spacing and reinforcement density

The hypothesis that a complex electrochemical relationship between the different reinforcement bars and crack spacings exists is supported by the corrosion rate results. The three reinforcement densities (R1, R2 and R3) combined with the four crack spacing series (S75, S90, S105 and SC) give rise to the hypothesis that the anode to cathode ratio effects the corrosion rate. An increase in reinforcement density leads to a decrease in the corrosion rate, while a decrease in crack spacing also leads to a decrease in the corrosion rate.

As a general overview, the single reinforcement series was susceptible to the highest corrosion rate for each crack spacing, while the highest reinforcement ratio suffered the lowest corrosion rate for each crack spacing. The corrosion rate increases according to the following trend: R3-S75,S105,S90,SC \rightarrow R2-S75,S90,S105,SC \rightarrow R1-S105,S75,S90,SC. Apart from an intricate relationship between anode and cathode regions, the increase in reinforcement density had a greater influence than the increase in crack spacings.

6.1.4 Effect of steel stress on corrosion rate

The effect of the steel-stress level on the corrosion rate was investigated through the implementation of three different reinforcement layouts, R1, R2 and R3, defined in section 6.1.1. By ensuring that a specific target surface crack width of 0.4 mm is achieved and maintained in a loading rig, the least reinforced R1 series had the highest steel stress. An increase in the reinforcement density resulted in a reduction in the steel stress of the individual reinforcement bars. Hence, the R3 series had the lowest steel stress. The trend in corrosion rate values accelerated with an increase in the steel-stress level as follows: R3 \rightarrow R2 \rightarrow R1.

The average corrosion rates for the three steel-stress levels of the R1, R2 and R3 were 2.57, 1.93 and 1.61 $\mu\text{A}/\text{cm}^2$ respectively. A higher steel stress leads to an increase in micro-cracking at the reinforcement level, allowing the corrosion process constituents greater penetrability at the reinforcement level. With the increase in small passages around the reinforcement rod, an increase in corrosion processes can be expected. This results in a larger anode region area around the initial crack. An increase in anodic surface area reduces the concrete-steel bond, which negatively influences the structural capacity of the beam.

6.1.5 Effect of corrosion rate on the residual service life

In order to investigate the effect of corrosion rate on the residual service life of a RC structure, the electrochemical corrosion rate is converted to the corrosion penetration rate. The corrosion penetration rate is multiplied with a pitting concentration factor and a pre-defined limit state (LS) for the allowable loss of reinforcement cross-sectional area. The residual service life of a structure is defined as the time remaining before the limit state is reached, indicating the end of the structural service life and/or the exceedance of the serviceability or ultimate limit state.

Residual service life predictions were determined to be greatly affected by the chosen limit state, reinforcement diameter and the pitting concentration factor. Equation 6.1 was then proposed to determine the time before the end of the corrosion propagation stage is reached. In other words, the end of the structure's usable life.

$$T_{RSL} = \frac{LS \cdot 10}{\left(100 - \left(\left(\varnothing_{init} - (0.116 \cdot i_{corr} \cdot \alpha_{pitt})\right)^2 \cdot \varnothing_{init}^{-2}\right) \cdot 100\right)} \quad (6.1)$$

where T_{RSL} is the time remaining before the end of the structural service life is reached (years), LS is the predefined limit state of allowable loss of A_{st} (%), i_{corr} is the measured corrosion rate ($\mu\text{A}/\text{cm}^2$), \varnothing_{init} is the initial diameter of the reinforcement (mm) and α_{pitt} is the pitting factor (1-10).

The proposed model could assist engineers:

- (i) In the decision to either rehabilitate and maintain or decommission a RC member based on the remainder of its serviceable life.
- (ii) By prioritising maintenance schedules in terms of the rehabilitation cost for critical RC members.

6.1.6 General conclusions

This study has made a stride towards understanding the combined effects of multiple cracks and reinforcement rods on chloride-induced corrosion in RC structures. From this research, it is clear that there is a relationship between multiple steel rods and the corrosion rate of RC members. It is also shown that there is a relationship between the single cracks and multiple cracks. However, the influence between crack spacings was not as great an influence as that of single cracks alone.

This study has also proposed a model for predicting the residual service life of a structure by selecting the attained limit state, reinforcement diameter and pitting factor. Further studies are evidently needed to incorporate more factors into the service life prediction model. Future studies will also improve the relevance of laboratory studies with on-site corrosion rate measurements of serviceable structures in practice.

6.2 Recommendations

The following recommendations are made for further research:

- (i) On-site corrosion rate measurements of structures in the tidal splash zone.
The correlation could aid the calibration of existing corrosion rate assessment techniques. Real world structures are also susceptible to dynamic load cases, varying exposure conditions and complex electrochemical relationships between multiple cracks and reinforcement bars. Knowledge in this regard may improve corrosion rate prediction models.
- (ii) Quantification of autogenous crack healing.
The effects of concrete self-healing can be advantageous to the service life of a RC structure as the crack widths decrease. The effects thereof should be studied as to better understand the crack dynamics and rates of closure under a variety of load conditions.

(iii) Quantification of the corrosion pitting factor.

Corrosion studies involving electrochemical corrosion assessment techniques should be calibrated with the physical mass loss of a gravimetric study. Improved quantification of the pitting factor can be achieved by metallurgic studies on the corroded reinforcement rods. This will greatly reduce the error between gravimetric and electrochemical techniques of corrosion assessment.

(iv) Crack spacing index for RC.

An index should be investigated for the correlation between surface crack width, crack spacing and corrosion rate for multiple types of concrete binder compositions. A index could in future aid preliminary on-site corrosion assessments without the need of corrosion rate instrumentation.

(v) Prolonged experimental programs.

The proposed loss of yield force model for a given mass loss can be improved with longer durations of corrosion studies (>2 years). Extended corrosion studies could further improve the understanding of anode and cathode region interactions in cracked RC members.

(vi) Influence of dynamic loads.

The effects of dynamic load combinations on the micro-cracking could aid the understanding of anode regions forming at the concrete-steel interface and their affect on the corrosion rate. Cyclic loading also reduces the potential for crack self-healing.

(vii) Concrete ageing on the transport properties.

It is well known that cement continuous the hydration process over time, and currently there are no available research with regard to the corrosion rate on structures over long periods of time (>25 years).

References

- ACI 211.1-91 (1999) Standard practice for selecting proportions for normal, heavyweight, and mass concrete* (1999). Standard. American Concrete Institute (cit. on p. 61).
- ACI 224 (1994) Control of Cracking in Concrete Structures* (1994). Standard. American Concrete Institute (cit. on p. 29).
- Adiyastuti, S. M. (2005). *Influence of cracks on chloride induced corrosion in reinforced concrete flexural members*. University of New South Wales (cit. on p. 20).
- Alexander, M. and D. Davis (1991). “Aggregates in concrete—a new assessment of their role”. In: *Concrete Beton* 59, pp. 10–20 (cit. on p. 59).
- Alexander, M. and B. Magee (1999). “Durability performance of concrete containing condensed silica fume”. In: *Cement and concrete research* 29.6, pp. 917–922 (cit. on p. 22).
- Alexander, M. and S. Mindess (2010). *Aggregates in concrete*. CRC Press (cit. on pp. 10, 13, 14).
- Alonso, C., C. Andrade, M. Castellote, and P. Castro (2000). “Chloride threshold values to depassivate reinforcing bars embedded in a standardized OPC mortar”. In: *Cement and Concrete research* 30.7, pp. 1047–1055 (cit. on p. 8).
- Alonso, C., C. Andrade, and J. Gonzalez (1988). “Relation between resistivity and corrosion rate of reinforcements in carbonated mortar made with several cement types”. In: *Cement and concrete research* 18.5, pp. 687–698 (cit. on p. 52).
- Andrade, C. and C. Alonso (1996). “Corrosion rate monitoring in the laboratory and on-site”. In: *Construction and Building Materials* 10.5, pp. 315–328 (cit. on pp. 39–42, 46, 49, 50, 72, 73, 120).
- Andrade, C. and C. Alonso (2001). “On-site measurements of corrosion rate of reinforcements”. In: *Construction and building materials* 15.2, pp. 141–145 (cit. on pp. 34, 49).
- Andrade, C. and C. Alonso (2004). “Test methods for on-site corrosion rate measurement of steel reinforcement in concrete by means of the polarization resistance method”. In: *Materials and Structures* 37.9, pp. 623–643 (cit. on p. 46).
- Andrade, C., C. Alonso, and A. Arteaga (1997). “Models for predicting corrosion rates”. In: *Brussel: Brite-Euram Project* (cit. on pp. 35, 101).
- Andrade, C. and I. Martinez (2005). “Calibration by gravimetric losses of electrochemical corrosion rate measurement using modulated confinement of the current”. In: *Materials and Structures* 38.9, pp. 833–841 (cit. on p. 77).

- Andrade, C., I. Martinez, N. Rebolledo, and A. Castillo (2017). “Development of an engineering approach for modelling corrosion attack”. In: *Integral Service Life Modelling of Concrete Structures* (cit. on p. 34).
- Angst, U., B. Elsener, C. Larsen, and Ø. Vennesland (2010). “Considerations on the effect of sample size for the critical chloride content in concrete”. In: *2nd International Symposium on Service Life Design for Infrastructure*, pp. 4–6 (cit. on p. 62).
- Arya, C. and F. Ofori-Darko (1996). “Influence of crack frequency on reinforcement corrosion in concrete”. In: *Cement and Concrete Research* 26.3, pp. 345–353 (cit. on pp. 17, 26–28).
- Arya, C. and Y. Xu (1995). “Effect of cement type on chloride binding and corrosion of steel in concrete”. In: *Cement and Concrete Research* 25.4, pp. 893–902 (cit. on p. 22).
- ASTM E8/E8M-09 (2011) *Standard Test Methods for the Tension Testing of Materials* (2011). Standard. ASTM International, USA (cit. on p. 79).
- ASTM, C. G. (2015). *Standard Test Method for Corrosion Potentials of Uncoated Reinforcing Steel in Concrete*. ASTM International (cit. on pp. 53, 92, 95).
- Bentur, A., N. Berke, and S. Diamond (1997). *Steel corrosion in concrete: fundamentals and civil engineering practice*. CRC Press (cit. on pp. 19, 24).
- Bertolini, L., B. Elsener, P. Pedferri, E. Redaelli, and R. B. Polder (2013). *Corrosion of steel in concrete: prevention, diagnosis, repair*. John Wiley & Sons (cit. on p. 9).
- Beushausen, H., M. Alexander, and Y. Ballim (2012). “Early-age properties, strength development and heat of hydration of concrete containing various South African slags at different replacement ratios”. In: *Construction and Building Materials* 29, pp. 533–540 (cit. on p. 22).
- Bjegović, D., V. Krstić, and D. Mikulić (2006). “Design for durability including initiation and propagation period based on the fuzzy set theory”. In: *Materials and Corrosion* 57.8, pp. 642–647 (cit. on p. 114).
- Blagojević, A. (2015). “The Influence of Cracks on the Durability and Service Life of Reinforced Concrete Structures in relation to Chloride-Induced Corrosion”. PhD thesis (cit. on pp. 1, 10, 21, 28, 38, 67, 90, 109, 112).
- Böhni, H. (2005). *Corrosion in reinforced concrete structures*. Elsevier (cit. on p. 12).
- Boulfiza, M., K. Sakai, N. Banthia, and H. Yoshida (2003). “Prediction of chloride ions ingress in uncracked and cracked concrete”. In: *ACI Materials Journal* 100.1 (cit. on pp. 15, 16).

- Breysse, D. and B. Gérard (1997). “Transport of fluids in cracked media”. In: *Rilem report*, pp. 123–154 (cit. on p. 16).
- Broomfield, J. (1994). “Corrosion rate measurements in reinforced concrete structures by a linear polarization device”. In: *Special Publication* 151, pp. 163–182 (cit. on p. 54).
- Broomfield, J. (2002). *Corrosion of steel in concrete: understanding, investigation and repair*. CRC Press (cit. on pp. 52, 53, 95).
- BS 8110-1 (1997), *Structural use of concrete - Part 1: Code of practice for design and construction* (2010). Standard. British Standards Institute (cit. on p. 29).
- BS-EN-1992-1-2 (2004) *Eurocode 2: Design of concrete structures - Part 1-1: General rules and rules for buildings* (2004). Standard. European Standards (cit. on p. 24).
- BS-EN-206-1 (2000) *Concrete - Part 1: Specification, performance, production and conformity* (2000). Standard. European Standard (cit. on pp. 18, 60).
- Cao, Z.-L., S.-D. Mi, H.-Y. Chen, Z.-C. Su, L.-Y. Wei, and M. Hibino (2016). “Relationship between microcell corrosion and macrocell corrosion of reinforcing steel in concrete structures”. In: *Green Building, Environment, Energy and Civil Engineering: Proceedings of the 2016 International Conference on Green Building, Materials and Civil Engineering (GBMCE 2016), April 26-27 2016, Hong Kong, PR China*. CRC Press, p. 303 (cit. on pp. 36, 37).
- CEB, D. C. S.-C. (1992). “Design Guide”. In: *Bulletin D’Information* 182, p. 18 (cit. on p. 25).
- Chu, C.-T., P. D. Fuqua, and J. D. Barrie (2006). “Corrosion characterization of durable silver coatings by electrochemical impedance spectroscopy and accelerated environmental testing”. In: *Applied optics* 45.7, pp. 1583–1593 (cit. on p. 47).
- Corrosion Testing, A. C. G.-1. on (2011). *Standard practice for preparing, cleaning, and evaluating corrosion test specimens*. ASTM International (cit. on p. 76).
- Daigle, L., Z. Lounis, and D. Cusson (2004). “Numerical prediction of early-age cracking and corrosion in high performance concrete bridges—case study”. In: *downloaded: August 22*, p. 2006 (cit. on p. 8).
- Dhir, R., M. El-Mohr, and T. Dyer (1997). “Developing chloride resisting concrete using PFA”. In: *Cement and Concrete Research* 27.11, pp. 1633–1639 (cit. on p. 22).
- Edvardsen, C., M. T. Jepsen, C. Andrade, and J. Kropp (2002). “Chloride migration coefficients from non-steady-state migration experiments at environment-friendly Green concrete”. In: *Proceedings of the 2nd international RILEM workshop testing and modelling the chloride ingress into concrete*, pp. 203–209 (cit. on p. 20).

- Elsener, B., O. Klinghoffer, T. Frolund, E. Rislund, Y. Schiegg, and H. Böhni (1997). “Assessment of reinforcement corrosion by means of galvanostatic pulse technique”. In: *Proceedings of International Conference on Repair of Concrete Structures-From Theory to Practice in a Marine Environment*, pp. 391–400 (cit. on pp. 43, 72).
- Elsener, B., H. Wojtas, and H. Böhni (1994). “Galvanostatic Pulse Measurements-Rapid on Site Corrosion Monitoring”. In: *Corrosion and corrosion protection of steel in concrete. Proceedings of international conference held at the University of Sheffield, 24-28 July 1994. Volume 1* (cit. on p. 49).
- Eurocode 2: Design of Concrete Structures: Part 1-1: General Rules and Rules for Buildings* (2004). British Standards Institution (cit. on pp. 29, 61).
- Fib model code for concrete structures 2010* (2013). Model Code. Du Béton, Fédération Internationale (cit. on pp. 29, 60).
- François, R., A. Castel, T. Vidal, and K. Vu (2006). “Long term corrosion behavior of reinforced concrete structures in chloride environment”. In: *Journal de Physique IV (Proceedings)*. Vol. 136. EDP sciences, pp. 285–293 (cit. on p. 28).
- Gonzalez, J., C. Andrade, C. Alonso, and S. Feliu (1995). “Comparison of rates of general corrosion and maximum pitting penetration on concrete embedded steel reinforcement”. In: *Cement and concrete research* 25.2, pp. 257–264 (cit. on p. 35).
- Gonzalez, J., A. Molina, M. Escudero, and C. Andrade (1985). “Errors in the electrochemical evaluation of very small corrosion rates—I. polarization resistance method applied to corrosion of steel in concrete”. In: *Corrosion Science* 25.10, pp. 917–930 (cit. on p. 48).
- Goto, Y. (1971). “Cracks formed in concrete around deformed tension bars”. In: *Journal Proceedings*. Vol. 68. 4, pp. 244–251 (cit. on p. 30).
- Gowers, K. and S. Millard (1999). “Measurement of Concrete Resistivity for Assessment of Corrosion”. In: *ACI Materials Journal* 96.5 (cit. on p. 51).
- Hamdy, A. S., E. El-Shenawy, and T. El-Bitar (2006). “Electrochemical impedance spectroscopy study of the corrosion behavior of some niobium bearing stainless steels in 3.5% NaCl”. In: *International Journal of Electrochemical Science* 1.4, pp. 171–80 (cit. on p. 46).
- Hansson, C., A. Poursaee, and A. Laurent (2006). “Macrocell and microcell corrosion of steel in ordinary Portland cement and high performance concretes”. In: *Cement and Concrete Research* 36.11, pp. 2098–2102 (cit. on p. 36).
- Heckroodt, R. O. (2002). *Guide to the deterioration and failure of building materials*. Thomas Telford (cit. on p. 5).

- isdcorr* (2015). URL: www.isdcorr.com/www.isdcorr.com/GECOR%5C_10.../GECOR%5C%2010%5C_2015%5C_ENG.pdf (visited on 09/07/2016) (cit. on pp. 52, 74, 151).
- Ismail, M., A. Toumi, R. François, and R. Gagné (2008). “Effect of crack opening on the local diffusion of chloride in cracked mortar samples”. In: *Cement and concrete research* 38.8, pp. 1106–1111 (cit. on pp. 17, 20).
- Jaffer, S. J. and C. M. Hansson (2009). “Chloride-induced corrosion products of steel in cracked-concrete subjected to different loading conditions”. In: *Cement and Concrete Research* 39.2, pp. 116–125 (cit. on pp. 9, 28).
- Jones, D. A. and N. Greene (1966). “Electrochemical measurement of low corrosion rates”. In: *Corrosion* 22.7, pp. 198–205 (cit. on p. 44).
- Kropp, J., M. Alexander, R. Torrent, and L. F. Luco (2007). “Transport mechanisms and reference tests”. In: *RILEM TC*, pp. 13–34 (cit. on p. 13).
- Lambert, P., C. Page, and P. R. Vassie (1991). “Investigations of reinforcement corrosion. 2. Electrochemical monitoring of steel in chloride-contaminated concrete”. In: *Materials and Structures* 24.5, pp. 351–358 (cit. on p. 8).
- Liu, Y. (1996). “Modeling the time-to-corrosion cracking of the cover concrete in chloride contaminated reinforced concrete structures”. PhD thesis. Virginia Polytechnic Institute and State University (cit. on pp. 10, 19).
- Mackechnie, J. R. (1995). “Predictions of reinforced concrete durability in the marine environment”. PhD thesis. University of Cape Town (cit. on p. 15).
- Mangat, P., J. Khatib, and B. Molloy (1994). “Microstructure, chloride diffusion and reinforcement corrosion in blended cement paste and concrete”. In: *Cement and Concrete Composites* 16.2, pp. 73–81 (cit. on p. 23).
- Marsavina, L., K. Audenaert, G. De Schutter, N. Faur, and D. Marsavina (2009). “Experimental and numerical determination of the chloride penetration in cracked concrete”. In: *Construction and Building Materials* 23.1, pp. 264–274 (cit. on p. 16).
- Melchers, R. E. and R. Jeffrey (2012). “Corrosion of long vertical steel strips in the marine tidal zone and implications for ALWC”. In: *Corrosion Science* 65, pp. 26–36 (cit. on p. 18).
- Morinaga, S. (1988). “Prediction of service lives of reinforced concrete buildings based on rate of corrosion of reinforcing steel”. In: *Special report of Institute of Technology, Shimizu Corporation* 23 (cit. on pp. 114, 115, 119).
- Nawy, E. G. (2001). *Fundamentals of high-performance concrete*. John Wiley & Sons (cit. on p. 16).

- Neff, D., J. Harnisch, M. Beck, V. L'Hostis, J. Goebbels, and D. Meinel (2011). "Morphology of corrosion products of steel in concrete under macro-cell and self-corrosion conditions". In: *Materials and Corrosion* 62.9, pp. 861–871 (cit. on p. 35).
- NEN 6720 (1995). *Regulations for concrete TGB 1990 – Structural requirements and calculation methods* (1995). 2.01. Standard. NEN Institute, Delft (cit. on pp. 29, 108).
- Neville, A. (1995). "Chloride attack of reinforced concrete: an overview". In: *Materials and Structures* 28.2, p. 63 (cit. on p. 6).
- Neville, A. (2002). "Autogenous healing—a concrete miracle?" In: *Concrete International* 24.11, pp. 76–82 (cit. on p. 61).
- Newton, C. and J. Sykes (1988). "A galvanostatic pulse technique for investigation of steel corrosion in concrete". In: *Corrosion Science* 28.11, pp. 1051–1074 (cit. on pp. 43, 45).
- Nilsson, L., E. Poulsen, P. Sandberg, H. Sørensen, and O. Klinghoffer (1996). "HETEK. Chloride penetration into concrete. State of the Art, Transport processes, corrosion initiation, test methods and prediction models". In: *Denmark, ISSN/ISBN*, pp. 0909–4288 (cit. on p. 7).
- Otieno, M. B. (2014). "The development of empirical chloride-induced corrosion rate prediction models for cracked and uncracked steel reinforced concrete structures in the marine tidal zone". PhD thesis. University of Cape Town (cit. on pp. 17, 21, 35, 37, 51, 60, 71, 101, 114, 115, 117, 119).
- Otieno, M. B., M. Alexander, and H. Beushausen (2008). "Corrosion propagation in cracked and uncracked concrete". In: *Concrete Repair, Rehabilitation and Retrofitting II: 2nd International Conference on Concrete Repair, Rehabilitation and Retrofitting, ICCRRR-2, 24-26 November 2008, Cape Town, South Africa*. CRC Press, p. 157 (cit. on pp. 87, 97).
- Otieno, M. B., M. Alexander, and H. Beushausen (2010). "Suitability of Various Measurement Techniques for Assessing Corrosion in Cracked Concrete." In: *ACI Materials Journal* 107.5 (cit. on pp. 28, 29).
- Otieno, M. B., H. Beushausen, and M. Alexander (2016). "Chloride-induced corrosion of steel in cracked concrete—Part II: Corrosion rate prediction models". In: *Cement and concrete Research* 79, pp. 386–394 (cit. on p. 118).
- Owens, G. (2009). *Fulton's concrete technology*. Cement & Concrete Institute (cit. on pp. 13, 14, 23, 59, 61).

- Pacheco Farias, J. (2015). “Corrosion of steel in cracked concrete: Chloride microanalysis and service life predictions”. PhD thesis. TU Delft, Delft University of Technology (cit. on p. 28).
- Palin, D., V. Wiktor, and H. Jonkers (2015). “Autogenous healing of marine exposed concrete: characterization and quantification through visual crack closure”. In: *Cement and Concrete Research* 73, pp. 17–24 (cit. on pp. 32, 33).
- Paul, S. C. (2015). “The role of cracks and chlorides in corrosion of reinforced strain hardening cement-based composite (R/SHCC)”. PhD thesis. Stellenbosch: Stellenbosch University (cit. on pp. 7, 17, 21, 28, 37, 47, 48, 54, 77, 78, 104, 128).
- Pease, B. (2010). *Influence of concrete cracking on ingress and reinforcement corrosion*. Technical University of Denmark, Lyngby, Denmark (cit. on pp. 30, 31).
- Pettersson, K. (1992). “Corrosion threshold value and corrosion rate in reinforced concrete”. In: *CBI Report 2 92* (cit. on p. 23).
- Pettersson, K., O. Jorgenson, and P. Fidjestoll (1996). “The effect of cracks on reinforcement corrosion in high-performance concrete in a marine environment”. In: *Special Publication* 163, pp. 185–200 (cit. on p. 28).
- Poursae, A. (2010). “Potentiostatic transient technique, a simple approach to estimate the corrosion current density and Stern–Geary constant of reinforcing steel in concrete”. In: *Cement and Concrete Research* 40.9, pp. 1451–1458 (cit. on pp. 42–44).
- Richardson, M. G. (2003). *Fundamentals of durable reinforced concrete*. CRC Press (cit. on pp. 11, 13, 20).
- Robberts, J. and V. Marshall (2010). *Analysis and Design of Concrete Structures*. Standard. Cement & Concrete Institute (cit. on p. 78).
- Rodriguez, O. G. and R. D. Hooton (2003). “Influence of cracks on chloride ingress into concrete”. In: *ACI Materials Journal* 100.2, pp. 120–126 (cit. on pp. 15, 17).
- Şahmaran, M. and İ. Ö. Yaman (2008). “Influence of transverse crack width on reinforcement corrosion initiation and propagation in mortar beams”. In: *Canadian Journal of Civil Engineering* 35.3, pp. 236–245 (cit. on p. 28).
- Samaha, H. R. and K. C. Hover (1992). “Influence of microcracking on the mass transport properties of concrete”. In: *Materials Journal* 89.4, pp. 416–424 (cit. on pp. 16, 17).
- SANS 6892-1 (2010) *Metallic materials - Tensile testing - Method of test at room temperature* (2010). Standard. South African Bureau of Standards (cit. on pp. 78, 103).

- SANS-10100-1 (2000) The structural use of concrete, Part 1: Design* (2000). 2.2. Standard. South African Bureau of Standards (cit. on p. 29).
- SANS-10100-2 (1994) The structural use of concrete, Part 2: Materials and execution of work (as amended, 1994)* (1994). 2.01. Standard. South African Bureau of Standards. ISBN: 978-0-626-25597-8 (cit. on pp. 24, 61, 107, 108).
- SANS-5863 (1994) Concrete tests - compressive strength of hardened concrete* (2010). Standard. South African Standard Code of practice (cit. on p. 62).
- SANS-920 (2011) Steel bars for concrete reinforcement (Edition 2.3)* (2011). 2.3. Standard. South African Bureau of Standards. ISBN: 978-0-626-25730-9 (cit. on p. 63).
- Schießl, P. and M. Raupach (1997). “Laboratory studies and calculations on the influence of crack width on chloride-induced corrosion of steel in concrete”. In: *ACI Materials Journal* 94.1, pp. 56–62 (cit. on pp. 28, 35).
- Scott, A. (2004). “The influence of binder type and cracking on reinforcing steel corrosion in concrete”. PhD thesis. University of Cape Town (cit. on pp. 8, 116, 119).
- Scott, A. and M. Alexander (2007). “The influence of binder type, cracking and cover on corrosion rates of steel in chloride-contaminated concrete”. In: *Magazine of Concrete Research* 59.7, pp. 495–505 (cit. on p. 22).
- Sharif, A., K. Loughlin, and A. A. B. Nawaz (1999). “Determination of the effective chloride diffusion coefficient in concrete via a gas diffusion technique”. In: *Concrete Durability and Repair Technology: Proceedings of the International Conference Held at the University of Dundee, Scotland, UK on 8-10 September 1999*. Thomas Telford, p. 185 (cit. on p. 11).
- Stern, M. and A. L. Geary (1957). “Electrochemical polarization I. A theoretical analysis of the shape of polarization curves”. In: *Journal of the electrochemical society* 104.1, pp. 56–63 (cit. on p. 42).
- Trejo, D. and R. G. Pillai (2003). “Accelerated chloride threshold testing: part I-ASTM A 615 and A 706 reinforcement”. In: *Materials Journal* 100.6, pp. 519–527 (cit. on p. 8).
- Tuutti, K. (1982). “Corrosion of steel in concrete”. In: (cit. on pp. 1, 4, 35).
- Vu, K. and M. G. Stewart (2000). “Structural reliability of concrete bridges including improved chloride-induced corrosion models”. In: *Structural safety* 22.4, pp. 313–333 (cit. on pp. 11, 115, 116).

- Vu, K., M. G. Stewart, and J. Mullard (2005). “Corrosion-induced cracking: experimental data and predictive models”. In: *ACI structural journal* 102.5, p. 719 (cit. on pp. 115, 119).
- Wang, D. C. Jansen, S. P. Shah, and A. F. Karr (1997). “Permeability study of cracked concrete”. In: *Cement and Concrete Research* 27.3, pp. 381–393 (cit. on pp. 10, 17).
- Wang, J. P. Lynch, and H. Sohn (2014). *Sensor Technologies for Civil Infrastructures: Applications in Structural Health Monitoring*. Elsevier (cit. on p. 72).
- Wang, M. Soda, and T. Ueda (2008). “Simulation of chloride diffusivity for cracked concrete based on RBSM and truss network model”. In: *Journal of Advanced Concrete Technology* 6.1, pp. 143–155 (cit. on p. 17).
- Weiss, J., A. Radlinska, F. Paradis, M. Niemuth, and G. Sant (2007). “Cracks in concrete: an overview of an approach to assess their development, their physical features, and their impact on durability”. In: *International RILEM workshop on transport mechanisms in cracked concrete. Acco, Leuven*, pp. 1–12 (cit. on p. 15).
- Whiting, D. A. and M. A. Nagi (2003). “Electrical resistivity of concrete—a literature review”. In: *R&D Serial* 2457 (cit. on p. 52).
- Win, P. P., M. Watanabe, and A. Machida (2004). “Penetration profile of chloride ion in cracked reinforced concrete”. In: *Cement and concrete research* 34.7, pp. 1073–1079 (cit. on pp. 16, 20).
- Winslow, D. N., M. D. Cohen, D. P. Bentz, K. A. Snyder, and E. J. Garboczi (1994). “Percolation and pore structure in mortars and concrete”. In: *Cement and concrete research* 24.1, pp. 25–37 (cit. on p. 14).
- Yoon, S. and E. Schlangen (2010). “Long short term experimental study on chloride penetration in cracked concrete”. In: *Key Engineering Materials*. Vol. 417. Trans Tech Publ, pp. 765–768 (cit. on p. 20).
- Yoon, S., Wang, W. J. Weiss, and S. P. Shah (2000). “Interaction between loading, corrosion, and serviceability of reinforced concrete”. In: *Materials Journal* 97.6, pp. 637–644 (cit. on pp. 37, 38).
- Zhou, Y., B. Gencturk, K. Willam, and A. Attar (2014). “Carbonation-induced and chloride-induced corrosion in reinforced concrete structures”. In: *Journal of Materials in Civil Engineering* 27.9, p. 04014245 (cit. on p. 10).
- Živica, V. (2003). “Influence of w/c ratio on rate of chloride induced corrosion of steel reinforcement and its dependence on ambient temperature”. In: *Bulletin of Materials Science* 26.5, pp. 471–475 (cit. on p. 19).

Appendices

A. Appendix A

A.1 Specimen pre-cracking

Table A.1: Flexural pre-cracking responses

Beam I.D	Reinforcement series	Notch series	Vertical midpoint displacement (mm)	Load (kN)
B1	R1	N1	0.397	25.0
B2	R1	N3	1.387	29.5
B3	R2	N1	0.884	37.7
B4	R2	N3	1.222	48.5
B5	R3	N1	1.483	55.0
B6	R3	N3	1.197	58.1
B7	R1	N5	0.557	32.0
B8	R1	N1	0.409	23.4
B9	R2	N5	0.932	49.0
B10	R2	N1	0.973	42.0
B11	R3	N5	1.580	61.0
B12	R3	N1	1.301	55.0
B13	R1	N3	0.551	30.0
B14	R1	N5	0.557	31.4
B15	R2	N3	0.924	46.7
B16	R2	N5	0.879	49.0
B17	R3	N3	0.712	61.0
B18	R3	N5	1.275	61.0
B19	R1	N1	0.378	25.0
B20	R1	N3	0.602	34.0
B21	R2	N1	0.965	40.0
B22	R2	N3	0.74	49.0
B23	R3	N1	1.233	55.0
B24	R3	N3	1.101	61.0
B25	R1	N5	0.745	27.7
B26	R2	N5	1.099	49.0
B27	R3	N5	1.288	61.0

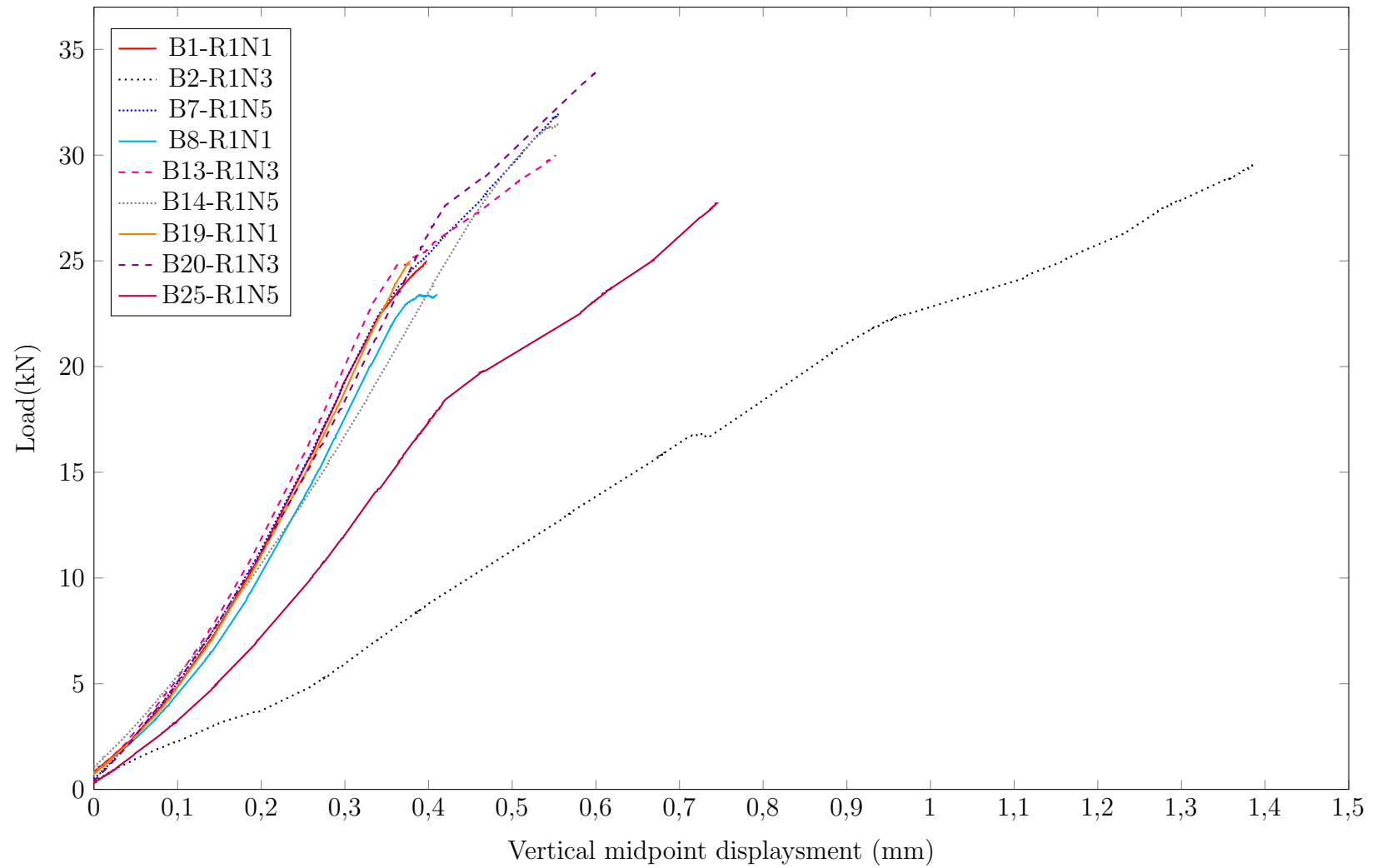


Figure A.1: Pre-cracking specimen response for single reinforcement (R1)

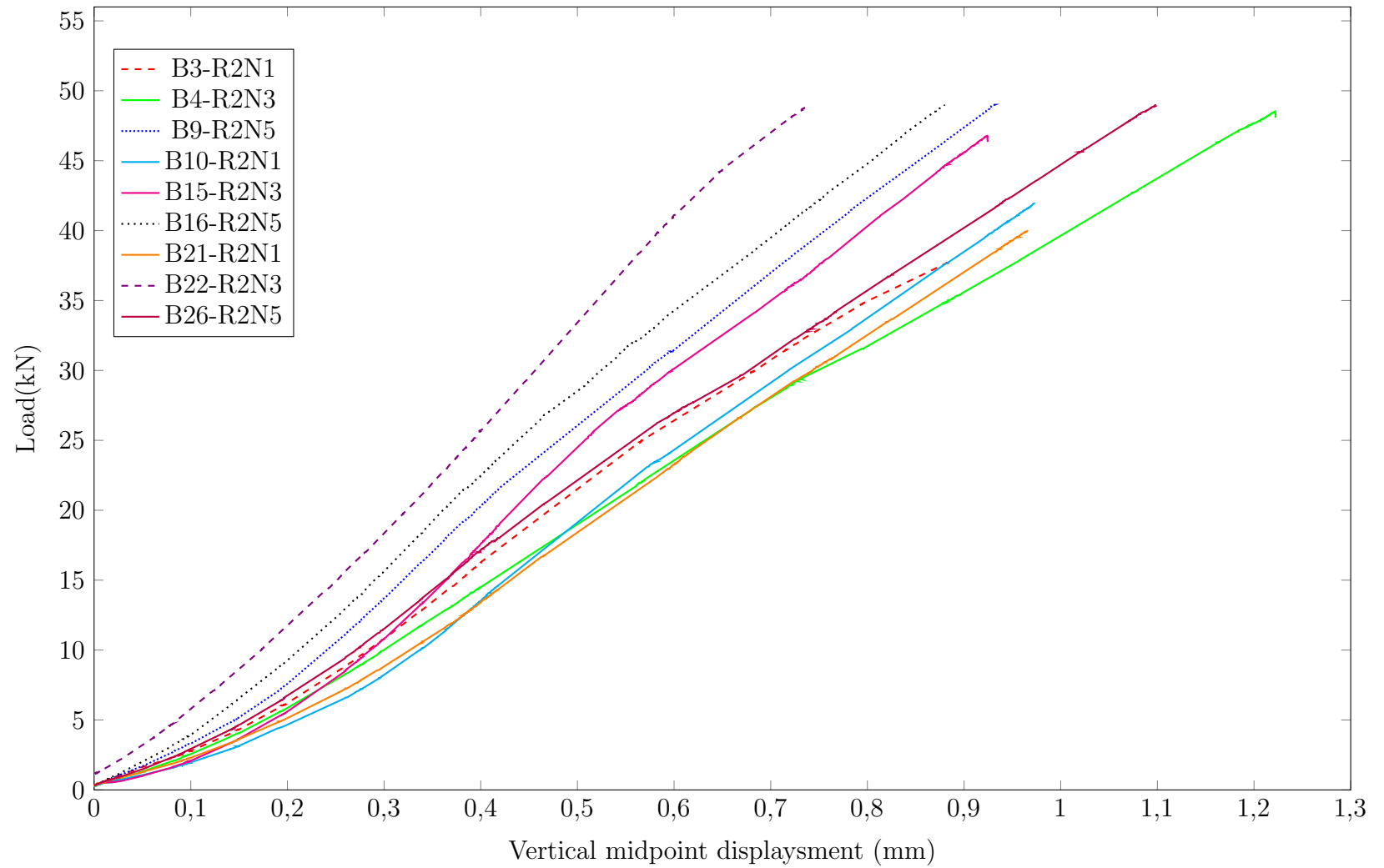


Figure A.2: Pre-cracking specimen response for double reinforcement (R2)

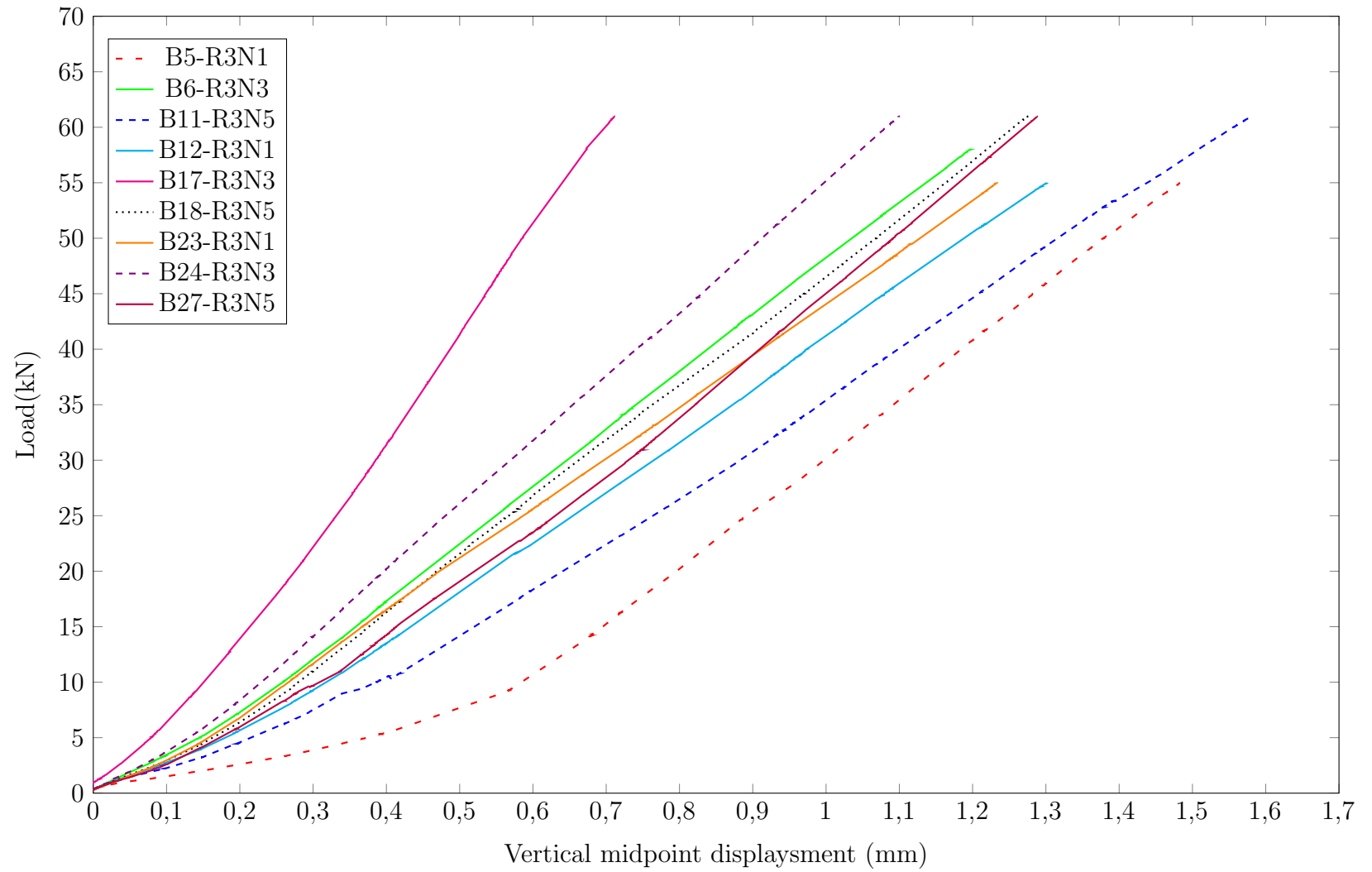


Figure A.3: Pre-cracking specimen response for tripple reinforcement (R3)

A.2 Crack spacings

Table A.2: Flexural pre-cracking responses

Beam	Series	Crack spacing S_c (mm)	1 st crack width $w_{c,1}$ (mm)	2 nd crack width $w_{c,2}$ (mm)	Crack spacing series
B1	R1N1	-	0.41	-	SC
B2	R1N3	96	0.38	0.40	S90
B3	R2N1	-	0.39	-	SC
B4	R2N3	113	0.35	0.38	S105
B5	R3N1	101	0.40	0.41	S105
B6	R3N3	106	0.43	0.40	S105
B7	R1N5	101	0.39	0.40	S105
B8	R1N1	-	0.43	-	SC
B9	R2N5	116	0.37	0.39	S105
B10	R2N1	-	0.50	-	SC
B11	R3N5	84	0.38	0.38	S75
B12	R3N1	-	0.42	-	SC
B13	R1N3	78	0.40	0.40	S75
B14	R1N5	81	0.44	0.39	S75
B15	R2N3	98	0.50	0.45	S90
B16	R2N5	68	0.44	0.45	S75
B17	R3N3	99	0.47	0.42	S90
B18	R3N5	89	0.39	0.35	S90
B19	R1N1	-	0.47	-	SC
B20	R1N3	82	0.50	0.45	S75
B21	R2N1	86	0.41	0.35	S90
B22	R2N3	97	0.44	0.45	S90
B23	R3N1	-	0.49	-	SC
B24	R3N3	100	0.35	0.42	S105
B25	R1N5	91	0.49	0.42	S90
B26	R2N5	94	0.36	0.35	S90
B27	R3N5	80	0.33	0.38	S75
Mean (\bar{x})		93.60	0.42	0.41	
STDEV. (σ)		12.82	0.05	0.03	
CoV (%)		13.7	12.0	8.38	

B. Appendix B

B.1 Residual service life prediction model

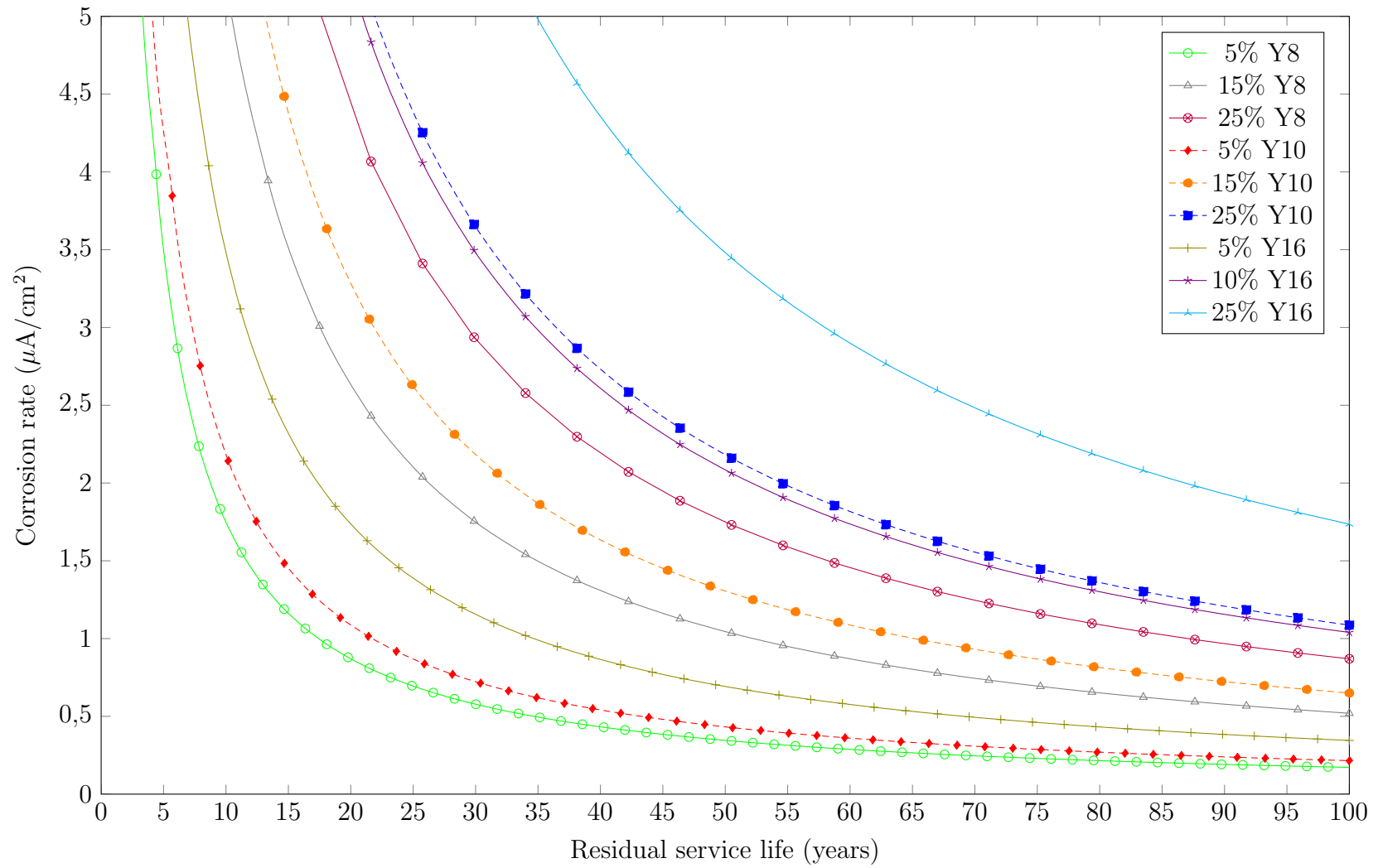
The decomposition of residual service life prediction model is shown in equations B.1 to B.3. This equation is plotted for various reinforcement diameters, limit states, pitting factors and corrosion rates in figures B.1 to B.3.

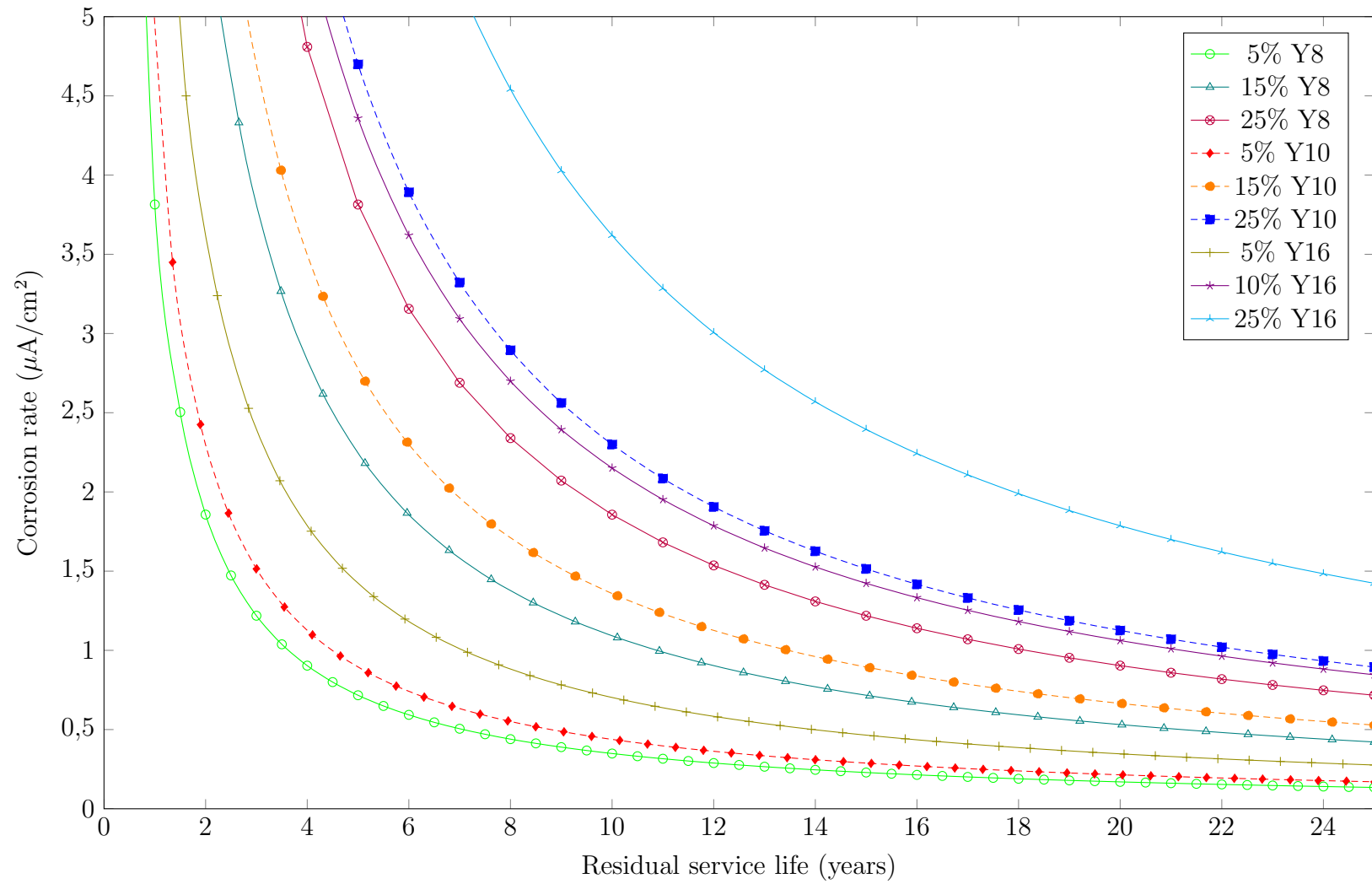
$$T_{prop} = \frac{LS \cdot 10}{(100 - k_1 \cdot 100)} \quad (\text{B.1})$$

$$k_1 = \left(\frac{(\varnothing_{init} - k_2 \cdot 10)^2 \cdot \pi \cdot 0.25}{\varnothing_{init}^2 \cdot \pi \cdot 0.25} \right) \quad (\text{B.2})$$

$$k_2 = \left(\frac{i_{corr} \cdot \alpha_{pit} \cdot 11.6}{1000} \right) \quad (\text{B.3})$$

where T_{RSL} is the time to the end of the propagation stage (years), LS is the limit state of the reduction in reinforcement diameter (recommended 5 - 25%), \varnothing_{init} is the initial reinforcement rod diameter (mm), i_{corr} is the corrosion rate ($\mu\text{A}/\text{cm}^2$) and α_{pit} is the pitting factor (recommended 1 - 10).

Figure B.1: Residual service life for $\alpha_{pit} = 1$

Figure B.2: Residual service life for $\alpha_{pit} = 5$

150

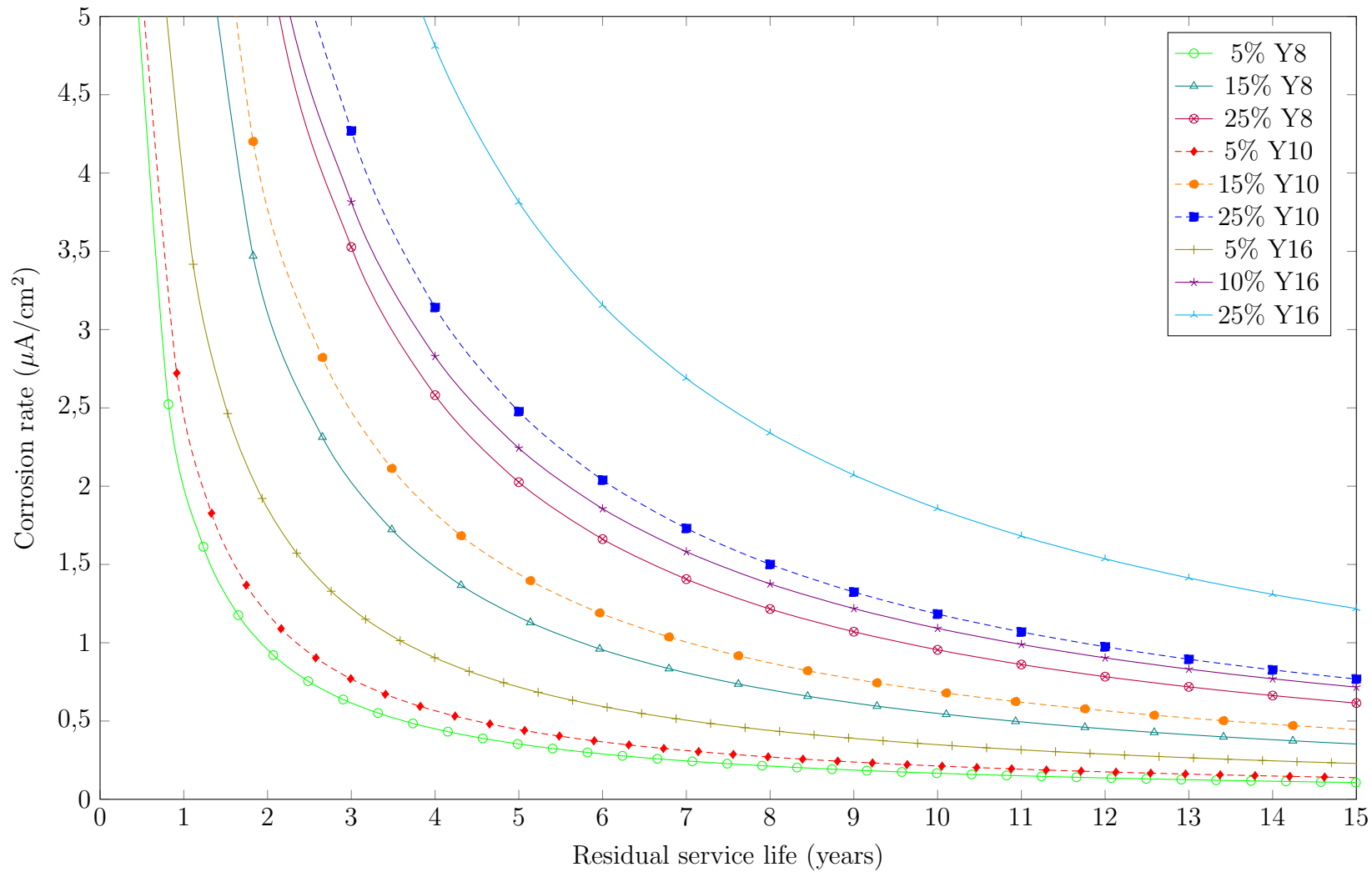


Figure B.3: Residual service life for $\alpha_{pit} = 10$

C. Appendices

C.1 Product details

C.1.1 GECOR-10[®]



Figure C.1: GECOR-10 instrument components (*isdcorr 2015*)

The components of the GECOR-10 is shown in figure C.1. The [GECOR-10 Product Guide](#) manual can be viewed at the [ISD](#) website (*isdcorr 2015*).

C.1.2 Alcolin[®]

Typical Neutral Cure Silicone that was used for the sealing of the Perspex pond is shown in figure C.2. [Neutral cure silicone](#) product details can be found at www.alcolin.com.



Figure C.2: Typical Alcolin silicone